The Astrophysical Journal Supplement Series, 196:13 (34pp), 2011 September doi:10.1088/0067-0049/196/1/13

HIGH-RESOLUTION ELECTRON-IMPACT EMISSION SPECTRA AND VIBRATIONAL EMISSION CROSS SECTIONS FROM 330–1100 nm FOR N_2

Rao S. Mangina[1], Joseph M. Ajello[1], Robert A. West[1], and Dariusz Dziczek[2]
[1] Jet Propulsion Laboratory, California Institute of Technology, Pasadena, CA 91109, USA
[2] Institute of Physics, Nicolaus Copernicus University, Torun, Poland
Received 2011 February 28; accepted 2011 March 6; published 2011 September 2

ABSTRACT

Electron-impact emission cross sections for N_2 were measured in the wavelength range of 330–1100 nm at 25 eV and 100 eV impact energies. Cross sections of several molecular emission bands of the first positive band system $B\ ^3\Pi_g^+(\nu') \rightarrow A\ ^3\Sigma_g^+(\nu'')$ and the second positive band system $C\ ^3\Pi_u(\nu') \rightarrow B\ ^3\Pi_g(\nu'')$ of N_2, the first negative band (1NB) system $B\ ^2\Sigma_u^+(\nu') \rightarrow X\ ^2\Sigma_g^+(\nu'')$ and Meinel band system $A\ ^2\Pi_u(\nu') \rightarrow X\ ^2\Sigma_g^+(\nu'')$ of N_2^+ ions as well as line emissions of N (N I) and N^+ (N II) in the visible–optical–near-IR wavelength range reported in this work were measured for the first time in a single experimental setup at high spectral resolving power ($\lambda/\Delta\lambda \approx 10000$) under single-collision-scattering geometry and optically thin conditions. Rotational emission lines of N_2 and N_2^+ were observed for strong emission bands at a gas temperature of about 300 K. The absolute cross section of the strongest (0,0) vibrational band at 391.43 nm of 1NB was determined using the standard H_α emission cross sections of H_2 by electron impact at both 25 eV and 100 eV electron-impact energies, and the cross sections for the remainder of the emissions were determined using (0,0) 1NB value. A comparison of the present emission cross sections with the earlier published data from both electron energy loss and electron-impact-induced fluorescence emission is discussed.

Key words: atomic data – line: identification – molecular data – radiation mechanisms: general – techniques: imaging spectroscopy – ultraviolet: general

Online-only material: color figure

1. INTRODUCTION

Earth, Titan, Triton, and Pluto are known to have rich N_2 atmospheres. N_2 emissions in the visible–optical–near-infrared (VOIR, 300–1100 nm) wavelength region have long been observed in Earth's nightglow, polar cap, and aurora with ground-based optical instruments and spacecraft such as *Thermosphere Ionosphere Mesosphere Energetics and Dynamics (TIMED)*. The study of N_2 is particularly relevant to the many orbital rendezvous of the *Cassini* spacecraft with Saturn's moon Titan and the planed 2015 reconnaissance of Pluto by the New Horizons spacecraft. Nitrogen bands have also been observed in the Leonid meteor emissions while searching for OH emissions from the $X\ ^2\Pi$ electronic state (Jenniskens et al. 2004). Identification and quantification of thermospheric processes have reached a point where detailed exploration of the VOIR emission spectra becomes an important issue. The levels of brightness of nitrogen bands are sensitive to the characteristic primary and secondary electrons and hence are routinely used to determine the precipitating electron energy flux. Four prominent molecular emissions observed in the VOIR region for N_2 are the first and the second positive bands (1PB and 2PB) of N_2, the first negative band (1NB) and the Meinel band (MB) of N_2^+. Photometric measurements of emissions in the 1NB system have been widely used to make estimates of the energy flux of precipitating auroral electrons (e.g., Romick et al. 1999, 2001). The MB and 1NB are particularly important as they are unaffected by cascade transitions and their intensities at night are proportional to the primary electron flux input (Chakrabarti 2001; Galand & Chakrabarti 2006). Under sunlit conditions, the 1NB and MB of N_2^+ are excited mainly by solar fluorescence of N_2^+ itself. Vibrational distributions of N_2 ($B\ ^3\Pi_g$) and N_2^+ ($A\ ^2\Pi_u$) have been observed in the aurora (Espy et al. 1987) and in sprites (Bucsela et al. 2003; Kanmae et al. 2007; Heavner et al. 2010). The 2PB is used as a monitor of the photoelectron energy in the dayglow and of the secondary electron flux in the aurora (Meier 1991; Solomon 1989). The 2PB is ideal for this role as it is excited by an optically forbidden electron-exchange transition that peaks at low electron energy (~14 eV; Shemansky et al. 1995). Our laboratory emission cross sections for modeling upper atmosphere spectral observations are used as a basis in many electron transport codes (Ajello et al. 2011). One of the most important examples is the Atmospheric Ultraviolet Radiance Integrated Code, which is used to identify spectral features by synthetic spectra and to model the airglow energetics by calculating N_2 volume production rates for each band (Strickland et al. 1995, 1999; Ajello et al. 2007, 2008a). The emission cross sections of the majority of neutral and singly ionized planetary gases for this code have been reviewed by Itikawa et al. (1986), Majeed & Strickland (1997), and Avakyan et al. (1998).

Titan's upper atmosphere (~1000 km altitude) consists of about 96% N_2 (Yelle et al. 2006). Most of Titan's atmospheric organic and nitrogen chemistry, aerosol formation, and atmospheric loss are driven from external energy sources, such as solar UV, Saturn's magnetosphere, solar wind, and galactic cosmic rays, which produce distributions of secondary electrons at different altitudes in the upper atmosphere that excite N_2 (Sittler et al. 2009). Analysis of the UV emissions of the extreme ultraviolet (EUV: 90–114 nm) and the far ultraviolet (FUV: 115–175 nm) from Titan observations by the Ultraviolet Imaging Spectrograph (UVIS) on board *Cassini* have been recently published (Ajello et al. 2007, 2008b). The EUV spectrum (50–115 nm) consists of three band systems of N_2 ($b\ ^1\Pi_u$, $b'\ ^1\Sigma_u^+$, $c_4'\ ^1\Sigma_u^+ \rightarrow X\ ^1\Sigma_g^+$) formed in the thermosphere between 900 and 1400 km, while the FUV spectrum consists of one N_2 ($a\ ^1\Pi_g \rightarrow X\ ^1\Sigma_g^+$) band system also formed in the

thermosphere (Ajello et al. 2007, 2008b). A complementary VOIR spectral study of Titan by the *Cassini* Imaging Science Subsystem (ISS) was carried out in 2009 and 2010. The ISS is the highest spatial resolution two-dimensional imaging device on the *Cassini* Orbiter and has been designed for investigations of the bodies and phenomena found within the Saturnian system (Porco et al. 2004). It consists of two framing cameras; each camera is outfitted with a large number of spectral filters which, taken together, span the electromagnetic spectrum from 200 to 1100 nm. These were chosen to address a multitude of Saturn system scientific objectives: including the cloud structure and nightglow from Titan's atmosphere. A successful partnership has been established between our laboratory and the ISS team to model ISS observations (Geissler et al. 2004).

The New Horizons team selected instruments that study the emissions of Pluto and Charon from the UV to near-IR (Stern et al. 2008). The main objectives for the Ralph's instrument are to obtain high-resolution color maps and composition maps of the surfaces of Pluto and Charon. The instrument has two separate channels: the Multispectral Visible Imaging Camera (MVIC) and the Linear Etalon Imaging Spectral Array (LEISA), well complemented to our VOIR program. A single telescope with a 3 inch (7.6 cm) aperture collects and focuses the light used in both channels: MVIC operating at visible and LEISA at near-infrared wavelengths. LEISA will be used to map the distribution of frosts of methane (CH_4), molecular nitrogen (N_2), carbon monoxide (CO), and water (H_2O) over the surface of Pluto and the water frost distribution over the surface of Charon. LEISA data may also reveal new constituents on the surfaces and in the atmosphere that have not yet been detected.

The Ballistic Missile Defense Organization's *Midcourse Space Experiment* obtained the first optical observations of molecular ions at very high altitudes above the northern polar cap. Spectra obtained at geomagnetic latitudes over ~80°N, at 1300 Magnetic Local Time, featured emissions identified as the 1NB of N_2^+, with a total band intensity of 2.5 kR and implied number densities of $\sim 10^3$ ions cm^{-3} at 900 km (Romick et al. 1999). Additional N_2^+ transitions from the MBs were also observed. No other permitted optical emissions were observed above 450 km indicating that the source must be the solar resonance fluorescence of N_2^+ ions. The presence of heavy molecular ions at high altitudes is an indication of the upward flow of ions from the ionosphere into the magnetosphere. These optical observations suggest a new technique for studies of the global structure and temporal variation of plasma energization and transport between the ionosphere and magnetosphere in the polar regions (Romick et al. 1999).

The above results clearly indicate that characteristic parameters of excitation and de-excitation of N_2 have great importance in understanding planetary atmospheric phenomena. However, in considerable efforts, laboratory experiments have generally failed to give consistent values for the excitation cross sections and the natural lifetimes of the various bands due to the difficulties in accounting for longer natural lifetimes of some of the emitting states, and collisional quenching and diffusion effects (in some cases, due to interference from overlapping bands). The history of VOIR measurements of electron-impact emission cross sections of 1PB, 2PB, 1NB, and MB band systems of N_2 is fraught with great uncertainty. Some discrepancies between the results of different authors persist while some cross sections have not been previously reported. For example, the published cross sections for these four-band systems at the standard electron-impact energy of 100 eV vary by an order of magnitude. Emission cross sections and excitation functions for certain vibrational bands were last reviewed by Itikawa et al. (1986) and for the 1NB and 2PB by Avakyan et al. (1988). Most experimental work on emission cross sections of N_2 in the VOIR were performed prior to 1986, and each of the band systems were treated individually by earlier researchers: 2PB (Shemansky et al. 1995), MB (Piper et al. 1986; Mandelbaum & Feldman 1976), 1NB (Borst & Zipf 1970) and 1PB (McConkey & Simpson 1969). The N I and N II multiplets have been the subject of many publications by the University of Wisconsin group (C. C. Lin's group as referenced in Itikawa et al. 1986; Avakyan et al. 1988). To our knowledge, there has been no single publication providing the total emission of all four-band systems and there have been no electron-impact high-resolution emission spectra of N_2. In addition, instrumental advances enabling imaging spectroscopy have allowed an order of magnitude increase in the signal-to-noise ratio (S/N) for weak features.

In view of the above survey on the status of the emission cross sections and their applications, we have established a VOIR spectroscopy laboratory to study electron impact on N_2 and have measured emission cross sections ($>10^{-20}$ cm^2) of all vibrational bands between 330 and 1100 nm at a high spectral resolving power of $\lambda/\Delta\lambda \approx 10000$ in a single experimental setup, defining single-collision-scattering geometry and providing optically thin fluorescence conditions, for $C\ ^3\Pi_u \rightarrow B\ ^3\Pi_g$, $B\ ^2\Sigma_u^+ \rightarrow X\ ^2\Sigma_g^+$, $B\ ^3\Pi_g \rightarrow A\ ^3\Sigma_u^+$, $B\ ^2\Pi_u \rightarrow X\ ^2\Sigma_g^+$ bands, and N I and N II multiplets. For various emitting electronic states in the VOIR range, Gilmore et al. (1992) published transition probabilities, *r*-centroids, band origins, Franck–Condon factors, and electronic transition moments versus internuclear distance for modeling direct excitation of these four-band systems. Figure 1 shows the partial energy level diagram based on the data of Gilmore et al. (1992) for N_2, N_2^+, and N_2^- states versus their internuclear distance (r) of interest to VOIR. We used simple steady-state detailed balance theory of emission cross section partitioning among weak bands or bands beyond our wavelength measurement range for each ν''-progression in order to estimate the total electronic emission cross section for a given emitting electronic state.

We organize the paper as follows: (1) an experimental section with a brief description of the instrumentation and calibration procedures, (2) an overview of the laboratory spectra, (3) detailed sets of emission spectra and their cross-sectional tables for each of the band systems with a model, and (4) a discussion of our results and an application of our emission cross sections to ISS observations of Titan.

2. EXPERIMENT AND CROSS SECTIONS

The present measurements of N_2 emission spectra and cross sections have been carried out in an apparatus using crossed electron and molecular beams. A schematic drawing of the apparatus is shown in Figure 2. A detailed description of the apparatus has been given elsewhere (Ajello et al. 2008a; Aguilar et al. 2008). Briefly, it consists of a VOIR imaging spectrometer operating in air in tandem with an electron-impact collision chamber under vacuum. The spectrometer and collision chamber are vacuum isolated by a quartz window. A magnetically collimated beam of electrons ($E_e = 25$ eV and 100 eV) with an energy resolution of 1 eV is crossed with a target gas beam, at ~300 K temperature, formed by a capillary array under optically thin conditions at a background pressure of 5×10^{-5} Torr. A gas temperature of ~300 K

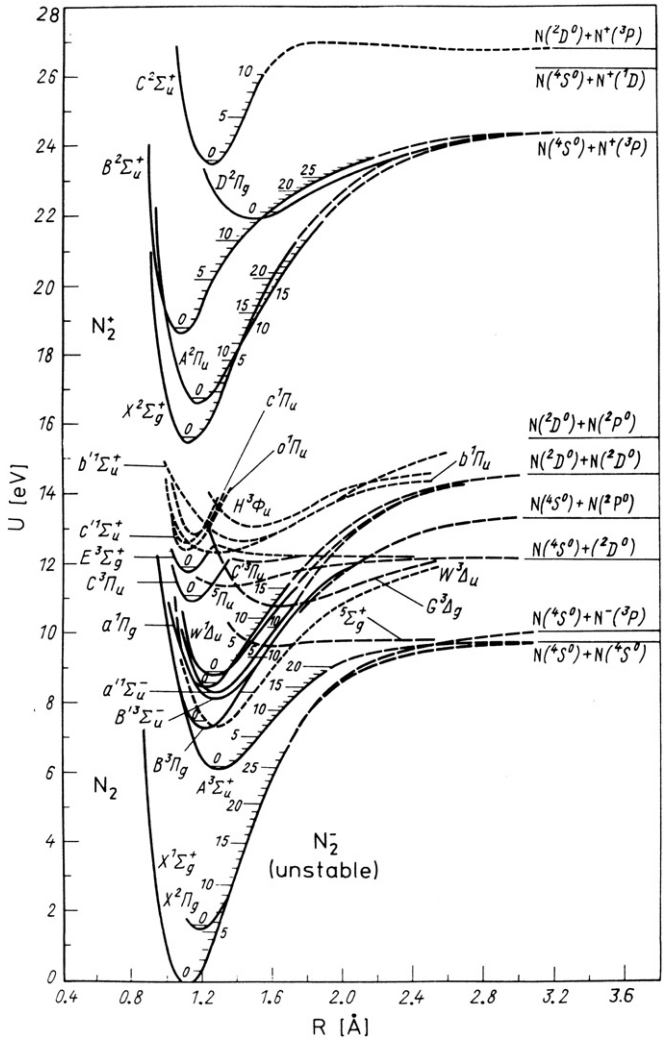

Figure 1. Partial diagram of potential energy curves of various molecular states of N_2 showing the molecular levels and energy regions for the VOIR transitions (Gilmore et al. 1992).

results in rotational line peak intensities at J-values of ~6–8 for the 1NB systems studied. The electron-impact-induced fluorescence spectrum was observed at 90° emission angle to both the electron beam and the molecular-beam axes using a Spectra Pro 0.5 m spectrometer capable of a resolving power of $\lambda/\Delta\lambda \approx 10000$ at 500 nm, with a 50 μm entrance slit size. This high resolution is sufficient for observing rotational structures. The spectrometer is equipped with a Princeton Instruments liquid-nitrogen-cooled CCD detector array which is 1340 pixels wide and 400 pixels tall (each pixel is 20 μm^2 in area). Grating 1 with 1800 grooves mm^{-1} and a 500 nm blaze wavelength for a dispersion of 166.7 nm mm^{-1} and grating 2 with 1200 grooves mm^{-1} and a 750 nm blaze wavelength for a dispersion of 111.1 nm mm^{-1} were used for the reported measurements. Order-sorting filters were used for gratings 1 and 2 with low-wavelength cutoffs of 320 nm and 490 nm, respectively. The two overlapping wavelength ranges for the spectrometer are 330–800 nm when using grating 1 and 500–1100 nm when using grating 2. The wavelength response of the detector was calibrated in the range from 300 nm to 1100 nm using standard deuterium and tungsten sources. In our previous publications (Ajello et al. 2008a; Aguilar et al. 2008), we presented the relative inverse sensitivity (S^{-1}) defined as the input standard blackbody spectrum irradiance divided by the measured output spectrum of the spectrometer for the gratings used in this experiment. We also discussed the procedures to eliminate the effects of random cosmic-ray hits on the CCD array, and account for the dependence of spectral resolution on transmitting slit sizes and wavelength calibration using National Institute of Standards and Technology (NIST) standard data tables. In regular spectral measurements, the full range of a grating is covered during an experiment by rotating the grating turret in predetermined small steps. At a given grating position the wavelength range captured by the detector array varies from 200 to 250 nm depending on the grating and slit size used. The spectral resolution set for the present work was 0.07 nm. Several repetitive scans were taken to see the bands clearly above the background.

The absolute calibration of the emission spectra for N_2 reported in this work for 25 eV and 100 eV electron-impact energies is based on the known emission cross section of H_α from dissociative excitation of H_2 at these energies in a swarm gas experiment. Karolis & Harting (1978) measured the electron-impact dissociative emission cross section of H_2 from threshold (~15.6 eV) to 100 eV. The H_α cross sections were recently reviewed by Lavrov & Pipa (2002) and were found to be in excellent agreement (within 10%) with the data of Karolis & Harting (1978). The measured cross sections of Karolis & Harting (1978) for H_α at 25 eV and 100 eV were reported to be 5.3×10^{-19} cm^2 and 9.3×10^{-19} cm^2, respectively. A comparison of the integrated intensity of the strongest (0,0) band of 1NB system of N_2 at 391.4 nm, combining both the P and R branches that extending from 387 nm to 392 nm, relative to the sharp H_α 656.28 nm multiplet using grating 1 gives the emission cross section Q_{em} values at 25 eV and 100 eV:

$$Q_{em}(25\ \text{eV}) = 2.88 \times 10^{-18}\ \text{cm}^2 \quad (1)$$

$$Q_{em}(100\ \text{eV}) = 14.90 \times 10^{-18}\ \text{cm}^2. \quad (2)$$

In the case of 25 eV electron-impact energy, since the strongest emissions of both the (0,0) band of the 1NB system $B\ ^2\Sigma_u^+(\nu') \rightarrow X\ ^2\Sigma_g^+(\nu'')$ at 391.4 nm and the (3,1) band of the 1PB system $B\ ^3\Pi_g^+(\nu') \rightarrow A\ ^3\Sigma_g^+(\nu'')$ at 762.67 nm are within the wavelength range (330–800 nm) observed by grating 1, the absolute cross-sectional value of the (3,1) band of the 1PB was determined with respect to the previously obtained cross-sectional value of (0,0) band of the 1NB. As the (3,1) band at 762.67 nm of the 1PB and H_α (656.28 nm) appears in grating 1 (330–800 nm) and grating 2 (500–1100 nm) spectra, the cross sections of the remainder of the bands and line emissions observed in the grating 2 spectrum were determined with respect to the cross-sectional values of H_α and the (3,1) band of $B\ ^3\Pi_g^+(\nu') \rightarrow A\ ^3\Sigma_g^+(\nu'')$. Whereas, for the case of 100 eV electron-impact energy, the line emissions commonly found in spectra obtained with both gratings 1 and 2 were used for scaling their cross sections with respect to the (0,0) band of $B\ ^2\Sigma_u^+(0) \rightarrow X\ ^2\Sigma_g^+(0)$ at 391.4 nm. In turn, these line emission cross sections were used in determining the cross sections of all other band emissions. Complete calibrated VOIR emission spectra from 330 to 1100 nm at 25 eV and 100 eV electron-impact energy are shown, respectively, in Figures 3(a) and (b). Each figure shows the concatenation of data measured separately, one with grating 1 (330–750 nm) and the other with grating 2 (750–1100 nm). This is the first single-scattering emission cross-sectional experiment ever reported for all the four bands of nitrogen in the VOIR region measured in a single

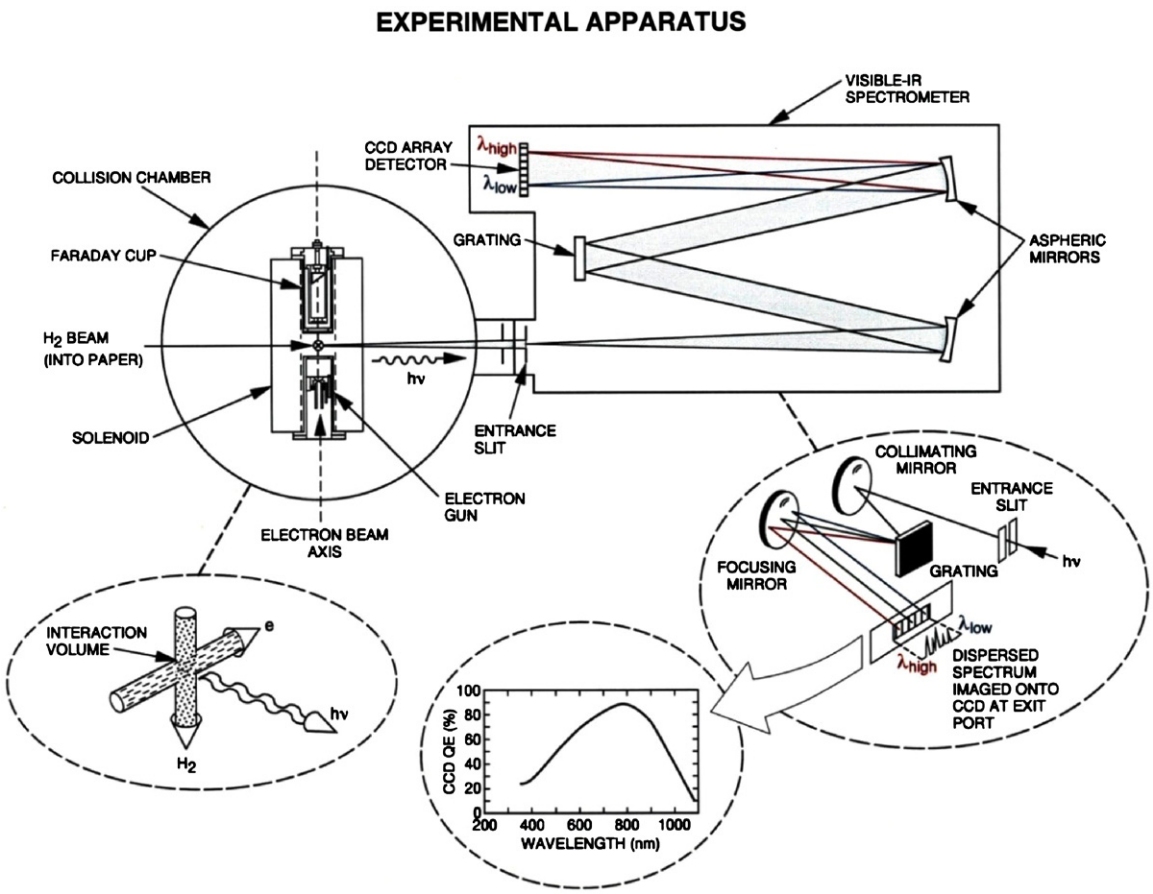

Figure 2. Schematic diagram of the VOIR experimental apparatus showing the collision chamber, the interaction region, an example of calibration curve, and the Czerny–Turner spectrometer's optics with grating turret and two mirrors.

(A color version of this figure is available in the online journal.)

apparatus. We base the uncertainty of the absolute calibration on the cited 20% variation of the cross sections for the various experiments. Additional uncertainties of the absolute cross section can be traced to a 10% correction for the gas pressure read by a Varian Bayard-Alpert ultra high vacuum (UHV) gauge tube, a 10% background offset to the singlet transitions at 100 eV from low-energy secondary electrons, and a 15% variation of electron-beam current and the stability of the gas pressure during the spectral scan. The relative uncertainty of the instrument calibration is 10% over the range of each grating. The resulting root-sum-square uncertainty of the absolute cross sections is about 30%. Care was taken to prevent overlap of orders within the monochromator by the use of suitable filters. The inverse sensitivity at the lowest wavelength range from 330 nm to 400 nm, which contains the (0,0) band of 2PB at 337.1 nm and the (0,0) band of 1NB at 391.4 nm, was verified using the molecular branching technique on the 2PB band system that we studied in the past as a standard (Shemansky et al. 1995; Ajello et al. 1988). This redundancy in sensitivity calibration is important since the grating 1 sensitivity has a sharp dependence on wavelength as the order-sorting filter begins to cut off wavelengths below 380 nm.

It is important to compare total emission cross sections to total excitation cross sections from electron energy-loss experiments. In this overview paper of the entire VOIR range (300–1100 nm), we consider model calculations of vibrational band intensities summed over rotational line emission. For the case of weak and negligible predissociation, vibrational cross sections representing different processes are related by

$$Q_{\rm em}(\nu') = Q_{\rm ex}(\nu') + Q_{\rm casc}(\nu'), \tag{3}$$

where $Q_{\rm em}(\nu') = \Sigma_{\nu''} Q_{\rm em}(\nu',\nu'')$ is the optical-emission cross section of an upper state ν', obtained by summing over rotational quantum numbers (J) of the ground and excited state(s), for a vibration band (ν',ν'') emission for a transition from an upper state vibrational level ν' into a lower state vibrational level ν''. $Q_{\rm ex}(\nu')$ is the total excitation cross section to vibrational level ν' of an electronic state summed over the rotational levels of the ground vibrational level $\nu''' = 0$ (at 300 K for N_2) of the molecular X-state (ν''') and the rotational levels of the upper electronic state. $Q_{\rm casc}(\nu')$ is the total cascade cross section to level ν' of the electronic state due to transitions from overlying electronic state(s) resulting in (ν',ν'') emission through an emission branching ratio $\beta(\nu',\nu'')$. The measured intensity is proportional to the emission cross section as described in Shemansky et al. (1995). The intensity in a cascade-free vibrational band structure for a (ν',ν'') transition, summed over all rotational levels, is given by

$$I(\nu', \nu'') = g(\nu')\, \beta(\nu', \nu''), \tag{4}$$

where

$$\beta(\nu', \nu'') = A(\nu', \nu'')/\Sigma_{\nu''} A(\nu', \nu''), \tag{5}$$

in which $A(\nu',\nu'')$ and $\Sigma_{\nu''} A(\nu',\nu'') = A(\nu')$ are the (ν',ν'') spontaneous emission transition probability and total band

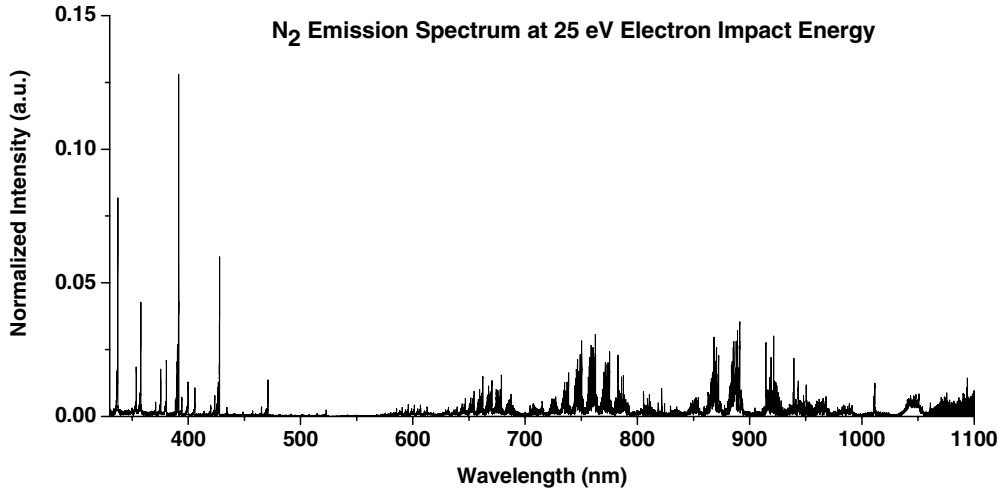

(a)

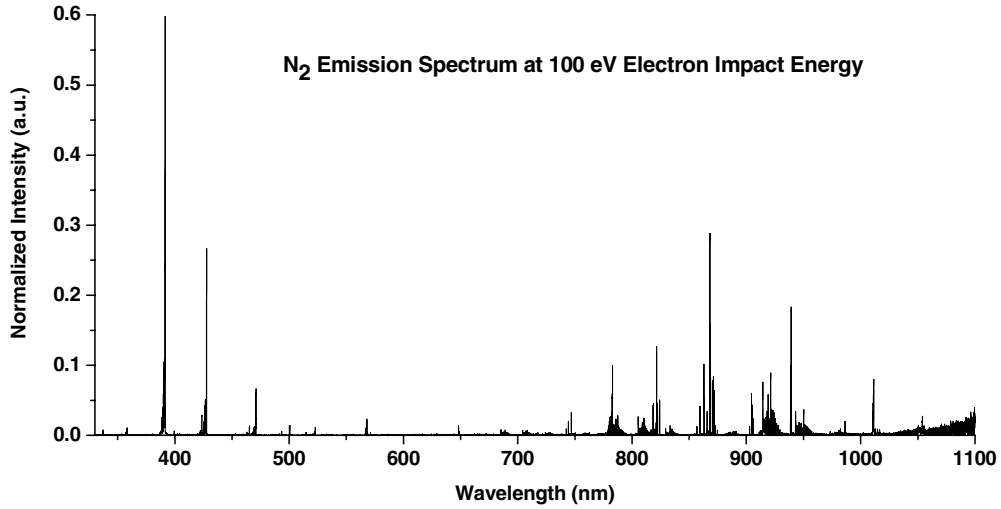

(b)

Figure 3. Calibrated overview spectra of electron-impact-induced emission of N_2 in 330–1100 nm wavelength range for electron energy of 25 eV (a) and 100 eV (b) at a spectral resolution of 0.07 nm (FWHM) with a spectrometer resolving power of $\lambda/\Delta\lambda \approx 10000$.

transition probability (including predissociation, if applicable), respectively. The vibrational excitation rate $g(\nu')$ per molecule per second from the ground state is determined by the absorption transition probability ($A_{\nu''',0}$) from the ground-state $X\ ^1\Sigma_g^+$ vibrational level $\nu''' = 0$ and by the electronic transition moment $R_e(r_{\nu'\nu''})$ as a function of r-centroid ($r_{\nu'\nu''}$). The $g(\nu')$ is given by

$$g(\nu') = Q_{\rm ex}(\nu''' = 0,\ \nu')F_e N_o(\nu'''). \quad (6)$$

The $\nu' = 0$ vibrational excitation cross section, $Q_{\rm ex}(\nu''' = 0, \nu')$, can be modeled by

$$Q_{\rm ex}(\nu''' = 0,\ \nu') \sim R_e^2(r_{\nu'\nu''})A_{\nu',0}\lambda_{\nu',0}^3, \quad (7)$$

where F_e is the electron flux and N_o is the number density of molecule in its ground-state vibrational level $X\ ^1\Sigma_g^+(\nu''')$, and $\lambda_{\nu',0}$ is the transition wavelength. In the absence of cascade from higher energy electronic states and predissociation, $Q_{\rm ex}(\nu')$ is related to the total vibrational band emission cross section, $Q_{\rm em}(\nu')$, by

$$Q_{\rm em}(\nu') = Q_{\rm ex}(\nu'). \quad (8)$$

The vibrational cross section $Q_{\rm em}(\nu')$ for emissions from an excited upper electronic state of a particular vibrational level ν' (=0 or 1 or 2, ...) into several vibrational levels ν'' (= 0, 1, 2, ...) of the lower electronic state of a band system can be determined by summing all the $Q_{\rm em}(\nu',\nu'')$ as

$$Q_{\rm em}(\nu') = \Sigma_{\nu''} Q_{\rm em}(\nu',\ \nu'') \quad (9)$$

and the cross section for electronic excitation

$$Q_{\rm ex} = \Sigma_{\nu'} Q_{\rm em}(\nu'). \quad (10)$$

Using the measured cross section $Q_{\rm em\_expt}(\nu',\nu'')$ of a strong emission vibrational band and known branching ratios of other emissions within a band system, the emission cross sections for much weaker emission bands, $Q_{\rm em\_weak}(\nu',\nu'')$, whose experimental cross sections could not be determined accurately due to poor S/N ratio, although their contribution to a given $Q_{\rm em}(\nu')$ may not be significant, can be determined by a model. For example, it follows that the intensity ratio between two transitions from the same initial state ν' into the final states $\nu'' = a,b$ is constant (i.e., $A(\nu',\nu_a'')/A(\nu',\nu_b'') = \text{constant}$). By using the latest available spectroscopic measurements needed for quantum mechanical calculations of electron transition moments for a band system of N_2 or N_2^+, Gilmore et al. (1992) calculated vibrational and rotational constants, band origins, Frank–Condon factors,

and *R*-centroids, Einstein coefficients, for many band systems of nitrogen for several excited N_2 and N_2^+ states, and subsequently upgraded data were published by the same authors (Laher & Gilmore 1999), which is an improvement over the compiled data published earlier by Lofthus & Krupenie (1977). We expect the 2PB, 1NB, and MB to closely follow Franck–Condon excitation rates, except for a small variation of the electronic transition moment. Based on the published transition probabilities, $A(\nu',\nu'')$, by Laher & Gilmore (1999), the cross section for a weaker band (also for a strong or weak band in an extended wavelength range outside our VOIR measurement) is related to a known band emission cross section by branching ratios as

$$Q_{\mathrm{em\_weak}}(\nu',\nu'') = Q_{\mathrm{em\_expt}}(\nu',\nu'')\cdot A_{\mathrm{weak}}(\nu',\nu'')/A_{\mathrm{expt}}(\nu',\nu''). \quad (11)$$

Although we observed some of the weak bands within the instrument bandpass, cross sections of others outside the bandpass were determined by model calculations. We use a direct excitation model to obtain the emission cross sections for each ν'-progression that lies between 280 nm and 330 nm for 2PB and beyond 1100 nm for 1PB and MB. For this, we measure at least one strong emission from each ν'-progression and use branching ratios that have been published recently (Laher & Gilmore 1999) for the estimation of the total emission cross section for each progression.

3. RESULTS AND DISCUSSION

Figures 3(a) and (b) show an overview of the measured VOIR emission spectra for 25 eV and 100 eV electron impact on N_2, respectively, in the range from 330 nm to 1100 nm. The range covers the 2PB ($C\,^3\Pi_u(\nu') \rightarrow B\,^3\Pi_g(\nu'')$) and 1PB ($B\,^3\Pi_g^+(\nu') \rightarrow A\,^3\Sigma_g^+(\nu'')$) band systems of N_2, and the 1NB ($B\,^2\Sigma_u^+(\nu') \rightarrow X\,^2\Sigma_g^+(\nu'')$) and MB ($A\,^2\Pi_u(\nu') \rightarrow X\,^2\Sigma_g^+(\nu'')$) band systems of N_2^+, and line emissions of N I and N II multiplets. It is clear from the figures that the two electron-impact-induced spectra measured at 25 eV and 100 eV are dramatically different; the 25 eV spectrum, as compared to the 100 eV, is mostly dominated by the band emissions. The $C\,^3\Pi_u \rightarrow B\,^3\Pi_g$ and $B\,^3\Pi_g^+ \rightarrow A\,^3\Sigma_g^+$ systems of N_2 are strong at 25 eV because they are excited by singlet-triplet electron-exchange processes whose emission cross sections peak sharply at about twice the threshold energy (∼15 eV; Shemansky et al. 1995; Fons et al. 1996). In contrast, the $B\,^2\Sigma_u^+ \rightarrow X\,^2\Sigma_g^+$ and $A\,^2\Pi_u \rightarrow X\,^2\Sigma_g^+$ band systems of N_2^+ arise from simultaneous ionization and excitation and are dipole-allowed and strong at both 25 eV and 100 eV. As the electron-impact-ionization cross section of N_2 for N_2^+ ion production has a maximum around 100 eV, the N_2^+ emission cross sections also have a broader maximum near 100 eV of electron-impact energy (Simpson & McConkey 1969; Borst & Zipf 1970). Using our spectral model for each band system, we extend the vibrational spectra of N_2 to a lower wavelength of 200 nm allowing more complete coverage of the 2PB band system and to a longer wavelength of 1200 nm of the MB and 1PB to obtain a more complete set of vibrational cross sections for these two-band systems.

For clarity and more details of each band system and multiplets, high-resolution spectra in narrower wavelength windows in increasing order of wavelength for various emissions of N_2, N_2^+, N, and N^+ at 25 eV and 100 eV electron-impact energies are shown in Figures 4–16. The present high-resolution experimental setup has sufficient S/N to resolve the P, Q, and R branches (but insufficient to resolve fine structure due to Λ-doubling and sub-bands from spin-doublet and spin-triplet splitting) of the emitted molecular bands. Moreover, the imaging technique, which shows simultaneous recording of several spectral bands, provides several orders of magnitude improvement of signal strength with minimal temporal drifting over single particle scanning experiments. In the following subsections, we present the measured emission cross sections for vibrational bands (ν',ν'') separately for the 1PB ($B\,^3\Pi_g \rightarrow A\,^3\Sigma_u^+$) (Tables 9–12) and 2PB ($C\,^3\Pi_u \rightarrow B\,^3\Pi_g$) (Tables 1–4) systems of N_2, the 1NB ($B\,^2\Sigma_u^+ \rightarrow X\,^2\Sigma_g^+$) (Tables 5–8) and MB ($A\,^2\Pi_u \rightarrow X\,^2\Sigma_g^+$) (Tables 13–17) systems of N_2^+, and line emissions for N I and N II multiplets (Table 18) in the VOIR wavelength range. The cross-sectional tables for each of the four-band systems state explicitly which vibrational bands are observed and list them in the order of increasing (ν',ν''), likewise for the N I and N II emissions and their cross sections with increasing wavelength, and compare our data with the previously published results. Below we also discuss low-energy (10–100 eV) electron energy-loss spectroscopy which is the subject of intense activity in the last few years, allowing the comparison of (integral) vibrational and electronic cross sections of the $B\,^3\Pi_g$, $B\,^2\Sigma_g^+$, $A\,^3\Pi_u$, and $C\,^3\Pi_u$ states (Cartwright et al. 1977; Campbell et al. 2001; Khakoo et al. 2005; Malone et al. 2009) and $B\,^2\Pi_u$, $X\,^2\Sigma_g^+$, and $A\,^3\Sigma_u^+$ states to the emission cross sections of this study. Finally, we apply the results to the *Cassini* ISS planning for Titan eclipse observations.

3.1 Second Positive Band System $C\,^3\Pi_u(\nu') \rightarrow B\,^3\Pi_g(\nu'')$ of N_2

The emissions of the 2PB occur through dipole-allowed transitions between vibrational–rotational levels of the $C\,^3\Pi_u(\nu') \rightarrow B\,^3\Pi_g(\nu'')$ states of N_2. Direct excitation of the upper state $C\,^3\Pi_u$ of the 2PB system from the ground state $X\,^1\Sigma_g^+$ is forbidden since the molecule would be required to change its spin quantum number. Nonetheless, the $C\,^3\Pi_u$ state can be populated by electron-impact excitation from the ground state of N_2 ($X\,^1\Sigma_g^+$) by low-energy electrons via an electron-exchange process whose cross section peaks at nearly twice the threshold excitation energy (Shemansky et al. 1995). Figures 4, 5(a), 6, and 7(a) show 24 emission vibrational bands of the 2PB system from 330 nm to 500 nm, at both 25 eV and 100 eV electron-impact energy, displaying the 2PB dominance at 25 eV. Although there have been several measurements of 2PB reported in the past (Jobe et al. 1967; Burns et al. 1969; Aarts & De Heer 1969; Finn et al. 1972; Shaw & Campos 1983; Zubek 1994; Shemansky et al. 1995; Fons et al. 1996), only three of them have published emission spectra of partly resolved bands measured with medium resolving power; in the 290–410 nm range by Zubek (1994), in the 250–440 nm range by Shemansky et al. (1995), and more recently in the 330–420 nm range by Tohyama & Nagata (2005). The present spectrum, obtained with high-resolution ($\Delta\lambda = 0.07$ nm) resolving each vibrational band of 2PB over a broader wavelength range of 300–500 nm, is an extension to our previous medium-resolution measurements by Shemansky et al. (1995).

The $^3\Pi_u \rightarrow {}^3\Pi_g$ transitions occur with three sub-branches: $^3\Pi_{g0} \rightarrow {}^3\Pi_{u0}$ (a weak Q branch; Herzberg 1989), $^3\Pi_{g1} \rightarrow {}^3\Pi_{u1}$, and $^3\Pi_{g2} \rightarrow {}^3\Pi_{u2}$. For emissions with $\Delta\Lambda = 0$ but $\Lambda'' = \Lambda' \neq 0$, such as $^3\Pi \rightarrow {}^3\Pi$ ones, where Λ represents the component of the electronic orbital angular momentum L about the internuclear axis, bands are characterized by weak Q ($J'' = J'$) branches whose contribution is only 5% of the total emission (Maseberg & Gay 2010), and strong emissions with $\Delta J = \pm 1$ appear from P ($J'' = J' + 1$, $\Delta\Lambda = +1$) and R ($J'' = J' - 1$, $\Delta\Lambda = -1$) branches (Herzberg 1989),

Table 1
Electron-impact-induced Emission Cross Sections of N_2, $Q_{em}(v',v'')$ (in Units of 10^{-18} cm^2), for the Second Positive Band System $C\,^3\Pi_u(v') \rightarrow B\,^3\Pi_g(v'')$, along with Our Model[a] and Previously Published Data

Band (v',v'')	Band Head Wavelength λ (nm)	Present Data at 25 eV 100 eV	Model[a]	Jobe et al. (1967)	Burns et al. (1969)	Aarts & De Heer (1969)	Shaw & Campos (1983)	Shemansky et al. (1995)	Fons et al. (1996)	Tohyama & Nagata (2005)
(0,0)	337.21	2.81	2.81	3.13	3.30	2.41	4.14	2.58	3.0	3.0
		0.211	0.195	...	1.097	0.161	0.376	...	0.254	...
(0,1)	357.69	1.80	1.74	2.465	2.13		2.66	1.865	1.923	2.02
		0.13	0.131	...	0.707			...		...
(0,2)	380.50	0.68	0.698	1.276	0.756		0.998	0.742	0.764	0.80
		0.056	0.0521	...	0.251			...		...
(0,3)	405.92	0.227	0.216	0.348	0.333		0.295	0.212	0.246	
		0.0165	0.0161	...	0.110			...		
(0,4)	434.36	0.063	0.0566		0.053		0.069	0.059	0.064	
		0.0042[a]	0.0042		0.018			...		
(0,5)	466.61	0.013[a]	0.0134				0.0240		0.012	
		Weak	0.001							
(0,6)	503.20	0.0050[a]	0.003							
		0.000	0.0002							
(1,0)	315.80	1.95[a]	1.89	2.49	1.82		3.03	1.467	1.968	
		0.147[a]	0.141		0.604			...		
(1.1)	333.85	0.086	0.0791	0.145	0.098		0.142	0.097	0.085	
		0.003	0.0059		0.032			...		
(1,2)	353.62	0.785	0.716	0.90	0.803		1.144	0.803	0.885	
		0.0307	0.0535		0.267			...		
(1,3)	375.46	0.750	0.730	0.90	0.722		0.80	0.70	0.846	
		0.0420	0.0471		0.234			...		
(1,4)	399.75	0.312	0.308	0.64	0.395		0.435	0.325	0.315	
		0.092	0.023		0.131			...		
(1,5)	426.80	0.138[a]	0.113	0.174	0.137		0.177	0.119	0.0984	
		0.144	0.0084		0.045			...		
(1,6)	457.31	0.0321	0.0348	0.075	0.030		0.0487	...	0.0413	
		0.0024	0.0026		0.010					
(1,7)	491.79	0.011	0.0095	0.035			0.0184	...	0.009	
		0.0012	0.0007							
(2,0)	297.6	0.198[a]	0.139	0.319	0.218		0.487		0.26	
		0.0148[a]	0.0104		0.072					
(2,1)	313.5	0.5124	0.360	0.928	0.532		1.00		0.65	
		0.0383.	0.027		0.177					
(2,2)	330.9	0.0382	0.0268	0.058	0.504		0.08		0.0474	
		0.0029	0.0020		0.017					
(2,3)	349.9	0.0885	0.0623	0.102	0.081		0.139		0.091	
		0.0066.	0.0047		0.027					
(2,4)	371.0	0.216	0.1440	0.290	0.204		0.295		0.247	
		0.0154	0.0108		0.068					
(2,5)	394.24	0.148	0.1110	0.290	0.168		0.271		0.162	
		0.0103	0.0083		0.056					
(2,6)	420.0	0.0506	0.0550	0.127	0.075		0.118		0.059	
		0.0038	0.0041		0.025					
(2,7)	448.94	0.0320	0.0213	0.061	0.027		0.0487		0.036	
		0.0012	0.0016		0.009					
(3,0)									0.010	
		...								
(3,1)									0.140	
		...								
(3,2)									0.115	
		...								
(3,3)									0.056	
		...								
(3,4)									...	
		...								
(3,5)									0.045	
		...								
(3,6)									0.0476	
		...								
(3,7)	414.04	0.032							0.035	
		...								

Table 1
(Continued)

Band (ν',ν'')	Band Head Wavelength λ (nm)	Present Data at 25 eV 100 eV	Model[a]	Jobe et al. (1967)	Burns et al. (1969)	Aarts & De Heer (1969)	Shaw & Campos (1983)	Shemansky et al. (1995)	Fons et al. (1996)	Tohyama & Nagata (2005)
(3,8)	441.41	...							0.0154	
		...								
(3,9)	472.25	...							0.0067	
		...								

Notes. In each (ν',ν'') row, the top values represent $Q_{em}(\nu',\nu'')$ at 25 eV and the bottom values represent at 100 eV electron-impact energy.
[a] Model results are based on Frank–Condon factors and branching ratios of Gilmore et al. (1992).

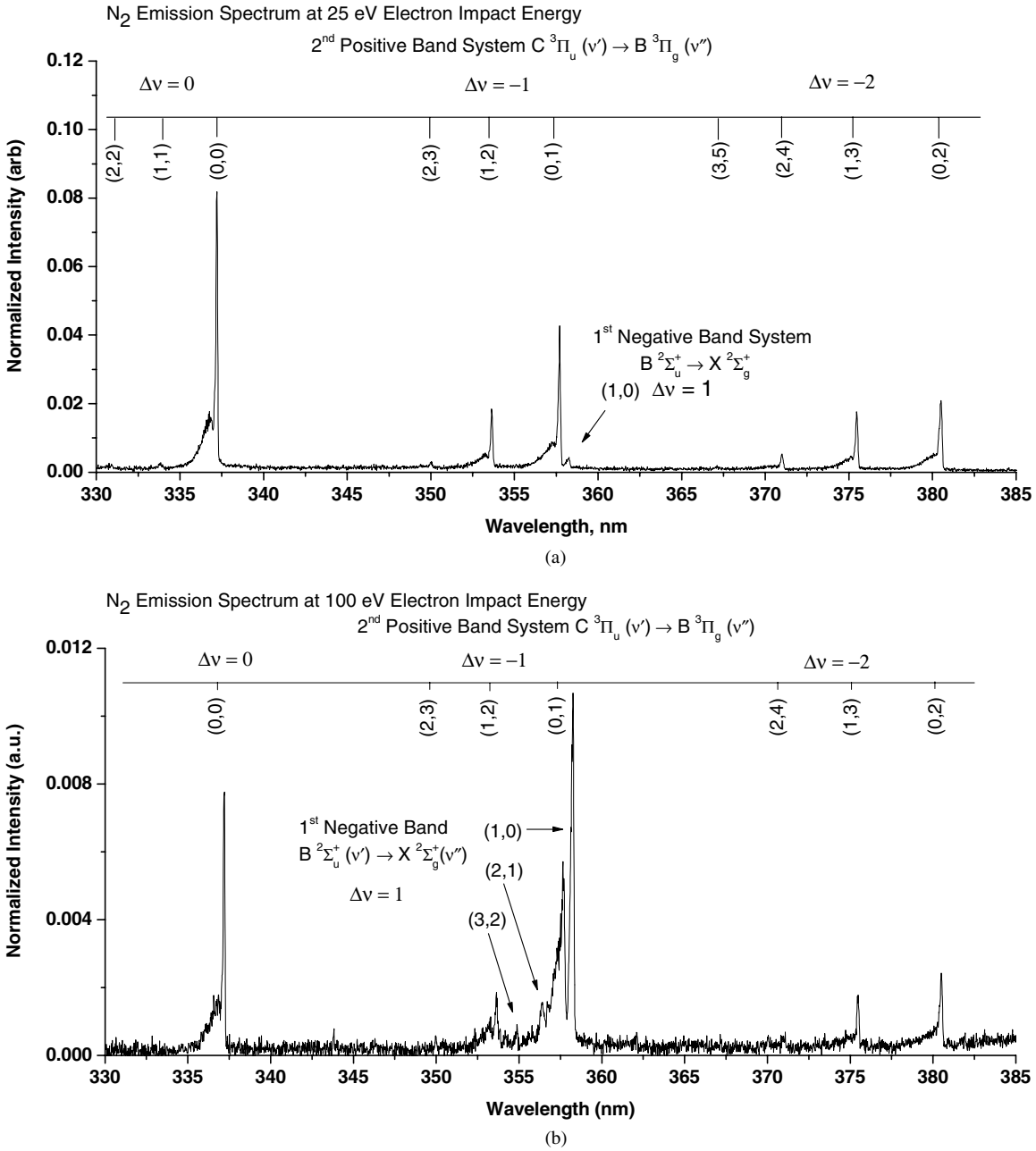

Figure 4. Calibrated electron-impact-induced fluorescence spectrum of N_2 from 330 nm to 385 nm for electron energy of 25 eV (a) and 100 eV (b) identifying the vibrational bands and sequences of the second positive band system $C\ ^3\Pi_u(\nu') \rightarrow B\ ^3\Pi_g(\nu'')$ and first negative band system $B\ ^2\Sigma_u^+(\nu') \rightarrow A\ ^3\Sigma_g^+(\nu'')$ at a spectral resolution of 0.07 nm (FWHM) with a spectrometer resolving power of $\lambda/\Delta\lambda \approx 10000$.

where J' and J'' are rotational quantum numbers of the upper and lower states, respectively. According to the Grotrian diagram of potential energy curves of various electronic states of N_2 and N_2^+ (Gilmore et al. 1992) shown in Figure 1, the upper

Table 2
Relative Emission Cross Sections with respect to the Strong Emission Band in Each $\nu' = 0, 1, 2, 3$ for the Second Positive Band System $C\,^3\Pi_u \rightarrow B\,^3\Pi_g$ of N_2

Band (ν',ν'')	Present	Model	Jobe et al. (1967)	Burns et al. (1969)	Shaw & Campos (1983)	Shemansky et al. (1995)	Fons et al. (1996)	Tohyama & Nagata (2005)
(0,0)	1.00	1.00	1.00	1.00	1.00	1.00	1.00	1.00
(0,1)	0.64	0.62	0.79	0.64	0.64	0.705	0.63	0.674
(0,2)	0.242	0.248	0.41	0.23	0.24	0.286	0.25	0.290
(0,3)	0.080	0.077	0.11	0.10	0.071	0.086	0.081	0.110
(0,4)	0.022	0.020	0.031	0.016	0.017		0.021	
(0,5)	0.0046	0.0047	0.011		0.059		0.0039	
(1,0)	1.00	1.00	1.00	1.00	1.00	1.00	1.00	1.00
(1.1)	0.044	0.042	0.058	0.054	0.047	0.065	0.043	0.042
(1,2)	0.40	0.38	0.36	0.44	0.38	0.537	0.45	0.527
(1,3)	0.385	0.386	0.36	0.40	0.26	0.473	0.43	0.425
(1,4)	0.16	0.163	0.26	0.22	0.14	0.224	0.16	0.273
(1,5)	0.07	0.06	0.070	0.075	0.058		0.050	
(1,6)	0.0165	0.0184	0.030	0.016	0.016		0.021	
(1,7)	0.0056	0.005	0.014		0.0061		0.0045	
(2,0)	0.386	0.385	0.34	0.41	0.48	0.293	0.40	
(2,1)	1.00	1.00	1.00	1.00	1.00	1.00	1.00	1.00
(2,2)	0.075	0.074	0.063	0.095	0.079	0.087	0.073	
(2,3)	0.173	0.173	0.11	0.15	0.14	0.19	0.14	
(2,4)	0.42	0.40	0.31	0.39	0.29	0.42	0.38	0.29
(2,5)	0.29	0.308	0.31	0.20	0.27	0.317	0.25	0.30
(2,6)	0.10	0.153	0.14	0.14	0.12		0.091	
(2,7)	0.062	0.059	0.066	0.049	0.048		0.055	

Table 3
Total Emission Cross Section, $Q_{em}(\nu')$ (in Units of 10^{-18} cm^2), as Defined in Equation (3), for Transitions from Vibrational–Rotational Level ν' of the Upper State $C\,^3\Pi_u$ into the Lower State $B\,^3\Pi_g$ of the Second Positive Band System of N_2 at 25 eV and 100 eV

(ν')	Present at 25 eV 100 eV	Model	Jobe et al. (1967)	Burns et al. (1969)	Shaw & Campos (1983)	Shemansky et al. (1995)	Fons et al. (1996)
0	5.598	5.346	7.219	6.572	8.186	5.468	6.009
	0.418	0.400	...	...	...	...	...
1	4.01	3.41	5.359	4.005	5.795	3.511	4.248
	0.348	0.255	...	1.323	...	...	...
2	1.263	0.919	1.591	1.809	2.439		1.5524
	0.093	0.069	0.379	0.451	...		...
3	0.032						0.4707
	...						...

Notes. A comparison is shown with previously published results. In each row, the top values represent $Q_{em}(\nu')$ at 25 eV and the bottom values represent at 100 eV electron-impact energy.

Table 4
Comparison of the Total Emission Cross Sections, $Q_{em}(\nu' = 0–3)$ (in Units of 10^{-18} cm^2), for the Second Positive Band System $C\,^3\Pi_u \rightarrow B\,^3\Pi_g$ at Several Electron-impact Energies Listed Below

Electron-impact Energy (eV)	Present	Model	Jobe et al. (1967)	Burns et al. (1969)	Cartwright et al. (1977)	Shaw & Campos (1983)	Shemansky et al. (1995)	Fons et al. (1996)	Campbell et al. (2001)	Malone et al. (2009)
20					11.8				16.1	
25	10.87	10.04	14.17	12.386		16.42	8.98	11.81		8.41
30									9.5	
100	0.859	0.78								0.495

excited state $C\,^3\Pi_u$ of 2PB has an internuclear distance R (Å) smaller than that of the lower state $B\,^3\Pi_g$, i.e., their minima occur at $R_C < R_B$. As a result, the rotational line spacing decreases with J in the P branch and increases with J in the R branch. In such case, the rotational constants $B_{\nu'} - B_{\nu''}$ become positive (i.e., $B_{\nu'} > B_{\nu''}$) for the P branch; hence, the sharp band head appears in the P branch compared to the R branch, for which $B_{\nu'} - B_{\nu''}$ is negative (i.e., $B_{\nu'} < B_{\nu''}$; Herzberg 1989). The $B_{\nu'}$ and $B_{\nu''}$ are the rotational constants of the upper and lower states, respectively. This is clear from Figures 4–6, which show that the 2PB system exhibits strong P and R branches with a sharp band head in the P branch and a broader R branch stretching toward blue wavelengths. Although the R branch has a broader wavelength spread, the present spectral resolution $\Delta\lambda \approx 0.07$ nm is not sufficient to resolve the rotational structure of the 2PB system. However, in the cases of other

Table 5
Emission Cross Sections, $Q_{em}(\nu',\nu'')$ (in Units of 10^{-18} cm^2), for the First Negative Band System $B\,^2\Sigma_u^+(\nu') \rightarrow X\,^2\Sigma_g^+(\nu'')$ of N_2^+ along with Our Model[a] and Previously Published Data

Band (ν',ν'')	Band Head Wavelength λ (nm)	Present Cross Sections at 25 eV 100 eV	Present Model	McConkey & Latimer (1965)	Nishimura (1968)	Aarts et al. (1968)	Srivastava & Mirza (1968a, 1968b)	Stanton & St. John (1969)	Borst & Zipf (1970)	Shaw & Campos (1983)
(0,0)	391.44	2.88	2.88	2.90	...	...	...	...	3.89	...
		14.90	14.90	15.0	17.4	21.2	16.8	15.6	17.4	15.4
(0,1)	427.81	1.20	0.940	0.928	...	...	...	...	...	...
		5.88	4.850	4.8	6.0	6.784	5.712			5.35
(0,2)	470.94	0.24	0.197	0.36	...	...	...	...	...	...
		1.34	1.020	1.125	0.870	1.272	1.092			0.92
(0,3)	522.82	0.029	0.034	...	...	...	...	...	...	...
		0.209	0.175		...	0.214				
(0,4)	586.50	0.005[a]	0.005	...	...	...	...	...	...	...
		0.030	0.027							
(0,5)	666.20	0.002	0.001							
		0.008	0.007							
(1,0)	358.26	0.20	0.170	...	...	...	...	...	...	...
		0.78	0.881		1.53					
(1.1)	388.46	0.15	0.120	...	...	...	...	...	...	...
		0.642	0.620		1.018				0.650	1.018
(1,2)	423.66	0.175	0.127	...	...	...	...	...	...	...
		0.72	0.654			0.933				0.78
(1,3)	465.21	0.066	0.047	...	...	...	...	...	...	...
		0.305	0.240			0.297				0.22
(1,4)	514.91	0.014	0.014	...	...	...	...	...	...	...
		0.069	0.069							
(1,5)	575.30	0.003	0.002	...	...	...	...	...	...	...
		0.023	0.005							
(2,0)	330.81	0.002	0.003	...	...	...	...	...	...	...
		0.019	0.017							
(2,1)	356.42	0.016	0.030	...	...	...	...	...	...	...
		0.170	0.148							
(2,2)	385.83	0.002[a]	0.004	...	...	...	...	...	...	...
		0.020	0.018							
(2,3)	419.95	0.007	0.013	...	...	...	...	...	...	...
		0.075	0.065							
(2,4)	460.01	0.004	0.008	...	...	...	...	...	...	...
		0.042	0.038							
(2,5)	507.74	0.003[a]	0.0025	...	...	...	...	...	...	...
		0.038	0.012							
(3,5)	455.62	0.006[a]	0.009	...	...	...	...	...	...	...
		0.03	0.040							
(4,6)	451.70	0.002[a]	0.0015	...	...	...	...	...	...	...
		0.01	0.001	...	...	...	...	...	...	...

Notes. In each (ν',ν''), row the top values represent $Q_{em}(\nu',\nu'')$ at 25 eV and the bottom values represent 100 eV electron-impact energy.
[a] Model results are based on Frank–Condon factors and branching ratios of Gilmore et al. (1992).

three band systems, 1NB ($B\,^2\Sigma_u^+ \rightarrow X\,^2\Sigma_g^+$), 1PB ($B\,^3\Pi_g \rightarrow A\,^3\Sigma_u^+$), and MB ($B\,^2\Pi_u \rightarrow X\,^2\Sigma_g^+$), as discussed in Sections 3.2, 3.3, and 3.4, respectively, the present spectral resolution is effective in resolving the rotational emission structures of N_2 at ~300 K.

We have observed 24 emission bands (ν',ν''), corresponding to the sequences of $\Delta v = -1$ through -6, from the $\nu' = 0$–4 and $\nu'' = 0$–9 vibrational levels of the 2PB. The 2PB band system predissociates beyond $\nu' = 4$ (Lofthus & Krupenie 1977). The emission cross sections, $Q_{em}(\nu',\nu'')$, for each band emission of the $C\,^3\Pi_u(\nu') \rightarrow B\,^3\Pi_g(\nu'')$ system at both 25 eV and 100 eV are listed in Table 1 along with the available data in the literature for comparison. In the previously published data, either the peak energy (~14–15 eV) cross section for only the (0,0) band and a normalized emission curve of it as a function of electron-impact energy (Burns et al. 1969; Aarts & De Heer 1969; Shemansky et al. 1995) or the cross sections and emission curves for a few selected bands with a limited electron energy range (Jobe et al. 1967; Fons et al. 1996; Tohyama & Nagata 2005) were provided. Hence, we have extracted emission cross-sectional values at 25 eV and 100 eV from the published excitation functions and peak cross-sectional values. The values so obtained are given in Table 1 for comparison with our cross-sectional values. As the $Q_{em}(\nu',\nu'')$ values fall very rapidly at 100 eV compared to the value at 25 eV (by more than an order of magnitude), in order to avoid excessive uncertainty we did not attempt to extract 100 eV cross sections for weaker bands from published excitation functions in cases where the relative

Table 6
Relative Emission Cross Sections with respect to the Strong Emission Band for Each $\nu' = 0$–4 for the First Negative Band System $B\,^2\Sigma_u^+ \rightarrow X\,^2\Sigma_g^+$ of N_2^+

Band (ν',ν'')	Present	Model	McConkey & Latimer (1965)	Nishimura (1968)	Aarts et al. (1968)	Srivastava & Mirza (1968a, 1968b)	Stanton & St. John (1969)	Borst & Zipf (1970)	Shaw & Campos (1983)
(0,0)	1.00	1.00	1.00	1.00	1.00	1.00	1.00	1.00	1.00
(0,1)	0.395	0.325	0.32	0.345	0.32	0.34			0.35
(0,2)	0.09	0.07	0.075	0.05	0.06	0.065			0.06
(0,3)	0.014	0.0117							
(0,4)	0.002	0.0018							
(0,5)	0.0005	0.00047							
(1,0)	1.00	1.00							
(1.1)	0.823	0.704							
(1,2)	0.923	0.742							
(1,3)	0.391	0.272							
(1,4)	0.0885	0.0783							
(1,5)	0.295	0.0057							
(2,0)	0.111	0.115							
(2,1)	1.00	1.00							
(2,2)	0.117	0.121							
(2,3)	0.44	0.44							
(2,4)	0.282	0.257							
(2,5)	0.223	0.081							
(3,5)	1.00	1.00							
(4,6)	1.00	1.00							

Table 7
Total Emission Cross Section, $Q_{em}(\nu') = \Sigma Q_{em}(\nu',\nu'')$ (in Units of 10^{-18} cm^2) for Transitions of the First Negative Band System of N_2^+ from an Upper State $B\,^2\Sigma_u^+$ Vibrational–Rotational Level ν' into the Lower State $X\,^2\Sigma_g^+$ at 25 eV and 100 eV

(ν')	Present at 25 eV 100 eV	Model	McConkey & Latimer (1965)	Nishimura (1968)	Aarts et al. (1968)	Srivastava & Mirza (1968a, 1968b)	Borst & Zipf (1970)	Shaw & Campos (1983)
0	4.344	4.057	4.188	...	...	...	3.89	...
	22.367	20.973	20.925	26.818	29.47	23.604	17.4	22.768
1	0.608	0.478		...	...			...
	2.539	2.467		1.018	1.23		0.650	2.018
2	0.032	0.060						
	0.37	0.298						
3	0.006	0.009						
	0.03	0.004						
4	0.002	0.0015						
	0.01	0.001						

Notes. A comparison is made with previously published results. In each row, the top values represent $Q_{em}(\nu')$ at 25 eV and the bottom values represent at 100 eV electron-impact energy.

$Q_{em}(v, \nu')$ were not listed. A comparative study from Table 1 shows a wide disagreement among the various results. Recently, Itikawa (2006) reviewed the shape of the excitation function of the (0,0) band of the 2PB system obtained by various researchers and found large discrepancies, including the peak energy values, among the published data. Shemansky et al. (1995) reported the 2PB system emissions rise sharply from the emission threshold as a function of electron-impact energy and fall from the peak (~14–15 eV) very rapidly within a small impact energy range, and they determined the full width at half-maximum (FWHM) of the excitation function curve of the (0,0) band to be only ~4.35 eV. In such cases, energy resolution of the electron beam becomes an important requirement for determining the ratio of cross sections at different electron-impact energies, which could be one of the reasons for the large discrepancies among the various published values of cross sections and peak electron-impact energy. The peak cross-sectional values of the 2PB system have been determined previously either by absolute measurements of experimental parameters, such as calibration of the optical spectrometer using tungsten-ribbon standard lamp, gas pressure, electron-beam current and energy, etc., that define the cross section (Jobe et al. 1967; Aarts & De Heer 1969), or by normalizing the 2PB (0,0) band with respect to the known cross section of the 1NB (0,0) band of N_2^+ (Burns et al. 1969; Shemansky & Broadfoot 1971) or to the He (5^1S–2^1P) transition by Shaw & Campos (1983). The average peak cross-sectional value among them is $(11.28 \pm 0.29) \times 10^{-18}$ cm^2, but their cross sections differ significantly at higher electron-impact energies, which could be due to poor energy resolution or excessive gas pressure or higher electron-beam currents causing the presence of secondary electrons or all of these effects in some cases. Particularly, due to the fact that singlet-triplet excitation of the 1PB and 2PB systems leads to low-energy emission thresholds, the target gas pressure and electron-beam current become factors in cross-sectional errors, because of scattered secondary electrons in the collision region

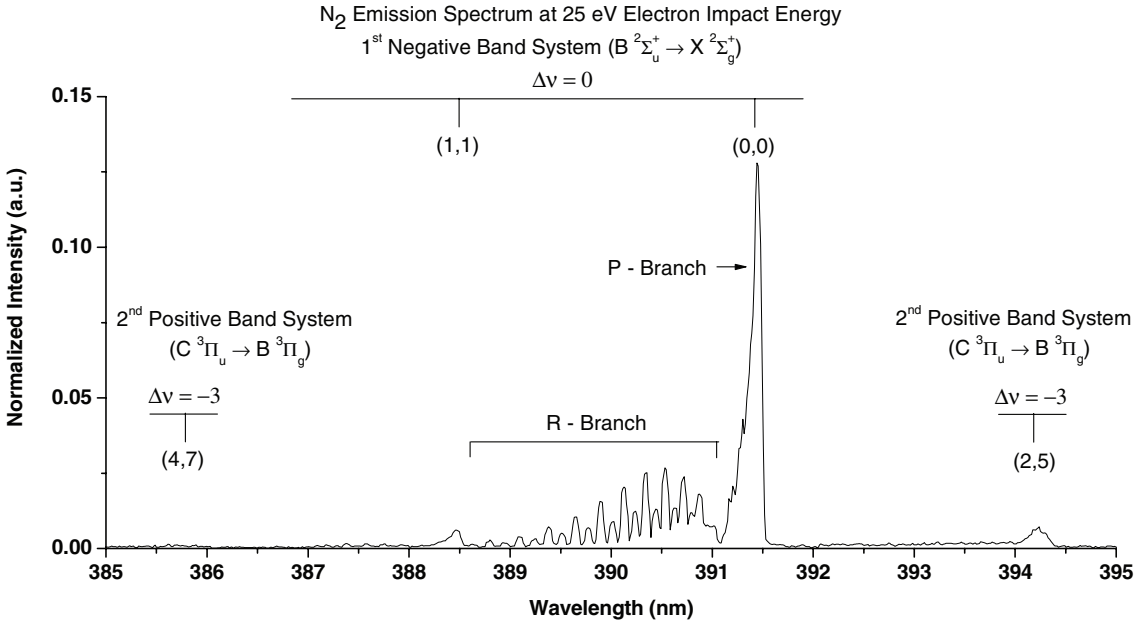

(a)

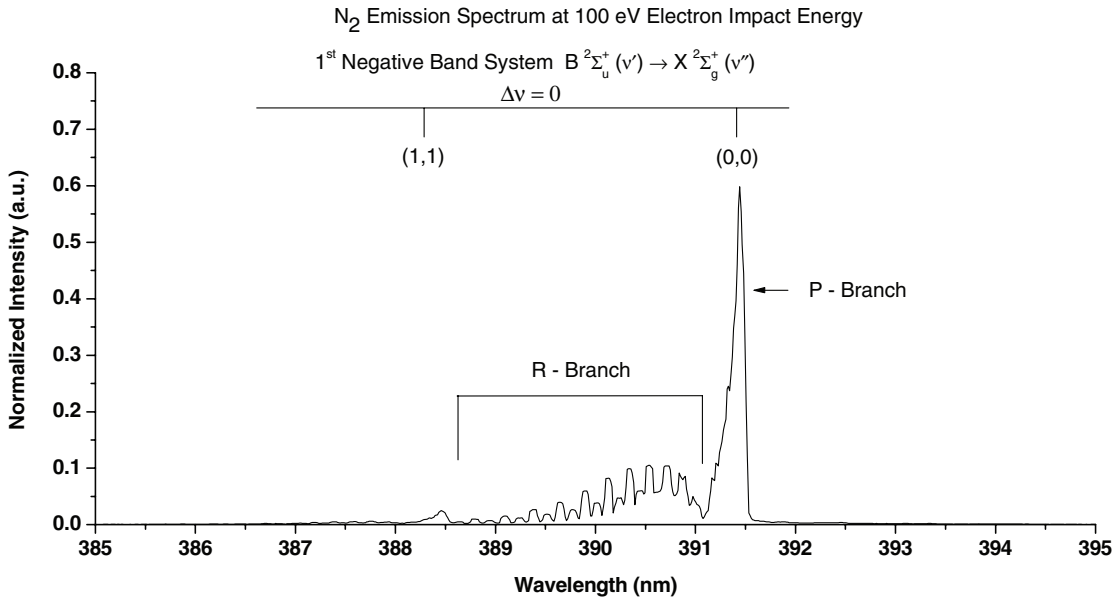

(b)

Figure 5. Calibrated electron-impact-induced fluorescence spectrum of N_2 from 385 nm to 395 nm for electron energy of 25 eV (a) and 100 eV (b) identifying the vibrational bands and sequences of the second positive band system $C\ ^3\Pi_u(\nu') \rightarrow B\ ^3\Pi_g(\nu'')$ and first negative band system (1NB) $B\ ^2\Sigma_u^+(\nu') \rightarrow A\ ^3\Sigma_g^+(\nu'')$ at a spectral resolution of 0.07 nm (FWHM) with a spectrometer resolving power of $\lambda/\Delta\lambda \approx 10000$ showing the detailed rotational structure of 1NB.

at higher electron-impact energies. Moreover, a single-collision condition, operating at lower pressures ($<10^{-5}$ Torr) is very important for the 2PB system; otherwise the possibility of contribution of collisional cascading from metastable states, such as $E\ ^3\Sigma_g^+$, $C'\ ^3\Pi_u$, and $D\ ^3\Sigma_u^+$, lying above the upper state $C\ ^3\Pi_u$ state of 2PB could become relevant (Burns et al. 1969; Shemansky et al. 1995; Poparic 2008).

Extensive measurements have been reported by Fons et al. (1996), who measured cross sections for more upper state vibrational levels $\nu' = 0$–4 to several lower state levels ν'' (0–9) as compared to other researchers, except those of Shemansky et al. (1995). They also provided excitation functions for at least one ν' (= 0, 1, 2, 3) from emission threshold to 100 eV. They observed linearity of emission intensity with respect to electron-beam current but definite nonlinearity with pressure at values above 2×10^{-3} Torr. More recent data presented by Tohyama &

Table 8
Comparison of the Total Emission Cross Sections (in Units of 10^{-18} cm^2), $Q_{em}(\nu' = 0$–$4)$, for the First Negative Band System $B\ ^2\Sigma_u^+ \rightarrow X\ ^2\Sigma_g^+$ of N_2^+ with Electron Excitation Cross Sections Q_{ex} at Several Electron-impact Energies

Electron-impact Energy (eV)	Present	Model	Shemansky & Liu (2005)
20			4.32
25	4.984	4.595	
100	25.316	23.738	23.21

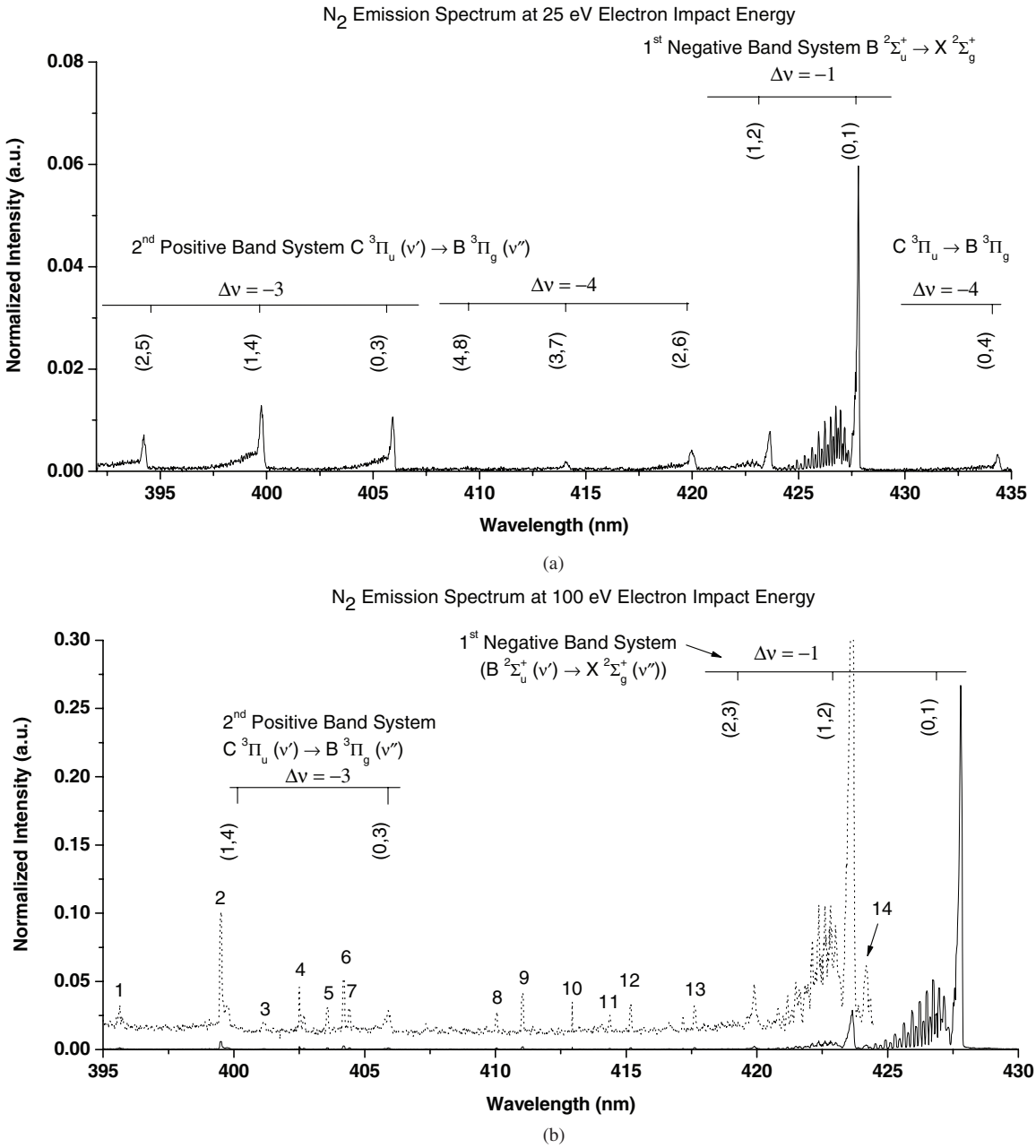

Figure 6. Calibrated electron-impact-induced fluorescence spectrum of N_2 from 390 nm to 435 nm for electron energy of 25 eV (a) and from 390 nm to 430 nm for 100 eV (b) identifying the vibrational bands and sequences of the second positive band system $C\ ^3\Pi_u(v') \rightarrow B\ ^3\Pi_g(v'')$ and first negative band system (1NB) $B\ ^2\Sigma_u^+(v') \rightarrow A\ ^3\Sigma_g^+(v'')$ with detailed rotational structure of it at a spectral resolution of 0.07 nm (FWHM) with a spectrometer resolving power of $\lambda/\Delta\lambda \approx 10000$. The dotted line in (b) is a part of the same spectrum magnified (multiplied by 15 and shifted upward for clarity) to show the line emissions of N I and N II multiplets as listed in Table 18.

Nagata (2005), who measured absolute cross sections for v' (=0, 1, 2) to several v'' (=0, 1, 2, . . .) levels and presented excitation functions for the (0,0) and (0,2) bands from threshold to 50 eV, and also reported the nonlinearity of emissions at pressures as low as 1×10^{-4} Torr.

The two strong bands (0,0) and (0,1) of the 2PB system, whose cross-sectional values at 25 eV are 2.81×10^{-18} cm^2 and 1.80×10^{-18} cm^2, respectively, agree well with the values of 2.58×10^{-18} cm^2 and 1.86×10^{-18} cm^2 measured in our laboratory earlier by Shemansky et al. (1995), as well as the values of 3.0×10^{-18} cm^2 and 1.92×10^{-18} cm^2 obtained by Fons et al. (1996), and 3.0×10^{-18} cm^2 and 2.02×10^{-18} cm^2 of Tohyama & Nagata (2005). Furthermore, the emission cross section of the (0,0) band between 25 eV (e.g., 2.81×10^{-18} cm^2) and 100 eV (e.g., 0.211×10^{-18} cm^2) electron-impact energies falls off by a factor of 13.32, in close agreement with our model and with experimental values obtained earlier by Shemansky et al. (1995) which showed a falloff factor of 14, but somewhat different from the values 12 of Fons et al. (1996), 11 of Shaw & Campos (1983), 21 of Aarts & De Heer (1969), and 17.0 of Malone et al. (2009), whereas Burns et al. (1969) reported a remarkably low ratio of 3. Our goal in the previous paper by Shemansky et al. (1995) was a careful study of the threshold region. This ratio is important for determining if effects of low-energy secondary electrons might be present at 100 eV. The emission cross sections can be compared to the model from Equation (3), which is normalized

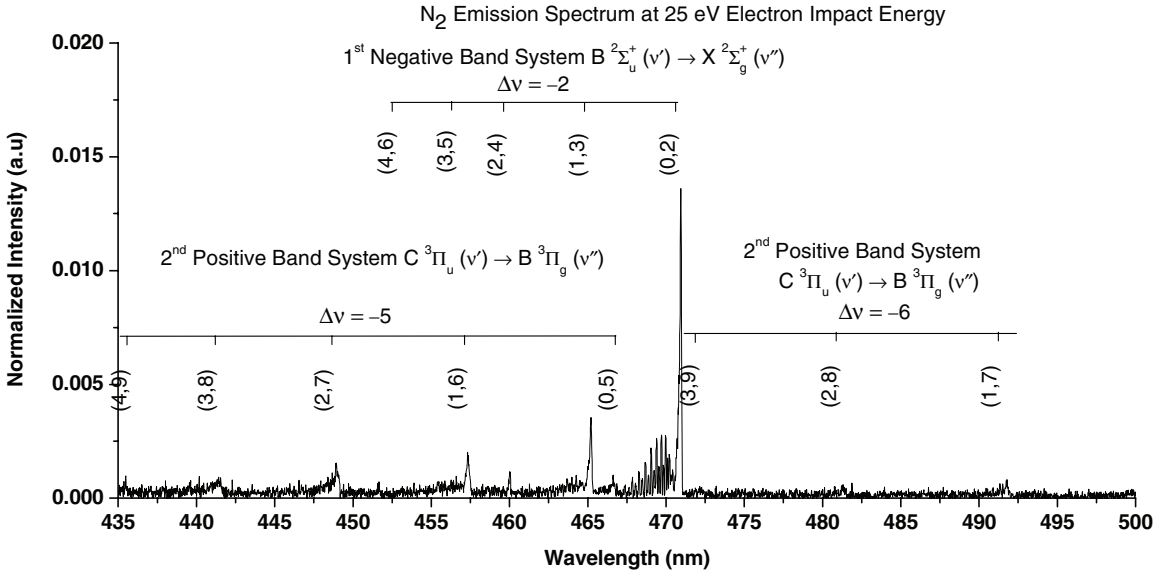

(a)

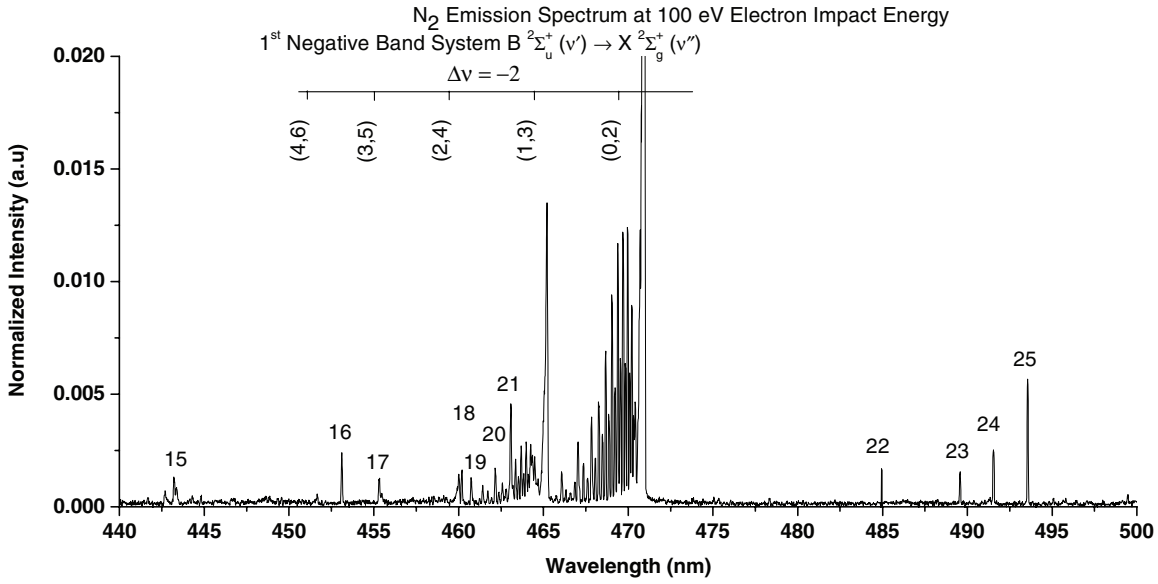

(b)

Figure 7. Calibrated electron-impact-induced fluorescence spectrum of N_2 from 435 nm to 500 nm for electron energy of 25 eV (a) covering the second positive $C\ ^3\Pi_u(\nu') \rightarrow B\ ^3\Pi_g(\nu'')$ and the first negative band systems, and from 440 nm to 500 nm for 100 eV (b) showing the first negative band system (1NB) $B\ ^2\Sigma_u^+(\nu') \rightarrow A\ ^3\Sigma_g^+(\nu'')$ at a spectral resolution of 0.07 nm (FWHM) with a spectrometer resolving power of $\lambda/\Delta\lambda \approx 10000$, identifying vibrational bands and sequences with detailed rotational structure of 1NB as well as line emissions of N I, II, III multiplets as listed in Table 18.

to the 2PB (0,0) band measured emission cross section. The agreement between experiment and model for the band emission cross sections is excellent showing that cascade is unimportant and that the excitation is proportional to Frank–Condon factors multiplied by the square of the electronic transition moment, as demonstrated by Shemansky et al. (1995). Although there is some disagreement in the absolute values of emission cross sections among various measurements, from a physics point of view it is important to determine the branching ratios of the 2PB system emission bands. In Table 2, we list the relative values of various bands of the $C \rightarrow B$ transition with respect to a strong (ν',ν'') band emission in ascending order of upper vibrational level ($\nu' = 0$–3) for comparison with their respective branching ratios as determined from model calculations (Laher & Gilmore 1999). The agreement is somewhat scattered among the data; our values are fairly close to those measured by Shaw & Campos (1983) and Fons et al. (1996).

In the absence of predissociation and significant cascading to the $C\ ^3\Pi_u$ state, the total vibrational excitation cross section is nearly equal to the total vibrational emission cross section (Equation (9)). To determine the total vibrational and electronic cross sections, contributions from below our measured wavelength range at 25 eV and 100 eV for (ν',ν'') from $\nu' = 4$ and $\nu'' = 7$ are estimated using our model. The results of our optical-emission cross sections are compared with those from other laboratories in Table 3 for each ν' of the upper state $C\ ^3\Pi_u$ into several ν'' levels of the lower state $B\ ^3\Pi_g$. We find from Table 3 that the total emission cross section at 25 eV and 100 eV is mostly dominated by the total vibrational emission cross sections of $\nu' = 0$ and 1, with contributions of ~50% and 38%

Table 9
Emission Cross Sections, $Q_{em}(\nu',\nu'')$ (in Units of 10^{-18} cm^2), for the First Positive Band System $B\,^3\Pi_g(\nu') \rightarrow A\,^3\Sigma_u^+(\nu'')$ of N_2 along with Our Model[a] and Previously Published Results

Band (ν',ν'')	Band Head Wavelength λ (nm)	Present Data at 25 eV 100 eV	Model[a]	Stanton & St. John (1969)	McConkey & Simpson (1969)
(0,0)	1050.825	3.50	2.450	0.944	...
		0.455	0.319	...	...
(1,0)	891.31	8.87	8.87	2.32	...
		1.15	1.15	...	...
(2,0)	775.314	4.60	5.60	2.05	2.0
		0.611	0.730	...	...
(2,1)	868.22	6.46	7.24	2.27	...
		0.841[a]	0.943	...	...
(2,2)	988.906	1.25	1.35	0.472	...
		0.162[a]	0.175	...	...
(3,0)	687.50	1.07	1.30	0.42	0.60
		0.139[a]	0.169	...	
(3,1)	762.67	5.90	8.52	2.65	3.15
		0.920	1.11	...	...
(3,2)	854.28	2.08	2.23	0.730	...
		0.290	0.290	...	...
(3,3)	968.00	2.55	2.69	0.944	...
		0.355[a]	0.350	...	...
(4,0)	618.683	0.178	0.131	...	...
		0.012[a]	0.017	...	...
(4,1)	678.885	2.39	2.68	0.940	1.25
		0.323	0.350	...	...
(4,2)	750.43	5.20	6.73	2.33	2.75
		0.68	0.877	...	...
(4,3)	837.02	0.095[a]	0.123	...	...
		0.012[a]	0.0155	...	...
(4,4)	943.64	1.56	2.02	...	...
		0.204[a]	0.268	...	...
(4,5)	1075.61	0.45	0.501	...	...
		0.06	0.0653	...	...
(5,1)	612.727	0.32	0.337	0.124	0.11
		0.0415	0.0439	...	...
(5,2)	670.451	2.40	3.04	1.116	1.50
		0.343	0.397	...	...
(5,3)	738.72	2.84	3.60	1.30	1.50
		0.370	0.468	...	...
(6,2)	606.986	0.377	0.482	0.206	0.165
		0.0489	0.0628	...	...
(6,3)	662.358	2.02	2.49	1.08	1.35
		0.294	0.324	...	...
(6,4)	727.352	1.62	1.39	0.622	0.705
		0.21[a]	0.182	...	...
(6,5)	804.570	0.418	0.445	...	...
		0.054[a]	0.058	...	...
(7,3)	601.359	0.43	0.488	0.220	0.18
		0.078	0.0636	...	...
(7,4)	654.480	1.49	1.60	0.708	0.91
		0.194[a]	0.209	...	...
(7,5)	715.289	0.448	0.367	0.189	...
		0.058	0.0478	...	...
(7,6)	789.700	0.513	0.455	...	...
		0.065	0.059	...	...
(8,4)	595.897	0.370	0.406	0.172	0.145
		0.050[a]	0.053	...	...
(8,5)	646.855	0.917	0.875	0.403	0.455
		0.019	0.0114	...	...
(9,5)	590.624	0.295	0.306	0.133	0.11
		0.041[a]	0.053	...	...

Table 9
(Continued)

Band (ν',ν'')	Band Head Wavelength λ (nm)	Present Data at 25 eV 100 eV	Model[a]	Stanton & St. John (1969)	McConkey & Simpson (1969)
(9,6)	639.458	0.520	0.432	0.202	...
		0.0674	0.0563	...	...
(10,6)	585.478	0.179	0.189	0.094	0.08
		0.023[a]	0.0247	...	...
(10,7)	631.732	0.150	0.177	0.106	...
		0.019[a]	0.023	...	...
(11,7)	580.369	0.151	0.183	0.073	0.055
		0.02[a]	0.024	...	...
(11,8)	626.877	...	0.091	0.052	...
		...	0.012		...
(12,8)	575.450	0.155	0.202	0.06	...
		0.026	0.026	...	...
(13,9)	568.369	0.0527	0.212	...	...
		0.007[a]	0.026	...	...

Notes. In each (ν',ν'') row, the top values represent $Q_{em}(\nu',\nu'')$ at 25 eV and the bottom values represent at 100 eV electron-impact energy.

[a] Model results are based on Frank–Condon factors and branching ratios of Gilmore et al. (1992).

of the total of the 2PB emissions, respectively. Since the 1PB ($B\ ^3\Pi_g \rightarrow A\ ^3\Sigma_u^+$) transition is the only radiative decay channel for the $C\ ^3\Pi_u$ state, summation of the emission cross sections of the (ν',ν'') band progression over ν'' gives the total emission cross section of each ν' level and subsequent summation over ν' of the vibrational emission cross sections gives the electronic emission cross section of the $C\ ^3\Pi_u$ state, which represents the sum of the direct excitation and cascade cross sections. The only known cascading to the $C\ ^3\Pi_u$ state results from the optically forbidden transition $E\ ^3\Sigma_g^+ \rightarrow C\ ^3\Pi_u$ with a lifetime of 270 μs. This lifetime is long enough for the drift of metastable molecules far out of the instrument field of view (less than 1 cm). Finn et al. (1972) measured the relative emission cross sections for the (0,0) and (1,0) bands and found some features just above the threshold region in the (0,0) emission which they attributed to the contribution from collisional quenching of the $E\ ^3\Sigma_g^+$ state. However, they stated that the $E\ ^3\Sigma_g^+$ contribution was insignificant in determining the total emission for 2PB. On the basis of the available literature, the total emission cross sections can be compared to electron scattering excitation cross sections, since the cascade cross section for *E*–*C* (200–400 nm) was unobserved due to a very weak transition (see Gilmore et al. 1992) in a steady-state experiment (Shemansky et al. 1995). The recent vibrationally resolved excitation cross sections (Malone et al. 2009) and non-vibrationally resolved excitation cross sections from earlier electron scattering experiments (near 25 eV) are also shown in Table 4, for comparison to the results obtained here for the total vibrational emission cross sections for $\nu' = 0$–3 and the total electronic emission cross section. The vibrationally resolved excitation cross sections of Malone et al. (2009) given in Table 4 appear to be systematically lower than the results found here. The general agreement is within 20%, indicating that cascade is unimportant in a steady-state emission experiment. Comparing the published values in Table 4, we find excellent agreement (<15%) with Cartwright et al. (1977), who measured an excitation cross section of 11.8×10^{-18} cm^2 at 24 eV, and Shemansky et al. (1995), who measured an emission cross section of 10.5×10^{-18} cm^2 at 25 eV. Our measured values at 25 eV and 100 eV were 10.87×10^{-18} cm^2 and 0.859×10^{-18} cm^2, respectively. Our ratio falloff for the 25 eV and 100 eV cross sections is 12.65, which indicates an insignificant effect of secondary electrons for the weaker bands. The present results are consistent with our earlier data of Shemansky et al. (1995), in which only the 2PB band system was measured, in terms of absolute values and cross-sectional ratios between 25 eV and 100 eV.

3.2 First Negative Band System $B\ ^2\Sigma_u^+(v') \rightarrow X\ ^2\Sigma_g^+(v'')$ of N_2^+

Figures 4–9 show high-resolution spectra of the 1NB system of N_2^+ ($B\ ^2\Sigma_u^+(v') \rightarrow X\ ^2\Sigma_g^+(v'')$) emissions, in smaller wavelength windows than shown in Figures 3(a) and (b), for identifying the details of the vibrational–rotational structure of various bands (ν',ν''). We have observed 20 emission bands from various vibrational levels with $\Delta v = 0$ through -3 in $B\ ^2\Sigma_u^+(\nu' = 0$–$3) \rightarrow X\ ^2\Sigma_g^+(v'' = 0$–$5)$. These emissions occur from an N_2^+ ion via simultaneous ionization and excitation of N_2 by electron impact. The strongest of all the band systems is the (0,0) band head emission at 391.443 nm of 1NB at both 25 eV and 100 eV electron-impact energies. The (0,0) band has been the most extensively studied emission from N_2^+ by an electron impact of N_2 in the laboratory by many researchers (see Table 5) and is commonly observed in the aurora by many spacecraft and ground-based observations. Based on the excitation function measurements reviewed in Borst & Zipf (1970), the emission intensities of $B\ ^2\Sigma_u^+(\nu') \rightarrow X\ ^2\Sigma_g^+(v'')$ system increase with electron-impact energy from threshold to near 100 eV. This trend is consistent with the increase of N_2^+ production cross section by electron impact on N_2, which peaks around 95 eV. Srivastava & Mirza (1968a) reported that the (0,0) band cross section as a function of electron-impact energy indicates that the $B\ ^2\Sigma_u^+$ state is excited at a constant fraction of the total ionization of N_2 and in agreement with the Bethe–Born approximation for ionization at higher electron-impact energies.

Table 10
Relative Emissions Cross Sections for the First Positive Band System $B\ ^3\Pi_g(\nu') \rightarrow A\ ^3\Sigma_u^+(\nu'')$ of N_2

Band (ν',ν'')	Present Data	Model[a]	Stanton & St. John (1969)	McConkey & Simpson (1969)
(0,0)	0.516	0.29	0.357	
(1,0)	1.307	1.307	0.877	
(2,0)	0.677	0.66	0.772	0.64
(2,1)	0.951	0.85	0.858	
(2,2)	0.184	0.158	0.178	
(3,0)	0.157	0.152	0.158	0.19
(3,1)	1.00	1.00	1.00	1.00
(3,2)	0.306	0.26	0.272	
(3,3)	0.375	0.312	0.351	
(4,0)	0.026	0.0156		
(4,1)	0.351	0.312	0.355	0.39
(4,2)	0.766	0.79	0.877	0.87
(4,3)	0.013	0.0135		
(4,4)	0.23	0.237		
(4,5)	0.0653	0.059		
(5,1)	0.047	0.0396	0.046	0.11
(5,2)	0.353	0.354	0.421	0.035
(5,3)	0.418	0.416	0.403	0.476
(6,2)	0.056	0.0562	0.077	0.052
(6,3)	0.298	0.291	0.408	0.428
(6,4)	0.238	0.163	0.235	0.224
(6,5)	0.0614	0.052		
(7,3)	0.0634	0.0573	0.082	0.057
(7,4)	0.219	0.187	0.267	0.288
(7,5)	0.0653	0.043	0.071	
(7,6)	0.076	0.053		
(8,4)	0.0545	0.0476	0.064	0.046
(8,5)	0.134	0.094	0.151	0.144
(9,5)	0.0434	0.0354	0.05	0.035
(9,6)	0.0766	0.052	0.0763	
(10,6)	0.026	0.022	0.034	0.025
(10,7)	0.022	0.02	0.035	
(11,7)	0.022	0.0135	0.027	0.017
(11,8)			0.0196	
(12,8)	0.0228	0.0135	0.022	
(13,9)	0.008	0.006		

Note. [a] Model results are based on Frank–Condon factors and branching ratios of Gilmore et al. (1992).

Figure 8 shows high-resolution ($\Delta\lambda = 0.07$ nm) spectra of the $B\ ^2\Sigma_u^+(\nu') \rightarrow X\ ^2\Sigma_g^+(\nu'')$ transitions of the prominent 1NB band (0,2), with clear distinction between P and R branches (whose separation and intensity are more prominent at 100 eV), free of overlap of emissions from the 2PB and 1PB systems. Both the upper and lower states of the 1NB system are $\Sigma(\Lambda = 0)$, and thus they strictly belong to Hund's case (b), in which $J' = 0 \rightarrow J'' = 0$ transitions are always forbidden for electronic systems in which both states have zero angular momentum along the internuclear axis. Hence, the Q branch ($\Delta J = 0$) is forbidden and not present in the 1NB system (Herzberg 1989). The vibrational transitions between $^2\Sigma_u^+$ and $^2\Sigma_g^+$ states follow the selection rule of $\Delta J = \pm 1$ leading to the formation of only P ($\Delta J = +1$) and R ($\Delta J = -1$) branches. Similar to the transitions in the 2PB ($C\ ^3\Pi_u(\nu') \rightarrow B\ ^3\Pi_g(\nu'')$) states of N_2 discussed in Section 3.1, the internuclear distance between upper state $B\ ^2\Sigma_u^+$ and lower state $X\ ^2\Sigma_g^+$ of N_2^+ of 1NB is such that $R_B < R_X$ (see Figure 1). Therefore, all the 1NB bands also exhibit sharp band heads forming in the P branch and a broader R branch. In the present high-resolution measurements, as shown in Figure 8, the R-branch rotational line intensity distribution shows a typical representation of the Fortrat parabola. The selection rule of $J'-J'' = \pm 1$ dictates that the transition in $^2\Sigma_u^+ - ^2\Sigma_g^+$ can only take place with rotational levels of equal nuclear spin degeneracy, which lead to that the even-numbered rotational energy levels of the N_2^+ ($B\ ^2\Sigma_u^+$) state can only combine with the odd-numbered rotational energy levels of the N_2^+ ($X\ ^2\Sigma_g^+$) state (Herzberg 1989). In other words, it is evident from the intensity alteration in the distribution of rotational levels observed in the R branch of $B\ ^2\Sigma_u^+ \rightarrow X\ ^2\Sigma_g^+$ bands that N_2 and N_2^+ being homonuclear that obey Bose statistics with an even:odd intensity alternation ratio of 2:1 exhibiting stronger *even* rotational levels due to the nuclear spin statistics of N_2 (see Figure 8). From the figure, the J values corresponding to 6 and 8 are stronger and their intensity distributions estimate N_2 gas temperature of ~300 K (Culp & Stair 1967; Hoppe 1970; Parigger et al. 1995; Linss 2005). It is

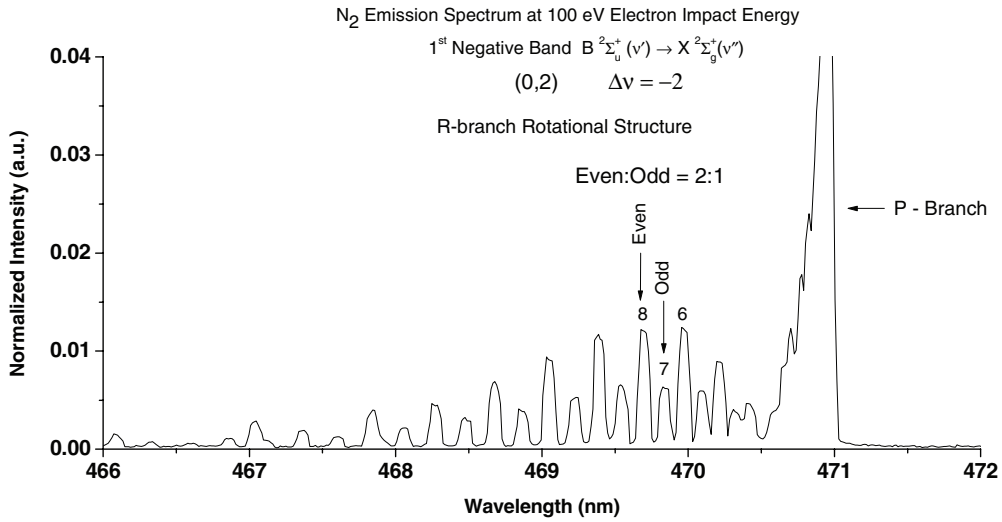

Figure 8. Expanded range of calibrated electron-impact-induced fluorescence spectrum of N_2 covering the (0,2) band of the first negative band system $B\,^2\Sigma_u^+(\nu') \rightarrow A\,^3\Sigma_g^+(\nu'')$ for electron energy of 100 eV, at a spectral resolution of 0.07 nm FWHM with a spectrometer resolving power of $\lambda/\Delta\lambda \approx 10000$, with detailed P-branch and R-branch rotational structures, corresponding to the N_2 gas temperature of ∼300 K for intense components of R branch with J values of 6 and 8.

Table 11
Total Emission Cross Section, $Q_{em}(\nu') = \Sigma Q_{em}(\nu',\nu'')$ (in Units of 10^{-18} cm^2), of the First Positive Band System of N_2 for Transitions from an Upper State $B\,^3\Pi_g(\nu')$ Vibrational–Rotational Level ν' into the Lower State $A\,^3\Sigma_u^+(\nu'')$

(ν')	Present Cross Sections at 25 eV 100 eV	Model[a]	Stanton & St. John (1969)
0	3.50	2.450	0.944
	0.455	0.319	...
1	8.87	8.87	2.32
	1.15	1.15	...
2	12.31	14.19	4.792
	1.614	1.848	
3	11.60	14.74	4.744
	1.704	1.92	...
4	9.873	12.185	3.27
	1.291	1.593	...
5	5.56	6.977	2.54
	0.755	0.909	...
6	4.435	4.807	1.908
	0.607	0.627	...
7	2.881	2.91	1.117
	0.395	0.379	...
8	1.287	1.281	0.575
	0.069	0.0644	...
9	0.815	0.738	0.335
	0.1084	0.1093	...
10	0.329	0.366	0.20
	0.042	0.0477	...
11	0.151	0.274	0.125
	0.02	0.038	...
12	0.155	0.202	0.06
	0.096	0.026	...
13	0.0527	0.212	...
	0.007	0.026	...

Notes. A comparison is made with others' data. In each row the top values represent $Q_{em}(\nu')$ at 25 eV and the bottom values represent at 100 eV electron-impact energy.
[a] Model results are based on Frank–Condon factors and branching ratios of Gilmore et al. (1992).

Table 12
Comparison of Total Emission Cross Sections, $\Sigma Q_{em}(\nu')$, (in Units of 10^{-18} cm^2), for the First Positive Band System $B\,^3\Pi_g(\nu') \rightarrow A\,^3\Sigma_u^+(\nu'')$ of N_2 with Electron Excitation Cross Sections $Q_{ex}(B\,^3\Pi_g)$ at Electron-impact Energies Listed Below

Electron-impact Energy (eV)	Present	Model	Stanton & St. John (1969)	McConkey & Simpson (1969)
25	61.819	69.514	37.0	33.0
100	8.313	8.967		

also clear from Figures 5–9 that the wavelength separation for rotational lines of the R branch of the 1NB bands increases with increase in lower state vibrational level (ν'') for the same upper vibrational level ν' (i.e., ν' = constant, ν''-progression).

At low pressures (e.g., 5×10^{-5} Torr in the present experimental conditions), spontaneous emission takes place rapidly (lifetime of a few ns) between the $B\,^2\Sigma_u^+$ and $X\,^2\Sigma_g^+$ states, before thermalization of the rotational levels of the excited $N_2{}^{+*}$ can occur. In other words, collisional equilibrium maintains the ground-state rotational population of $\nu'' = 0$ at near 300 K. Following electron excitation, the ground-state $\nu'' = 0$ rotational population is reflected in the excited state $B\,^2\Sigma_u^+$ of N_2^+. The rotational levels of the ground state, N_2 ($X\,^1\Sigma_g^+$) at room temperature populate only $\nu'' = 0$ with a distribution determined by a product of a rotational–vibrational Maxwell–Boltzmann energy distribution, with statistical weights based upon the $2J+1$ levels and nuclear statistics (Jokiaho et al. 2008 and references therein). Therefore, the rotational temperature (T_r) of the radiating state $B\,^2\Sigma_u^+$ of N_2^+ reflects the neutral gas N_2 ($X\,^1\Sigma_g^+$) temperature (i.e., $T_r \propto T_n$), and T_n can thus be determined from the structure and relative intensities of R-branch rotational emissions. In the present measurements from Figure 8, $J = 6$ is found to be $J_{max,}$ giving a neutral gas temperature of ∼300 K. This method is also commonly used with nitrogen emission bands in determining the temperature of neutrals in the upper atmosphere (Jokiaho et al. 2008) and in low-pressure plasma discharges (Nassar et al. 2004; Linss 2005; Huang et al. 2008, and references therein) and laser-induced emissions (Parigger et al. 1995). Koehler et al. (1981) demonstrated the application of rotational temperatures of the (0,2) band emission of 1NB system to auroral studies. Recently, Jokiaho et al. (2008) used the (0,2) band, obtained with a high-resolution ($\Delta\lambda$ =

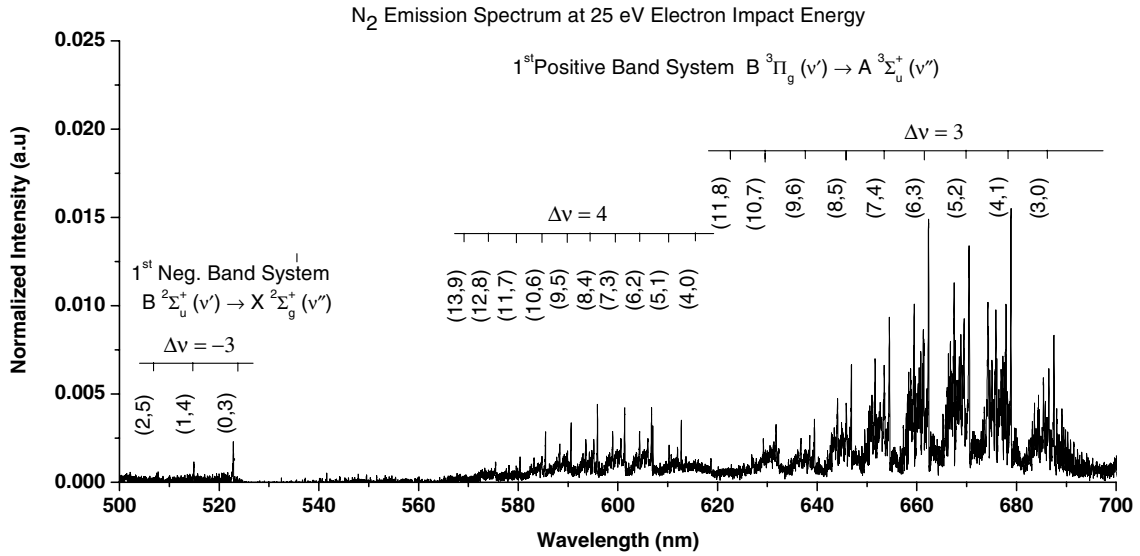

(a)

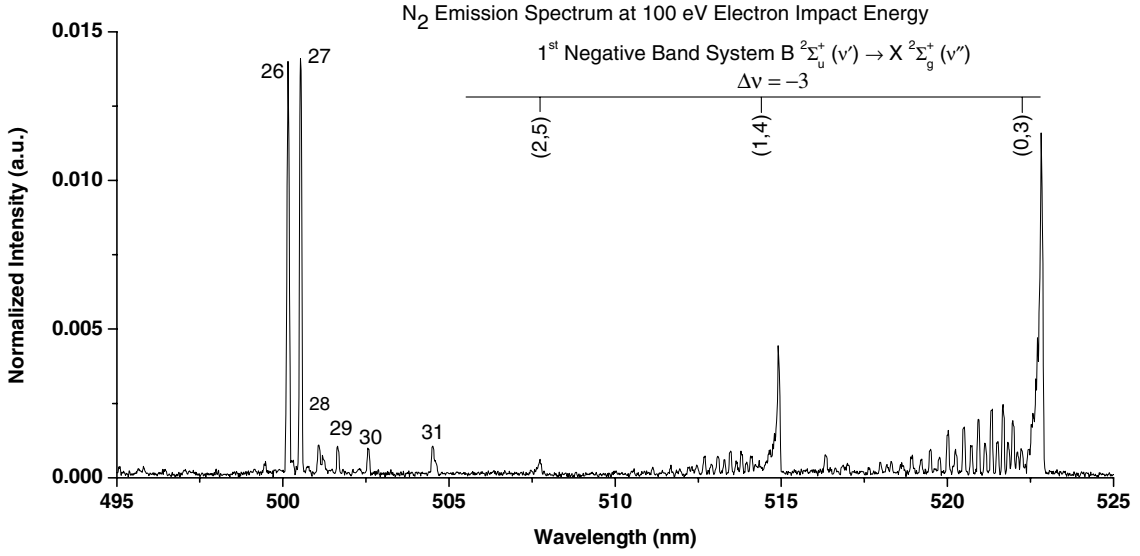

(b)

Figure 9. (a) Calibrated electron-impact-induced fluorescence spectrum of N_2 from 500 nm to 700 nm for electron energy of 25 eV identifying the vibrational bands and sequences of the first positive band system $B\,^3\Pi_g^+(\nu') \rightarrow A\,^3\Sigma_u^+(\nu'')$ and first negative band system $B\,^2\Sigma_u^+(\nu') \rightarrow A\,^3\Sigma_g^+(\nu'')$ at a spectral resolution of 0.07 nm FWHM with a spectrometer resolving power of $\lambda/\Delta\lambda \approx 10000$. (b) Calibrated electron-impact-induced fluorescence spectrum of N_2 from 495 nm to 700 nm for electron energy of 100 eV identifying the vibrational bands and sequences of the first negative band system $B\,^2\Sigma_u^+(\nu') \rightarrow A\,^3\Sigma_g^+(\nu'')$ at a spectral resolution of 0.07 nm FWHM with a spectrometer resolving power of $\lambda/\Delta\lambda \approx 10000$. Strong emissions of N II multiplets are also identified as listed in Table 18.

Table 13
Comparison of Cross Sections (in Units of 10^{-18} cm^2) for Electronic Excitation of the States Reported in the Literature

Electronic State at Electron impact Energy (eV)	Cartwright et al. (1977)	Campbell et al. (2001)	Malone et al. (2009)	Johnson et al. (2005)
$Q(B)$ at 25 eV	13.0	12.0	8.410	12.00
$Q(B')$ at 25 eV	4.00	8.00		4.200
$Q(C)$ at 25 eV	10.0	13.0		8.400
$Q(E)$ at 25 eV	0.8	1.40	0.107	0.107
$Q(W)$	13.0	8.0		
Total	40.8	42.4		24.70

0.08 nm), which is similar to ours (0.07 nm), to estimate the neutral temperatures and emission height variations at auroral heights recorded with the High Throughput Imaging Echelle Spectrograph. Using the ionization rate profiles obtained from the rotational temperature of the (0,2) band and the total energy flux from the intensity of the band, they have derived the

Table 14
Emission Cross Sections, $Q_{em}(\nu',\nu'')$ (in Units of 10^{-18} cm^2), for the Meinel Band System $A\ ^2\Pi_u\ (\nu') \rightarrow X\ ^2\Sigma_g^+(\nu'')$ of N_2^+ along with Our Model[a] and Previously Published Data

Band (ν',ν'') λ (nm)	Band Head Wavelength 25 eV 100 eV	Present Cross Sections at	Model[a]	Stanton & St. John (1969)	Simpson & McConkey (1969)	Srivastava & Mirza (1968b, 1968c)	Mandelbaum & Feldman (1976)	Skubenich & Zapesochny (1981)	Piper et al. (1986)
(0,0)	1109.20	2.63[a]	2.63						
		6.710[a]	6.710						
(1,0)	914.569								
	919.010	3.32	3.32	...	...	...	...	...	...
	921.279	8.46	8.46	...	...	...	2.78 Rel	...	...
(2,0)	782.850								
	785.974	3.176	1.364	...	...	...	...	...	..
	787.478	6.64	3.480	4.5 ± 0.2	2.10	6.02	1.0 Rel	5.70	10.1 ± 1.4
(2,1)	943.102								
	947.034	1.68	1.256	...	...	...	...	...	...
	950.246	3.73	3.199	...	...	...	1.20 Rel	...	...
(3,0)	685.384								
	688.052	0.385	0.321	...	...	...	...	...	...
	689.102	1.04	0.817	1.22 ± 0.2	0.65	...	...	...	...
(3,1)	805.535								
	809.100	1.02	0.849	...	...	...	...	...	..
	810.692	2.48	2.164	2.9 ± 0.2	...	2.40	0.64 Rel	3.80	7.0 ± 1.0
(3,2)	973.334								
	977.260	0.392[a]	0.190	...	...	...	...	...	...
	980.974	0.399	0.485	...	...	...	0.64 Rel	...	...
(4,0)	610.742								
	612.917	0.089[a]	0.056	...	...	...	...	...	...
	613.663	0.228	0.142	0.24	0.14 ± 0.6	...	...	...	...
(4,1)	704.339								
	707.171	0.38	0.275	...	...	...	...	...	...
	708.259	0.90	0.701	1.03	0.60 ± 0.1	0.68	...	1.30	2.2 ± 0.3
(4,2)	829.557								
	833.377	0.42	0.277	...	...	...	...	...	...
	835.032	0.966	0.706	...	...	...	...	...	...
(5,1)	626.877								
	629.229	0.108[a]	0.060	...	...	...	...	...	...
	629.975	0.277	0.152	...	...	...	...	...	...
(5,2)	724.090								
	727.112	0.225[a]	0.126	...	...	...	...	...	...
	728.250	0.573	0.322	0.59	0.13	...	...	...	...

Notes. In each (ν',ν'') row, the top values represent $Q_{em}(\nu',\nu'')$ at 25 eV and the bottom values represent at 100 eV electron-impact energy.
[a] Model results are based on Frank–Condon factors and branching ratios of Gilmore et al. (1992).

Table 15
Relative Emission Cross Sections of the Meinel Band System $A\ ^2\Pi_u \rightarrow X\ ^2\Sigma_g^+$ of N_2^+

Band (v',v'')	Present	Model	Stanton & St. John (1969)	Simpson & McConkey (1969)	Srivastava & Mirza (1968b, 1968c)	Mandelbaum & Feldman (1976)	Skubenich & Zapesochny (1981)	Piper et al. (1986)
(0,0)	1.01	1.01	...	...	...	...	...	...
(1,0)	1.274	1.274	...	...	...	2.78	...	...
(2,0)	1.00	1.00	1.00	1.00	1.00	1.00	1.00	1.00
(2,1)	0.56	0.482	...	...	...	1.20	...	...
(3,0)	0.157	0.123	0.265	0.31	...	...	...	...
(3,1)	0.373	0.326	0.63	...	0.40	0.64	0.67	0.69
(3,2)	0.06	0.073	...	...	...	0.64	...	...
(4,0)	0.0344	0.022	0.052	0.067	...	...	...	...
(4,1)	0.136	0.106	0.224	0.286	0.113	...	0.228	0.218
(4,2)	0.145	0.107	...	...	...	...	...	...
(5,1)	0.042	0.023	...	...	...	...	...	...
(5,2)	0.086	0.0485	0.128	0.062	...	...	...	...

Table 16
Total Emission Cross Section, $Q_{em}(v')$ (in Units of 10^{-18} cm^2) of the Meinel Band System of N_2^+ for Transitions from an Upper State $A\ ^2\Pi_u$ Vibrational–Rotational Level v' into the Lower State $X\ ^2\Sigma_g^+$

(v')	Present Cross Sections at 25 eV 100 eV	Model[a]	Stanton & St. John (1969)	Simpson & McConkey (1969)	Srivastava & Mirza (1968b, 1968c)	Skubenich & Zapesochny (1981)	Piper et al. (1986)
0	2.63[a]	2.63					
	6.710[a]	6.710					
1	3.32	3.32	...	...	...	...	...
	8.46	8.46	...	...	...	...	...
2	4.856	2.62	...	...	..	...	..
	10.37	6.679	4.5	2.10	6.02	5.70	10.1
3	1.02	1.36	...	...	...	...	...
	3.919	3.466	1.22	0.65	...	3.80	7.0
4	1.465	0.608	...	...	...	...	...
	2.094	1.549	1.27	0.84	0.68	...	2.2
5	0.333	0.186	...	...	...	...	...
	0.85	0.474	...	0.13	...	...	...

Notes. A comparison is made with previously published results. In each (v') row the top values represent $Q_{em}(v')$ at 25 eV and the bottom values represent at 100 eV electron-impact energy.
[a] Model results are based on Frank–Condon factors and branching ratios of Gilmore et al. (1992).

Table 17
Comparison of the Total Electronic Cross Section, $\Sigma Q_{em}(v' = 0\text{–}5)$, (in Units of 10^{-18} cm^2) of the Meinel Band System of N_2^+ at 25 eV and 100 eV Electron-impact Energies

Electron-impact Energy (eV)	Present	Model	Simpson & McConkey (1969)	Shemansky & Liu (2005)	Piper et al. (1986)
25	13.624	13.268		55.0	
100	32.403	27.338	26.5	82.64	115[a]

Note. [a] Piper data: these are electronic excitation values to the $A\ ^2\Pi_u$ state.

electron density height profiles. We intend to pursue the details of the rotational structure of each of these band systems in a later publication; this paper pertains mainly to the vibrational structure.

The present measured emission cross sections are listed in Table 5 in terms of vibrational transitions (v',v'') of the emission bands for the $B\ ^2\Sigma_u^+(v') \rightarrow X\ ^2\Sigma_g^+(v'')$ system along with the data available in the literature. Earlier reported emission cross sections for the (0,0) band at 391.4 nm as a function of electron-impact energy were from threshold to 300 eV by McConkey & Latimer (1965), who later revised their (0,0) value from threshold to 55 eV (McConkey et al. 1971); from 70–2500 eV by Srivastava & Mirza (1968a), who also revised their (0,0) value and reported additional (0,1) and (0,2) bands from 70–4000 eV (Srivastava & Mirza 1968b); from 80–1500 eV by Nishimura (1968); from 100–600 eV by Aarts et al. (1968) who later revised it (De Heer & Aarts 1970), 0–450 eV by Stanton & St. John (1969); from 500—20,000 eV by Koval et al. (1969); from threshold–3000 eV by Borst & Zipf (1970); and from 30–400 eV by Shaw & Campos (1983). Doering & Yang (1996) determined the (0,0) band cross section from measurements of branching ratios of $X\ ^2\Sigma_g^+$, $A\ ^2\Pi_u$, and $B\ ^2\Sigma_u^+$ (v'') in an electron–electron coincident technique and electron-impact-ionization cross sections of N_2^+. None of the above authors either published the emission spectra for any of the bands of $B\ ^2\Sigma_u^+(v') \rightarrow X\ ^2\Sigma_g^+(v'')$ system or used high spectral resolution in their measurements. There are

Table 18
Emission Cross Section, Q_{em} (in Units of 10^{-18} cm^2), for N I and N II Transitions Induced by Electron Impact at N_2 for Energies of 25 eV and 100 eV

Peak Number	Species	Multiplet	Wavelength λ (nm)	Cross Section at 25 eV 100 eV
1	N II	$2s^2 2p(^2P^\circ)3s–2s^2 2p(^2P^\circ)3p \;\; ^3P^\circ–^1D$	395.641	0.033
2	N II	$2s^2 2p(^2P^\circ)3s–2s^2 2p(^2P^\circ)3p \;\; ^1P^\circ–^1D$	399.501	0.059
3	N I	$2s^2 2p^2(^3P)3s–2s^2 2p^2(^3P)5p \;\; ^2P–^2S^\circ$	401.180	0.0124
4	N I	$2s^2 2p^2(^3P)3s–2s^2 2p^2(^3P)5p \;\; ^2P–^2S^\circ$	402.451	0.016
5	N II	?	403.595	0.019
6	N II	?	404.214	0.023
7	N II	?	404.391	0.012
8	N I	$2s^2 2p^2(^3P)3s–2s^2 2p^2(^1D)3p \;\; ^2P–^2D^\circ$	410.069	0.010
9	N I	$2s^2 2p^2(^3P)3s–2s^2 2p^2(^1D)3p \;\; ^2P–^2D^\circ$	411.043	0.016
10	N II	$2s2p^2(^4P)3s–2s2p^2(^4P)3p \;\; ^5P–^5S^\circ$	412.939	0.005
11	N I	$2s^2 2p^2(^3P)3s–2s^2 2p^2(^3P)4p \;\; ^4P–^4S^\circ$	414.381	0.0084
12	N I	$2s^2 2p^2(^3P)3s–2s^2 2p^2(^3P)4p \;\; ^4P–^4S^\circ$	415.190	0.0114
13	N II	?	417.605	0.014
14	N II	?	424.181	0.05
15	N II	?	443.236	0.012
16	N II	?	453.112	0.0175
17	N III	$2s^2 4d–2s2p(^3P^\circ)3d \;\; ^2D–^2F^\circ$	455.337	0.017
18	N II	$2s^2 2p(^2P^\circ)3s–2s^2 2p(^2P^\circ)3p \;\; ^3P^\circ–^3P$	460.206	0.0142
19	N II	$2s^2 2p(^2P^\circ)3s–2s^2 2p(^2P^\circ)3p \;\; ^3P^\circ–^3P$	460.749	0.011
20	N II	$2s^2 2p(^2P^\circ)3s–2s^2 2p(^2P^\circ)3p \;\; ^3P^\circ–^3P$	462.153	0.012
21	N II	$2s^2 2p(^2P^\circ)3s–2s^2 2p(^2P^\circ)3p \;\; ^3P^\circ–^3P$	463.076	0.035
22	N II	$2s2p^2(^4P)3p–2s2p^2(^4P)3d \;\; ^5D^\circ–^5P$	484.951	0.005
23	N II	$2s2p^3–2s^2 2p(^2P^\circ)3p \;\; ^1D^\circ–^1P$	489.579	0.011
24	N I	$2s^2 2p^2(^3P)3s–2s^2 2p^2(^3P)4p \;\; ^2P–^2S^\circ$	491.539	0.019
25	N I	$2s^2 2p^2(^3P)3s–2s^2 2p^2(^3P)4p \;\; ^2P–^2S^\circ$	493.550	0.039
26	N II	$2s^2 2p(^2P^\circ)3p–2s^2 2p(^2P^\circ)3d \;\; ^3D–^3F^\circ$	500.151	0.0964
27	N II	$2s^2 2p(^2P^\circ)3p–2s^2 2p(^2P^\circ)3d \;\; ^3D–^3F^\circ$	500.530	0.0956 0.098*
28	N II	$2s^2 2p(^2P^\circ)3s–2s^2 2p(^2P^\circ)3p \;\; ^3P^\circ–^3S$	501.074	0.017
		$2s2p^2(^4P)3s–2s2p^2(^4P)3p^5P–^5P^\circ$	501.187	
29	N II	$2s^2 2p(^2P^\circ)3p–2s^2 2p(^2P^\circ)3d \;\; ^3D–^3F^\circ$	501.643	0.00821
30	N II	$2s^2 2p(^2P^\circ)3p–2s^2 2p(^2P^\circ)3d \;\; ^3D–^3F^\circ$	502.553	0.00835
31	N II	$2s^2 2p(^2P^\circ)3s–2s^2 2p(^2P^\circ)3p \;\; ^3P^\circ–^3S$	504.500	0.0131
32	N I	$2s2p^4–2s^2 2p^2(^3P)4p \;\; ^4P–^4P^\circ$	528.159	0.0085
33	N I	?	529.30	0.0061
34	N I	$2s2p^4–2s^2 2p^2(^3P)4p \;\; ^4P–^4D^\circ$	532.901	0.014
35	N I	$2s2p^4–2s^2 2p^2(^3P)4p \;\; ^4P–^4D^\circ$	535.682	0.010
36	N I	$2s2p^4–2s^2 2p^2(^3P)4p \;\; ^4P–^4D^\circ$	537.276	0.008
37	N II	$2s2p^2(^4P)3s–2s2p^2(^4P)3p \;\; ^5P–^5D^\circ$	553.613	0.0124
38	N I	$2s^2 2p^2(^3P)3p–2s^2 2p^2(^3P)5d \;\; ^4D^\circ–^4F$	556.078	0.0133
39	N I	$2s^2 2p^2(^3P)3p–2s^2 2p^2(^3P)5d \;\; ^4D^\circ–^4F$	556.508	0.0109
40	N II	$2s^2 2p(^2P^\circ)3s–2s^2 2p(^2P^\circ)3p \;\; ^3P^\circ–^3D$	566.713	0.0662
41	N II	$2s^2 2p(^2P^\circ)3s–2s^2 2p(^2P^\circ)3p \;\; ^3P^\circ–^3D$	567.636	0.0334
42	N II	$2s^2 2p(^2P^\circ)3s–2s^2 2p(^2P^\circ)3p \;\; ^3P^\circ–^3D$	568.002	0.147
43	N II	$2s^2 2p(^2P^\circ)3s–2s^2 2p(^2P^\circ)3p \;\; ^3P^\circ–^3D$	568.660	0.0226
44	N II	$2s^2 2p(^2P^\circ)3s–2s^2 2p(^2P^\circ)3p \;\; ^3P^\circ–^3D$	571.100	0.0256
45	N II	$2s^2 2p(^2P^\circ)3s–2s^2 2p(^2P^\circ)3p \;\; ^1P^\circ–^3D$	574.742	0.0121
46	N II	$2s^2 2p^2(^3P)3p–2s^2 2p^2(^3P)4d \;\; ^2S^\circ–^2P$	599.981	0.010
47	N I	$2s^2 2p^2(^3P)3p–2s^2 2p^2(^3P)4d \;\; ^2S^\circ–^2P$	600.879	0.010
48	N II	$2s^2 2p(^2P^\circ)3d–2s^2 2p(^2P^\circ)4p \;\; ^3F^\circ–^3D$	616.786	0.015
49	N II	$2s^2 2p(^2P^\circ)3d–2s^2 2p(^2P^\circ)4p \;\; ^3F^\circ–^3D$	617.014	0.008
50	N II	$2s^2 2p(^2P^\circ)3d–2s^2 2p(^2P^\circ)4p \;\; ^3F^\circ–^3D$	617.355	0.0114
51	N II	$2s^2 2p(^2P^\circ)3d–2s^2 2p(^2P^\circ)4p \;\; ^1F^\circ–^1D$	624.297	0.014

Table 18
(Continued)

Peak Number	Species	Multiplet	Wavelength λ (nm)	Cross Section at 25 eV 100 eV
52	N II	$2s^22p(^2P^\circ)3s–2s^22p(^2P^\circ)3p \quad ^3P^\circ–^1P$	638.017	0.02
53	N I	$2s^22p^2(^3P)3p–2s^22p^2(^3P)4d \quad ^4D^\circ–^4D$	641.229	0.0068
54	N I	?	643.715	0.010
	N I	$2s^22p^2(^3P)3p–2s^22p^2(^3P)4d \quad ^4D^\circ–^4F$	648.170	
55	N II	$2s^22p3s–2s^22p3p \quad ^1P^\circ–^1P$	648.246	0.192
	N I	$2s^22p^2(^3P)3p–2s^22p^2(^3P)4d \quad ^4D^\circ–^4F$	648.270	
56	N I	$2s^22p^2(^3P)3p–2s^22p^2(^3P)4d \quad ^4D^\circ–^4F$	648.398	0.050
57	N I	$2s^22p^2(^3P)3p–2s^22p^2(^3P)4d \quad ^4D^\circ–^4F$	648.512	0.072
58	N I	$2s^22p^2(^3P)3p–2s^22p^2(^3P)4d \quad ^4P^\circ–^4D$	672.347	0.0254
59	N II	$2s^22p4s–2s2p^2(^4P)3s \quad ^1P^\circ–^3P$	717.767	0.0242
60	N II	$2s^22p(^2P^\circ)3d–2s^22p(^2P^\circ)4p \quad ^3P^\circ–^3D$	721.687	0.0212
61	N I	$2s^22p^2(^3P)3s–2s^22p^2(^3P)3p \quad ^4P–^4S^\circ$	742.438	0.054
62	N I	$2s^22p^2(^3P)3s–2s^22p^2(^3P)3p \quad ^4P–^4S^\circ$	744.296	0.12
63	N I	$2s^22p^2(^3P)3s–2s^22p^2(^3P)3p \quad ^4P–^4S^\circ$	746.876	0.175
64	N I	$2s^22p^2\ (^1D)3s–2s^22p^2(^3P)5p \quad ^2D–^2D^\circ$	816.623	0.082
65	N I	$2s^22p^2(^3P)3s–2s^22p^2(^3P)3p \quad ^4P–^4P^\circ$	818.421	0.0405[a] 0.255
66	N I	$2s^22p^2(^3P)3s–2s^22p^2(^3P)3p \quad ^4P–^4P^\circ$	818.739	0.033[a] 0.264
67	N I	$2s^22p^2(^3P)3s–2s^22p^2(^3P)3p \quad ^4P–^4P^\circ$	819.970	0.091
68	N I	$2s^22p^2(^3P)3s–2s^22p^2(^3P)3p \quad ^4P–^4P^\circ$	820.989	0.108
69	N I	$2s^22p^2(^3P)3s–2s^22p^2(^3P)3p \quad ^4P–^4P^\circ$	821.541	0.0824[a] 0.734
70	N I	$2s^22p^2(^3P)3s–2s^22p^2(^3P)3p \quad ^4P–^4P^\circ$	822.220	0.0322[a] 0.263
71	N I	$2s^22p^2(^3P)3s–2s^22p^2(^3P)3p \quad ^4P–^4P^\circ$	824.130	0.0336[a] 0.291
72	N I	$2s^22p^2(^3P)3s–2s^22p^2(^3P)3p \quad ^2P–^2P^\circ$	856.746	0.121
73	N I	$2s^22p^2(^3P)3s–2s^22p^2(^3P)3p \quad ^2P–^2P^\circ$	859.463	0.251
74	N I	$2s^22p^2(^3P)3s–2s^22p^2(^3P)3p \quad ^2P–^2P^\circ$	862.985	0.586
75	N I	$2s^22p^2(^1D)3s–2s^22p^2(^3P)5p \quad ^2D–^2P^\circ$	865.638	0.210
76	N I	$2s^22p^2(^1D)3s–2s^22p^2(^3P)5p \quad ^2D–^2P^\circ$	866.720	0.0533
77	N I	$2s^22p^2(^3P)3s–2s^22p^2(^3P)3p \quad ^4P–^4D^\circ$	868.078	1.64
78	N I	$2s^22p^2(^3P)3s–2s^22p^2(^3P)3p \quad ^4P–^4D^\circ$	868.375	0.921
79	N I	$2s^22p^2(^3P)3s–2s^22p^2(^3P)3p \quad ^4P–^4D^\circ$	868.651	0.479
80	N I	$2s^22p^2(^3P)3s–2s^22p^2(^3P)3p \quad ^4P–^4D^\circ$	870.370	0.477
81	N I	$2s^22p^2(^3P)3s–2s^22p^2(^3P)3p \quad ^4P–^4D^\circ$	871.198	0.503
82	N I	$2s^22p^2(^3P)3s–2s^22p^2(^3P)3p \quad ^4P–^4D^\circ$	871.919	0.376
83	N I	$2s^22p^2(^3P)3s–2s^22p^2(^3P)3p \quad ^4P–^4D^\circ$	872.917	0.0865
84	N I	$2s^22p^2(^3P)3s–2s^22p^2(^3P)3p \quad ^4P–^4D^\circ$	874.742	0.0425
85	N I	$2s^22p^2(^3P)3p–2s^22p^2(^3P)3d \quad ^2S^\circ–^2P$	902.860	0.0841
86	N I	$2s^22p^2(^1D)3s–2s^22p^2(^1D)3p \quad ^2D–^2F^\circ$	904.560	0.322
87	N I	$2s^22p^2(^1D)3s–2s^22p^2(^1D)3p \quad ^2D–^2F^\circ$	904.940	0.261
88	N I	$2s^22p^2(^3P)3p–2s^22p^2(^3P)3d \quad ^2S^\circ–^2P$	906.00	0.184
89	N I	$2s^22p^2(^3P)3s–2s^22p^2(^3P)3p \quad ^2P–^2D^\circ$	938.659	0.105[a] 0.60
90	N I	$2s^22p^2(^3P)3s–2s^22p^2(^3P)3p \quad ^2P–^2D^\circ$	939.275	0.169[a] 1.07
91	N I	$2s^22p^2(^3P)3p–2s^22p^2(^3P)3d \quad ^4D^\circ–^4D$	982.311	0.0754
92	N I	$2s^22p^2(^3P)3p–2s^22p^2(^3P)3d \quad ^4D^\circ–^4D$	986.322	0.173

Table 18
(Continued)

Peak Number	Species	Multiplet	Wavelength λ (nm)	Cross Section at 25 eV 100 eV
93	N I	$2s^22p^2(^3P)3p–2s^22p^2(^3P)3d\ \ ^4D^\circ–^4F$	1010.53	
94	N I	$2s^22p^2(^3P)3p–2s^22p^2(^3P)3d\ \ ^4D^\circ–^4F$	1010.90	0.334[a]
95	N I	$2s^22p^2(^3P)3p–2s^22p^2(^3P)3d\ \ ^4D^\circ–^4F$	1011.26	1.82
96	N I	$2s^22p^2(^3P)3p–2s^22p^2(^3P)3d\ \ ^4D^\circ–^4F$	1011.45	
97	N I	$2s^22p^2(^3P)3p–2s^22p^2(^3P)3d\ \ ^4D^\circ–^4F$	1012.83	0.042
98	N I	$2s^22p^2(^3P)3p–2s^22p^2(^3P)3d\ \ ^4D^\circ–^4F$	1014.69	0.055
99	N I	$2s^22p^2(^3P)3p–2s^22p^2(^3P)3d\ \ ^4D^\circ–^4F$	1016.48	0.045
100	N I	$2s^22p^2(^3P)3p–2s^22p^2(^3P)3d\ \ ^4P^\circ–^4D$	1054.02	0.22

Notes. A comparison is made with the previously published results. In each row, the top values represent cross sections at 25 eV and the bottom values represent at 100 eV electron-impact energy. Total cross section for N I and N II emissions in the present VOIR range at 25 eV = 0.83×10^{-18} cm^2. Total cross section for N I and N II emissions in the present VOIR range at 100 eV = 14.628×10^{-18} cm^2.

[a] Emission cross-sectional values at 25 eV electron-impact energy.

* Cross section reported by Aarts & De Heer (1971) for N II at 500.3 nm at 100 eV.

significant differences in both cross-sectional values and shapes of the excitation functions among their results. It is clear from Table 5 that there is a wide disagreement among the published cross-sectional values, except for the (0,0) band at 100 eV, which range from (15.0 to 17.4) $\times 10^{-18}$ cm^2 (with an exception of the value of 21.4×10^{-18} cm^2 of Aarts et al. 1968) for the 1NB emissions. The agreement for certain individual band emission cross sections is particularly good (15%) at both 25 eV and 100 eV for the $\nu' = 0$, ν''-progression. Besides inherent errors in various direct or indirect methods employed in determining the absolute cross sections, high values of electron-beam currents and gas pressures used in such measurements and the possible contamination of 1NB due to the overlap of the neighboring 1PB ($B\ ^3\Pi_g \rightarrow A\ ^3\Sigma_u^+$) and/or 2PB ($C\ ^3\Pi_u \rightarrow B\ ^3\Pi_g$) bands could potentially induce errors in the earlier reported cross-sectional values. We suspect the experimental techniques employed 40 years ago (Stanton & St. John 1969; McConkey & Simpson 1969) were performed with an insufficient bandpass to isolate the broad 10–20 nm wide rotational envelope of each band. Until now, the Borst & Zipf (1970) excitation function for the (0,0) band had been considered as a standard for much auroral and laboratory plasma modeling. They reported cross sections for only the (0,0) band as a function of electron-impact energy from emission threshold to 3 keV at an N_2 pressure of 1×10^{-4} Torr. Their data showed a cross-sectional maximum of $(17.4 \pm 0.17) \times 10^{-18}$ cm^2 at about 100 eV and at higher energies 200–3000 eV it falls off according to Bethe–Oppenheimer relation $Q_{\rm em} = {E_e}^{-1} A \ln(BE_e)$, where the constants A and B were determined from their data points. By using the shape of the Borst & Zipf (1970) emission cross section and published experimental-integrated electric dipole photoionization oscillator strengths (f_{ij}), Shemansky & Liu (2005) calculated the (0,0) band cross section at 100 eV to be $(14.7 \pm 1.2) \times 10^{-18}$ cm^2. In addition, they reported an average of 11 independent laboratory measurements for the (0,0) band to be 15.3×10^{-18} cm^2. The present (0,0) band cross section of 14.9×10^{-18} cm^2 at 100 eV is in excellent agreement with the value of 15.0×10^{-18} cm^2 reported by McConkey & Simpson (1969) and very close to the average value of 15.3×10^{-18} cm^2 (Shemansky & Liu 2005). We neglected the contribution of polarization to the present data, considering that it was previously examined for the (0,0) band emission at the magic angle 54°44′ and at 90°, and was reported to be less than 6%, 3%, 2%, 5%, and 5%, respectively, by McConkey & Latimer (1965), Aarts et al. (1968), Srivastava & Mirza (1968a, 1968b), Borst & Zipf (1970), and Shaw & Campos (1983). Among the data shown in Table 5, although the absolute values among the data are poor, the relative values are fairly in good agreement, as shown in Table 6.

We have modeled the prominent bands of the 1NB system, inserting model emission cross sections for overlapped bands and weak bands (mostly for the $\nu' = 2$, ν''-progression), based on transition probabilities provided in the review by Laher & Gilmore (1999). For each ν'-progression, we have chosen the strongest unblended band for normalization of all emission cross sections using Equation (11), for example, the (0,0) band at 391.44 nm for $\nu' = 0$, the (1,2) band at 423.65 for $\nu' = 1$, and the (2, 3) band at 419.97 nm for $\nu' = 2$. We find that the total ν'-vibrational emission cross section at 100 eV closely follow Franck–Condon factors with the excitation of $\nu' = 0$ representing ∼88% of the electronic emission cross section (Table 7). The total electronic emission cross section at 100 eV is found to be 25.32×10^{-18} cm^2, as compared to a value of 23.21×10^{-18} cm^2 (Table 8) based on photoionization electric dipole oscillator strengths (Shemansky & Liu 2005). Significant departure from Franck–Condon excitation is found for the vibrational bands in the 25 eV spectra (e.g., $\nu' = 2$). Lofthus & Krupenie (1977) report significant rotational-vibrational perturbations of the upper state $B\ ^2\Sigma_u^+$, and there have been observed numerous rotational line displacements and intensity anomalies arising from perturbations of the upper state. The perturbed levels of the B state are found for $\nu' = 0, 1, 3, 5, 9$, and 13, the perturbing state is $A\ ^2\Pi_u$. We note that the (2,3) band at 419.97 nm is overlapped by the 2PB (2,6) band. Thus, the band shape (rotational envelope) changes as the observed feature in Figure 6(a) at 25 eV is mostly 2PB, while in Figure 6(b) at 100 eV it is mostly 1NB (2,3).

3.3. First Positive System $B\ ^3\Pi_g(\nu') \rightarrow A\ ^3\Sigma_u^+(\nu'')$ of N_2

Figures 9(a), 10–14, 16, 18, and 19 show the details of emission spectra of the 1PB system $B\ ^3\Pi_g^+(\nu') \rightarrow A\ ^3\Sigma_u^+(\nu'')$ of N_2. We have observed several bands corresponding to the emissions from different vibrational levels ν' of the $B\ ^3\Pi_g$ state to ν'' of the $A\ ^3\Sigma_u^+$ state in the visible and near-infrared (IR) region from 560 to 1100 nm at both 25 and 100 eV

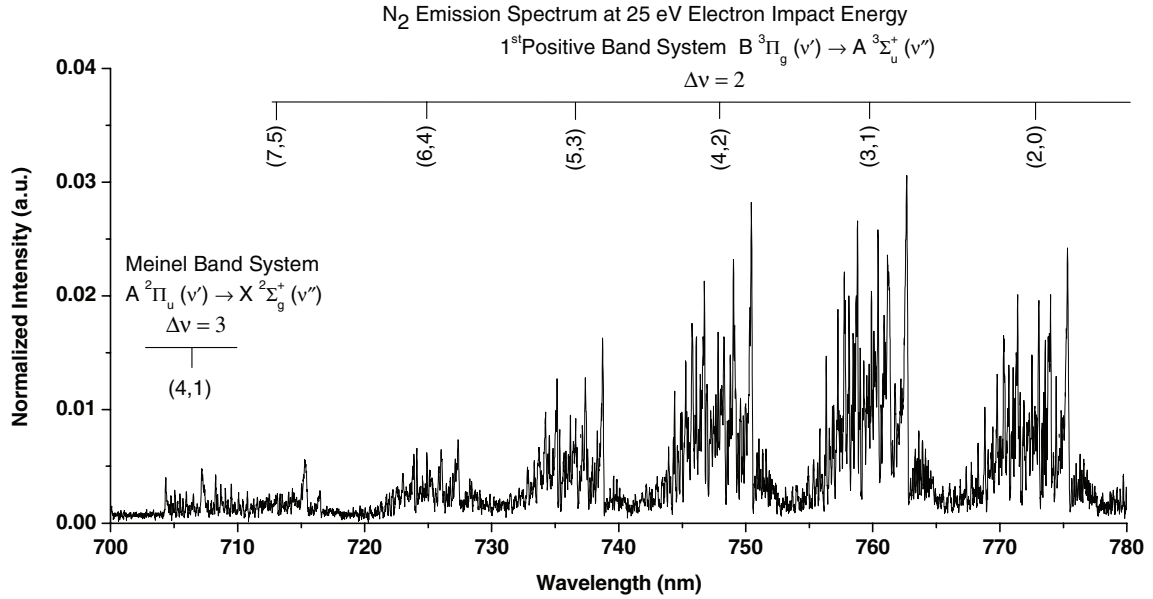

Figure 10. Calibrated electron-impact-induced fluorescence spectrum of N_2 from 700 nm to 780 nm for electron energy of 25 eV identifying the vibrational bands and sequences of the first positive system $B\,^3\Pi_g^+(v') \rightarrow A\,^3\Sigma_u^+(v'')$ and Meinel band system $A\,^2\Pi_u(v') \rightarrow X\,^2\Sigma_g^+(v'')$ at a spectral resolution of 0.07 nm FWHM with a spectrometer resolving power of $\lambda/\Delta\lambda \approx 10000$.

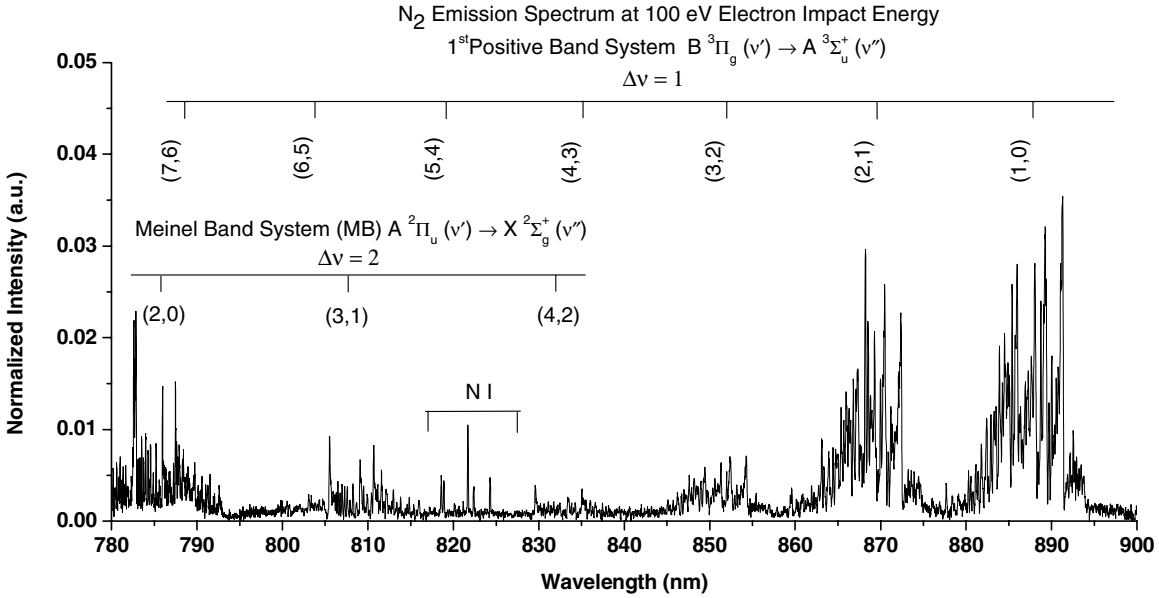

Figure 11. Calibrated electron-impact-induced fluorescence spectrum of N_2 from 780 nm to 900 nm for electron energy of 25 eV identifying the vibrational bands and sequences of the first positive band system $B\,^3\Pi_g^+(v') \rightarrow A\,^3\Sigma_u^+(v'')$ and Meinel band system $A\,^2\Pi_u(v') \rightarrow X\,^2\Sigma_g^+(v'')$ at a spectral resolution of 0.07 nm FWHM with a spectrometer resolving power of $\lambda/\Delta\lambda \approx 10000$. Strong N I atomic emissions are also identified as listed in Table 18.

electron-impact energies. A few of the 1PB system emissions are known to occur beyond our present wavelength limit of 1100 nm (Lofthus & Krupenie 1977). To the best of our knowledge, our results for the $\Delta v = 0$, 1, 2, 3, and 4 vibrational sequences are the first high-resolution spectra measurements for this part of the band system obtained under a single-scattering and optically thin conditions. The only electron-impact emissions of the 1PB system measured in the past (40 years ago), at lower spectral resolution, were by Stanton & St. John (1969) and McConkey & Simpson (1969). In the present wavelength range, the 1PB system has the highest number of emission bands (v',v'') with $\Delta v = 0$–4 sequences as compared to the other nitrogen emission bands investigated here (2PB, 1NB, MB systems). Similar to the electronic excitation $^1\Sigma_g^+ \rightarrow {}^3\Pi_u$ and emission $^3\Pi_u \rightarrow {}^3\Pi_g$ of the 2PB system, the 1PB is also excited through a forbidden singlet-triplet excitation $^1\Sigma_g^+ \rightarrow {}^3\Pi_g$ by low-energy electrons via electron exchange. Emission occurs between optically allowed triplet states $^3\Pi_g \rightarrow {}^3\Sigma_u^+$, whose cross-sectional maximum is at about twice the emission threshold (Stanton & St. John 1969; McConkey & Simpson 1969). A typical 1PB spectrum of the strongest $B \rightarrow A$ band (1,0) at 891.31 nm, shown in Figure 14, has clear multiple band heads degraded from red to blue wavelengths. As the upper state $B\,^3\Pi_g$ follows both Hund's cases (a) and (b) (for higher J') and the lower state $A\,^3\Sigma_u^+$ follows Hund's case (b), each band (v',v'') appears complex having several sub-band heads stronger toward the

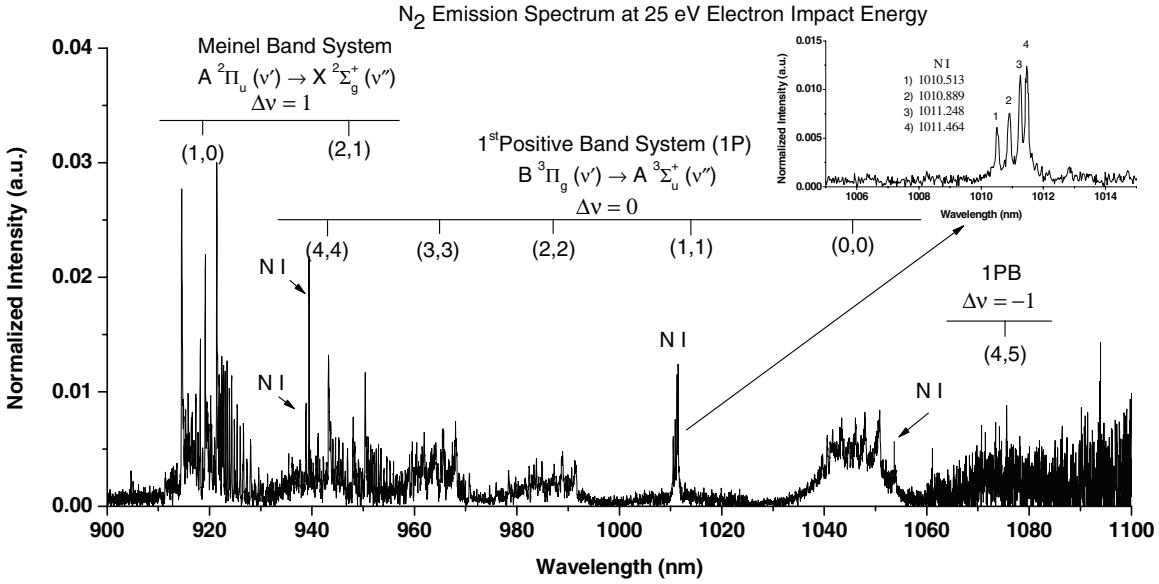

Figure 12. Calibrated electron-impact-induced fluorescence spectrum of N_2 from 900 nm to 1100 nm for electron energy of 25 eV identifying the vibrational bands and sequences of the first positive system $B\ ^3\Pi_g^+(\nu') \rightarrow A\ ^3\Sigma_u^+(\nu'')$ and Meinel band system $A\ ^2\Pi_u(\nu') \rightarrow X\ ^2\Sigma_g^+(\nu'')$ at a spectral resolution of 0.07 nm FWHM with a spectrometer resolving power of $\lambda/\Delta\lambda \approx 10000$. Strong N I atomic multiplets are also identified as listed in Table 18. The inset shows resolved N I $2s\ ^2 2p\ ^2(^3P)3p–2s\ ^2 2p\ ^2(^3P)3d\ (^4D^\circ–^4F)$ transition structure at 1011.2 nm.

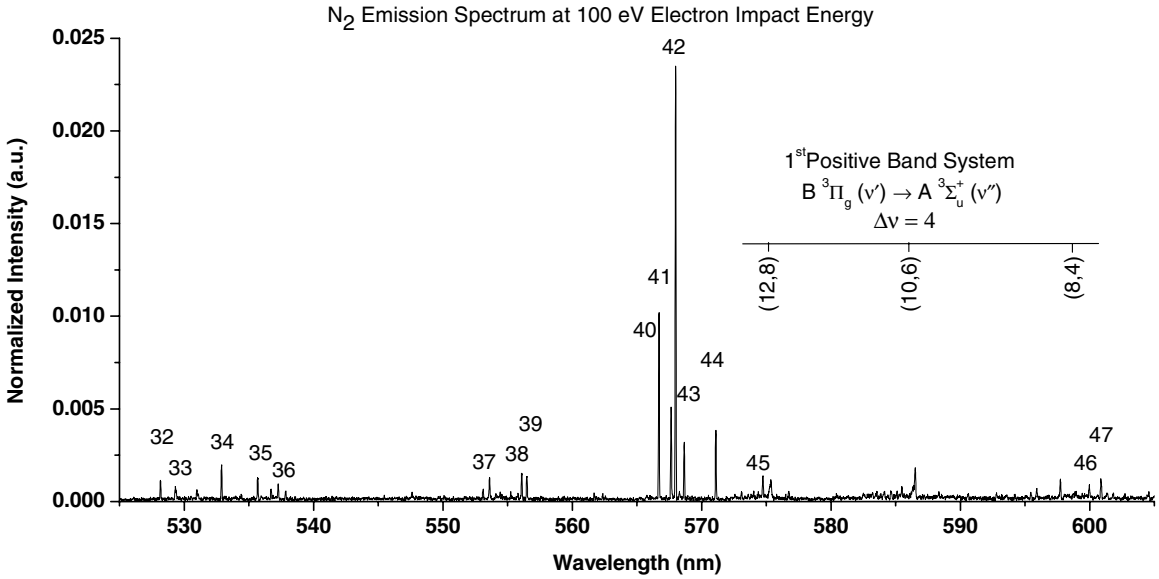

Figure 13. Calibrated electron-impact-induced fluorescence spectrum of N_2 from 525 nm to 610 nm for electron energy of 100 eV identifying the vibrational bands and sequences of the first positive band system $B\ ^3\Pi_g^+(\nu') \rightarrow A\ ^3\Sigma_u^+(\nu'')$ at a spectral resolution of 0.07 nm FWHM with a spectrometer resolving power of $\lambda/\Delta\lambda \approx 10000$. Strong N I and N II multiplets are also identified as listed in Table 18.

red while the rest descend toward the blue. Each band of the triplet transition $^3\Pi_g \rightarrow {}^3\Sigma_u^+$ is composed of P, Q, R branches corresponding to $\Delta J = -1,\ 0,\ +1$, respectively, and each vibronic transition is composed of 27 rotational branches of which 9 strong and 18 satellites correspond to P, Q, and R branches (Kryuchkov et al. 1984; Sakamoto et al. 2006; Biloiu et al. 2007). The complex structure of the 1PB system arises from the separation of the $B\ ^3\Pi_g$ state having three sub-bands $B\ ^3\Pi_0 \rightarrow A\ ^3\Sigma_u^+$, $B\ ^3\Pi_1 \rightarrow A\ ^3\Sigma_u^+$, and $B\ ^3\Pi_2 \rightarrow A\ ^3\Sigma_u^+$; each sub-band consisting of 9 transitions having $\Delta J = \Delta N$ (N is the quantum number of Hund's case (b)) are the strongest branches while the 18 other weak branches correspond to $\Delta J = \Delta N \pm 1$ and $\Delta N \pm 2$ and are called satellites (Sakamoto et al. 2006). Following the Fortrat parabola, the peaks in Figure 14 represent the turning points of the P_{11}, P_{22}, P_{33}, and R_{33} branches, respectively, as identified recently by Biloiu et al. (2007). Although the 1PB band system has a low emission threshold energy (e.g., 7.4 eV for $\nu' = 0$), a higher emission intensity, a higher predissociation level ($\nu'' = 12$) giving several emission bands, and longer radiative lifetimes ($\sim$7 μs; Hollstein et al. 1969), its complex rotational emission structure makes it much more difficult to use as a diagnostic spectroscopy for gas temperature measurements than the 2PB and 1NB systems.

When compared to other bands in the VOIR, the 1PB system of N_2 ($B\ ^3\Pi_g–A\ ^3\Sigma_u^+$) is the strongest, even stronger than the singlet Rydberg systems ($b\ ^1\Pi_u$, $b'^1\Sigma_u^+$, $c\ ^1\Sigma_u^+ \rightarrow X\ ^1\Sigma_g^+$) which emit in the UV, recently reported by Ajello et al. (2007) for use in understanding *Cassini* UVIS observations.

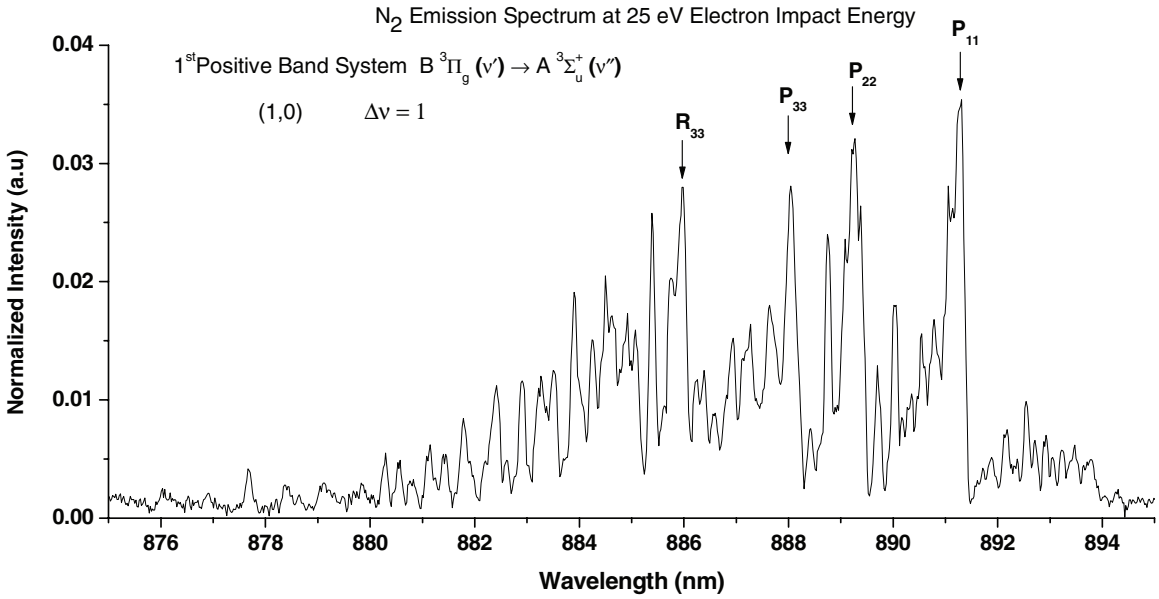

Figure 14. Expanded range of calibrated electron-impact-induced fluorescence spectrum of N_2 covering the (1,0) band of the first positive band system $B\,^3\Pi_g^+(\nu') \rightarrow A\,^3\Sigma_u^+(\nu'')$ showing detailed rotational structures of P, Q, and R branches at 25 eV electron-impact energy at a spectral resolution of 0.07 nm FWHM with a spectrometer resolving power of $\lambda/\Delta\lambda \approx 10000$.

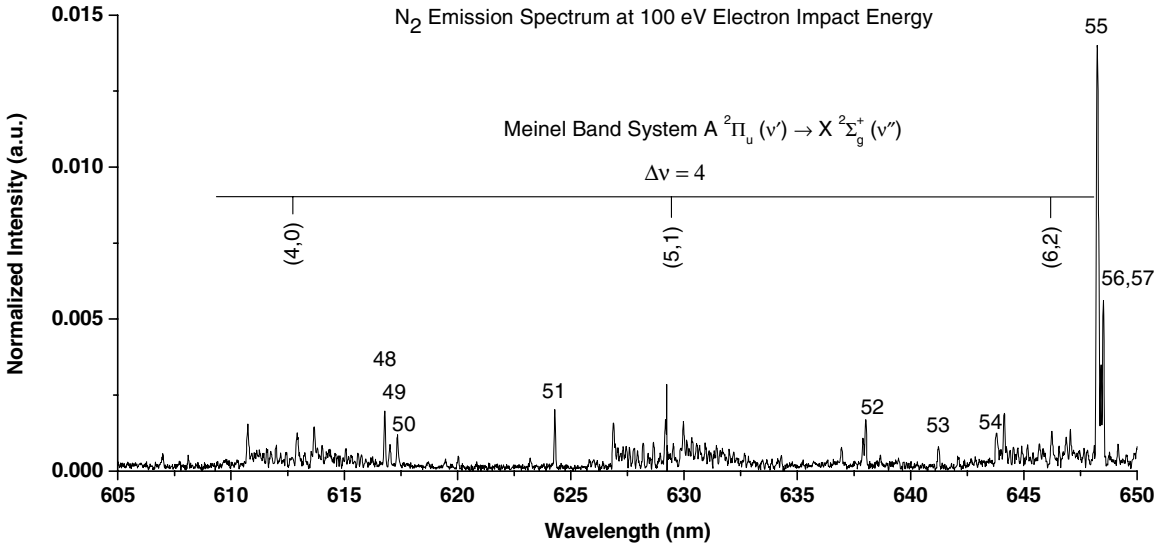

Figure 15. Calibrated electron-impact-induced fluorescence spectrum of N_2 from 605 nm to 650 nm for electron energy of 100 eV, identifying the vibrational bands and sequences of the Meinel band system $A\,^2\Pi_u(\nu') \rightarrow X\,^2\Sigma_g^+(\nu'')$ at a spectral resolution of 0.07 nm FWHM with a spectrometer resolving power of $\lambda/\Delta\lambda \approx 10000$. Strong N I and N II multiplets are also identified as listed in Table 18.

The great enhancement of the 1PB system compared with the 2PB ($C\,^3\Pi_u \rightarrow B\,^3\Pi_g$) system is entirely due to cascading emissions from the $C\,^3\Pi_u$ state to its lower state $B\,^3\Pi_g$ which is the upper state of 1PB ($B\,^3\Pi_g - A\,^3\Sigma_u^+$); hence, the 2PB system is one of the principal cascade contributors to the 1PB emission. Cartwright et al. (1977) have shown that cascading plays a significant role in populating vibrational levels of the A and B states in the aurora. They reported a total of six triplet states, $C\,^3\Pi_u$ (2PB), $C'\,^3\Pi_u$ (Goldstein–Kaplan system), $D\,^3\Sigma_u^+$ (fourth positive system), $E\,^3\Sigma_u^+$, $B'\,^3\Sigma_u^+$, and $W\,^3\Delta_u$ (Wu–Benesch IR system), contributing to the 2PB ($C\,^3\Pi_u \rightarrow B\,^3\Pi_g$) vibrational cross section. All of the direct excitation cross sections of the C state contribute to the B-state cascade cross-sectional along with the other triplet states.

The partial and full manifold of the emission cross sections of the band system at 25 eV and 100 eV are listed in Table 9 and their relative intensities are given in Table 10. We observed 35 bands, which span the ν' levels from 0 through 12, since predissociation occurs in the 1PB system above $\nu' = 12$ (Lofthus & Krupenie 1977). We model the vibrational levels from $\nu' = 0$ to 10 with respect to the measured strongest emission band. The four strongest bands observed are the (1,0) band at 888.3 nm, the (2,1) band at 869.5 nm, the (3,1) band at 760.5 nm, and the (4,2) band at 758. 3 nm. The ν' levels of 11 and 12 are very weakly populated and represent only about 3%–4% of the band system. In Table 11, we present the ν' cross sections for each level. The vibrational population is very evenly distributed among $\nu' = 0$–6 because of many electronic states contributing to the observed band system through cascade. The equilibrium internuclear distance of the B state is 0.12123 nm compared to 0.1148 nm for the C state, 0.1108 nm for the D state, 0.11487 nm for the C state, and 0.11177 nm for the E state,

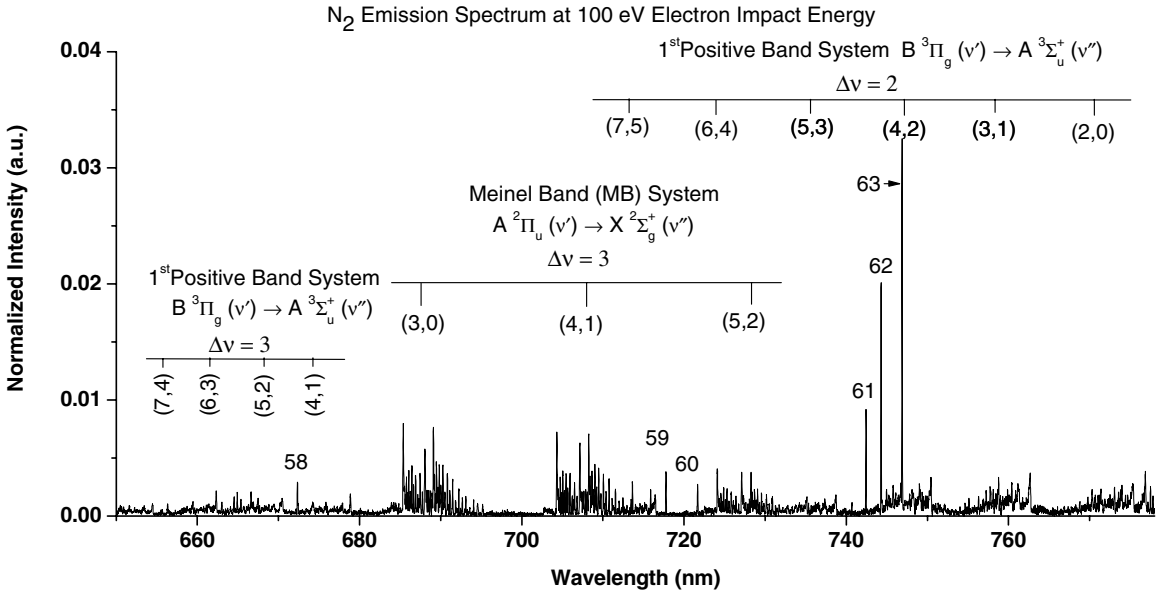

Figure 16. Calibrated electron-impact-induced fluorescence spectrum of N_2 from 650 nm to 780 nm for electron energy of 100 eV, identifying the vibrational bands and sequences of the first positive band system $B\,^3\Pi_g^+(v') \rightarrow A\,^3\Sigma_u^+(v'')$ and Meinel band system $A\,^2\Pi_u(v') \rightarrow X\,^2\Sigma_g^+(v'')$ at a spectral resolution of 0.07 nm FWHM with a spectrometer resolving power of $\lambda/\Delta\lambda \approx 10000$. Strong N I and N II multiplets are also identified as listed in Table 18.

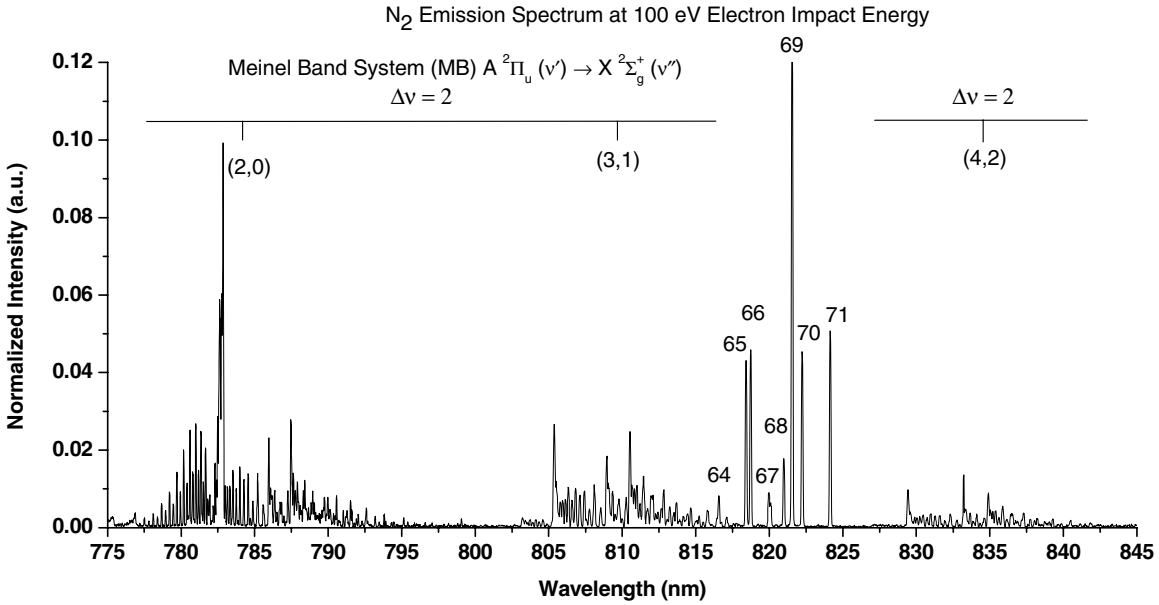

Figure 17. Calibrated electron-impact-induced fluorescence spectrum of N_2 from 775 nm to 845 nm for electron energy of 100 eV identifying the vibrational bands and sequences of the Meinel band system $A\,^2\Pi_u(v') \rightarrow X\,^2\Sigma_g^+(v'')$ at a resolution of 0.07 nm FWHM with a spectrometer resolving power of $\lambda/\Delta\lambda \approx 10000$. Strong N I atomic multiplets are also identified as listed in Table 18.

which are four strong cascading contributions. Tables 11 and 12 compare the band emission cross sections for each vibration level v' and the total emission cross sections in this experiment, respectively, with emission cross sections measured in the past (Stanton & St. John 1969; McConkey & Simpson 1969). The earlier work was done at much lower spectral resolution (e.g., compare Figure 2 of Stanton & St. John 1969 with our data shown in Figures 9(a)–10(b)). The electron-impact-induced fluorescence spectrum of the 1PB system has never been completely resolved until the work presented here. Stanton & St. John (1969) revealed that serious overlapping occurred in several Δv sequences (e.g., $\Delta v = 3$ and 4). Our total emission cross section of 61.82×10^{-18} cm^2 is much larger than previous measurements. We attribute this difference to the lack of high resolving power techniques in separating the closely spaced 1PB, high currents and high gas pressures used in determining their cross-sectional values in the past compared to the present measurement conditions. Previously, it has been reported by Stanton & St. John (1969) and McConkey & Simpson (1969) that the $B \rightarrow A$ transitions showed pressure and electron-beam current dependence when observed at pressures and currents higher than 5×10^{-3} Torr and 500 μA, respectively. At higher pressures, collisional quenching can affect the $B\,^3\Pi_g$ population, as $C\,^3\Pi_u$ state transitions occur immediately (10^{-8} s), before the $C\,^3\Pi_u$ state is affected by relaxation processes, whereas the $B\,^3\Pi_g$ state has a relatively long radiative lifetimes (10^{-5} s; Lofthus & Krupenie 1977). The present cross-sectional measurements were made at N_2 gas pressure of 5×10^{-5} Torr and

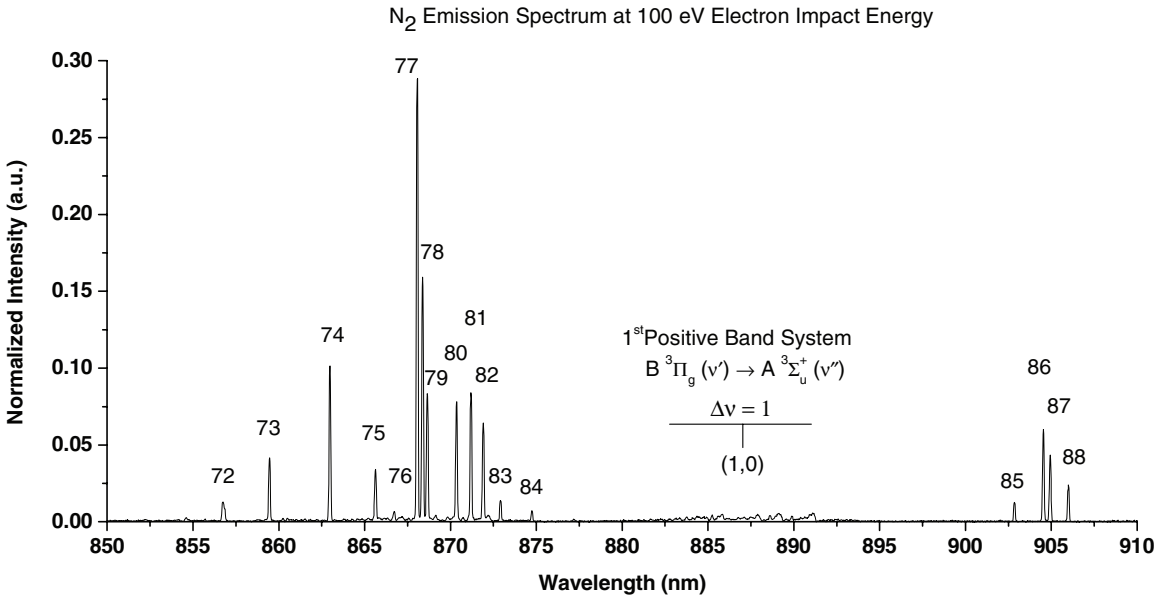

Figure 18. Calibrated electron-impact-induced fluorescence spectrum of N_2 from 850 nm to 910 nm for electron energy of 100 eV identifying the vibrational bands and sequences of the first positive band system $B\ ^3\Pi_g^+(v') \rightarrow A\ ^3\Sigma_u^+(v'')$ at a spectral resolution of 0.07 nm FWHM with a spectrometer resolving power of $\lambda/\Delta\lambda \approx 10000$. Strong N I atomic multiplets are also identified as listed in Table 18.

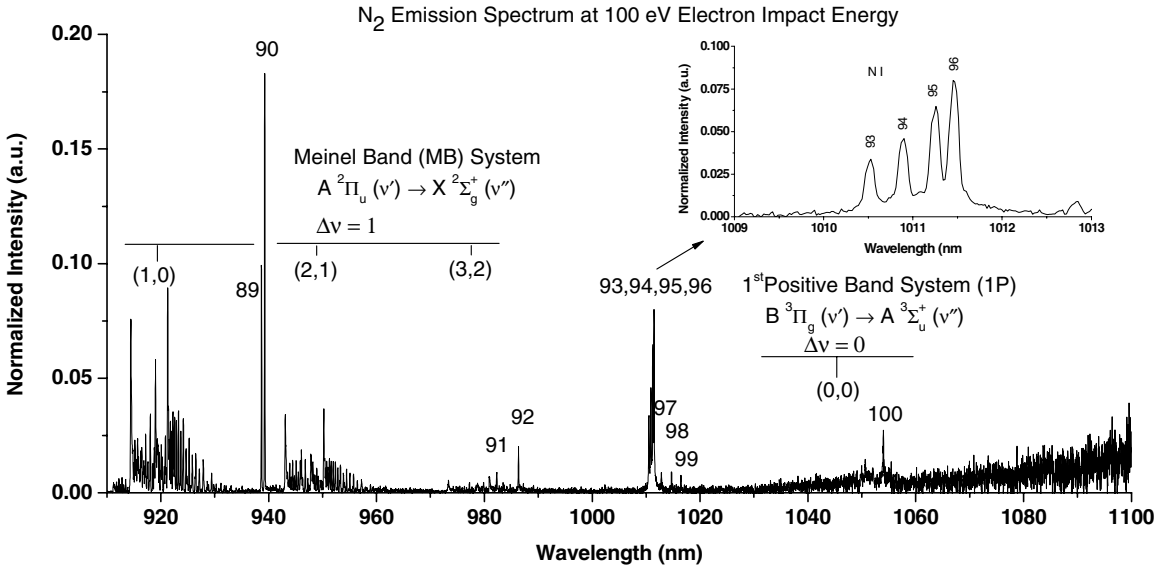

Figure 19. Calibrated electron-impact-induced fluorescence spectrum of N_2 from 910 nm to 1100 nm for electron energy of 100 eV identifying the vibrational bands and sequences of the Meinel band system $A\ ^2\Pi_u(v') \rightarrow X\ ^2\Sigma_g^+(v'')$ and the first positive band system $B\ ^3\Pi_g^+(v') \rightarrow A\ ^3\Sigma_u^+(v'')$ at a spectral resolution of 0.07 nm FWHM with a spectrometer resolving power of $\lambda/\Delta\lambda \approx 10000$. Strong N I atomic multiplets are also identified as listed in Table 18.

electron-beam currents of 25 μA at 25 eV and 100 μA at 100 eV, such that the effect of secondary electrons was minimized, especially at 100 eV. Moreover, as opposed to the strongest band (1,0) observed in the present measurements, both Stanton & St. John (1969) and McConkey & Simpson (1969) found the (3,1) band to be the strongest one. Our observation is consistent with the prior studies reported in the review article by Lofthus & Krupenie (1977). Stanton & St. John (1969) reported excitation functions for several bands $v' = 0$–9 as a function of electron-impact energy, McConkey & Simpson (1969) reported excitation functions for $v' = 3$, 6, and 8, and both reported the contribution of cascades. A comparison of the relative shapes of their excitation functions somewhat differs from one band to the other, and the two sets of data do not agree with each other.

It is also important to understand the 1PB system by comparing the B state direct excitation cross section with the sum of excitation cross sections for the C, C', B', W, D, E from energy-loss work. We show in Table 13 the direct excitation cross section of the B', C', D, E, and W states available in the literature to determine the total contribution of them to the $B \rightarrow A$ transition via cascade. The sum of the energy-loss excitation cross sections of the C, C', B', W, D, E state should be more than 90% of the cascade cross section. Unfortunately, only the B, B', C, and D states excitation cross sections have been measured as described in Table 13 (Cartwright et al. 1977; Campbell et al. 2001; Johnson et al. 2005; Malone et al. 2009). Campbell et al., who measured the complete set of B, B', C, and E cross sections, found a total excitation cross section of 42.4 $\times$ 10^{-18} cm^2 at 25 eV. The sum over v'' of the $D \rightarrow B$ $(0,v'')$ optical-emission

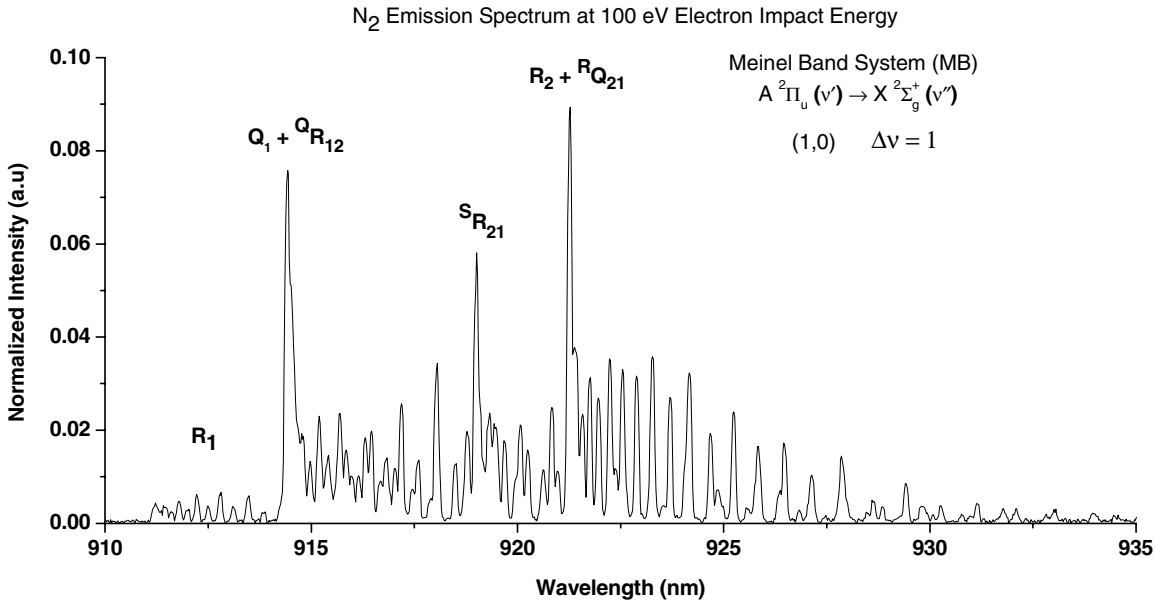

Figure 20. Expanded range of calibrated electron-impact-induced fluorescence spectrum of N_2 covering the (1,0) band of Meinel band system $A\,^2\Pi_u(\nu') \rightarrow X\,^2\Sigma_g^+(\nu'')$ showing detailed rotational structures of several branches for electron energy of 100 eV at a spectral resolution of 0.07 nm FWHM with a spectrometer resolving power of $\lambda/\Delta\lambda \approx 10000$.

cross sections giving the value of 0.127×10^{-18} cm^2 for the cross section for the $v = 0$ vibrational level of the $D(^3\Sigma_u^+)$ state excited by electron collision with the N_2 $X(^1\Sigma_g^+)$ ground state was reported by Filippelli et al. (1984), whereas Skubenich & Zapesochny (1967) reported this to be 1.28×10^{-18} cm^2, an order of magnitude larger. McConkey & Simpson determined this to be 3×10^{-18} cm^2 which is a factor of two larger than Skubenich & Zapesochny (1967). However, they all concluded that the contribution of the D state to $D \rightarrow B \rightarrow A$ cascade is very small (<0.4%) compared to the second positive system via $C \rightarrow B \rightarrow A$. We attribute the differences to incomplete measurement of cascading and root-sum-square experimental errors of the two experiments of about 40%. The 1PB system is the only band system of the four-band systems studied here that shows direct excitation not to be the dominant mechanism. It is, in fact, primarily populated by cascading, indicating that the vibrational distribution is unlikely to be proportional to the X–B Franck–Condon factors for most excited vibrational levels.

3.4. Meinel Band System $A\,^2\Pi_u \rightarrow X\,^2\Sigma_g^+$ of N_2^+

The MB emissions from $A\,^2\Pi_u(\nu') \rightarrow X\,^2\Sigma_g^+(\nu'')$ transitions of N_2^+ were first observed in auroral emissions before being discovered in the laboratory. They have also been detected in comet tails (Jenniskens et al. 2004). The emission cross sections of the MB system are of great importance to studies of Earth's visible aurora and of other nitrogen-bearing atmospheres. Although MB emissions appear beyond 1100 nm (Lofthus & Krupenie 1977), we have observed 12 bands of this doublet system ranging from $\nu' = 1$–5 and $\nu'' = 0$–2 with $\Delta v = 1$–3 sequences within our present VOIR wavelength range. Detailed features of the MB system observed at 25 eV and 100 eV spanning the wavelength range from 560 nm to 1100 nm are shown in Figures 10–12, 15–17, 19, and 20. It is clear from the figures that the $A\,^2\Pi_u(\nu') \rightarrow X\,^2\Sigma_g^+(\nu'')$ system intensities increase with increasing electron-impact energy, as expected, since these transitions occur from electronic states $A\,^2\Pi_u(\nu') \rightarrow X\,^2\Sigma_g^+(\nu'')$ of the ionized N_2^+. The excited state is comprised of two spin-doublet components, $^2\Pi_{1/2}$ and $^2\Pi_{3/2}$ and each component displays a twofold Λ-doublet degeneracy for the P, Q, and R branches, resulting in 12 transitions to the lower state $^2\Sigma_g^+$ (Herzberg 1989). Figure 20 shows a detailed high-resolution spectrum of (1,0) band which appears to have sub-heads of R_1, Q_1 + $^QR_{12}$, $^SR_{21}$, R_2 + $^RQ_{21}$ transitions (Meinel 1950) with each sub-head showing rotational structures degraded toward the red wavelength. The $A \rightarrow X$ transitions are not perturbed by the B state or any higher states since the $\nu' = 0$ level of the B state is above the $\nu' = 9$ level of the A state. Based on the transition probabilities (Lofthus & Krupenie 1977; Laher & Gilmore 1999), the strongest is the (0,0) band of MB system at 1109 nm, slightly outside the present measured range. The second strongest MB system is the (1,0) band at 919 nm (Figure 20).

The $A\,^2\Pi_u(\nu') \rightarrow X\,^2\Sigma_g^+(\nu'')$ emissions are further complicated as they appear in the near-infrared spectral region where they often overlap with the bands of 1PB system of N_2 ($B\,^3\Pi_g - A\,^3\Sigma_u^+$) which is simultaneously excited by electron impact on N_2. As a result, it is difficult to distinguish between their respective emissions. In order to resolve each band system's signature and determine their respective contributions, we have modeled the overlapping MBs (and also weak bands) using the transition probabilities provided in the review by Gilmore et al. (1992). For each ν'-progression, we have chosen the strongest unblended bands that are free of contamination by other bands for normalization of emission cross sections using Equation (11), for example, the (1,0) band at 919 nm for $\nu' = 1$, the (2,1) band at 947 nm for $\nu' = 2$, the (3,1) band at 809 nm for $\nu' = 3$, the (4,1) band at 707 nm for $\nu' = 4$, and the (5,2) band at 727 nm for $\nu' = 5$. We list emission cross sections of the MB system at 25 and 100 eV by (ν',ν'') in Table 14 along with the available data in the literature for comparison, and the relative values of these bands are given in Table 15 for comparing branching ratios. Furthermore, we sum the emission cross sections for each vibrational ν', ν''-progression to obtain the total vibrational cross section $\Sigma_{\nu''} Q_{\rm em}(\nu',\nu'')$ for each vibrational level ν' and then sum all the ν' total cross sections to obtain the total band system electronic cross section $\Sigma_{\nu'}\ Q_{\rm em}(\nu')$. The values so obtained are listed in Tables 16 and 17, respectively.

The agreement for the individual band emission cross sections among the published data listed in Table 14 is relatively poor at both 25 eV and 100 eV. Consequently, the total electronic cross sections at 25 eV and 100 eV, when compared among the three published experiments, also remain in poor agreement. For example, in Table 17, a comparison of total electronic cross sections at 100 eV for three experimenters from Simpson & McConkey (1969), Piper et al. (1986), and the theoretical cross section of Shemansky & Liu (2005) based on photoionization electric dipole oscillator strengths, are scattered over a range from 26.5×10^{-18} cm^2 to 115×10^{-18} cm^2, compared with our measured value at 32.4×10^{-18} cm^2 and our modeled value at 27.34×10^{-18} cm^2. A comparison of our emission cross-sectional values at 25 eV and 100 eV in Table 17 with the ionization cross sections of Shemansky & Liu (2005) at the same pair of energies also show poor agreement. At the same time, at 100 eV we find our data and Simpson & McConkey (1969) differing by 40%.

The distribution of vibrationally excited N_2^+ ($X\ ^2\Sigma_g^+$) ions in the auroral atmosphere depends in part on the excitation cross sections of the $A\ ^2\Sigma_u^+$ state. Although the relative vibrational excitation rates are well established, the published values for the electronic excitation of the MBs differ by an order of magnitude (Piper et al. 1986). We believe the discrepancies arise mainly from the high-pressure effects of quenching in the experimental conditions and from lack of spectral resolution. The variations in the excitation cross sections are attributed not only to collisional effects but also to the effects of electric fields used in the measurements (e.g., Shemansky & Broadfoot 1971). Our laboratory measurements are conducted at the lowest pressure (5×10^{-5} Torr) to date to help circumvent this problem. Recently, Piper et al. (1986) made measurements at an N_2 gas pressure of 7×10^{-4} Torr and presented a review comparing their results for the strongest individual bands for $\nu' = 2$–7 to other laboratory measurements in the wavelength range of 600–850 nm. The spectral resolution is another important factor in resolving various bands in the overlapping wavelength region. Coarse resolution is suspected for the disagreement among the previously published. Moreover, all the early experiments used current meters rather than pulse counting or imaging as available today to measure the intensity of the MB emissions. None of the early experiments, including the recent one by Piper et al. (1986), listed the spectral resolution of their measurements or published the emission spectra of the $A\ ^2\Pi_u(\nu') \rightarrow X\ ^2\Sigma_g^+(\nu'')$ system. The much larger MB cross sections of Piper et al. (1986) could also be due to their normalization procedure, in which they used the cross section of the (0,0) band at 391.4 nm of the 1NB of Borzt & Zipf (1970) which is much higher compared to our value for the same 1NB (0,0) band (Section 3.2).

Another complication affecting the laboratory measurements is that the MBs have relatively longer radiative lifetimes compared to other nitrogen band systems, making it harder to capture their emissions within the field of view of the optical spectrometer. For example, the lifetimes (τ) of the upper state $A\ ^2\Pi_u$ of the MB system of N_2^+ have been measured by various workers (Peterson & Moseley 1973; Popkie & Henneker 1971; Shemansky & Broadfoot 1971; Holland & Maier 1972a, 1972b). The most recent work of Peterson & Moseley (1973), who measured τ using time-of-flight technique for several MBs, found τ in the range of 13.9–7.3 ($\pm$1–0.4) μs, which somewhat agrees with $\tau = 11$ μs found by Holland & Maier (1972a, 1972b) and is in between values of $\tau = 16$–10 μs by Popkie & Henneker (1971) and $\tau = 8.5$–6 μs found by Shemansky & Broadfoot (1971). For natural radiative lifetimes in the 10 μs range, either collisional quenching or diffusion losses are usually present under the conditions in which excited gases are studied in the laboratory. At low pressures, the thermal ions move about 0.5 cm in one radiative lifetime, which is a sizable fraction of the distance from the beam axis to the edge of the observable volume. Our spectrometer field of view is about 4 cm which might not be sufficient to measure the entire $A\ ^2\Pi_u(\nu') \rightarrow X\ ^2\Sigma_g^+(\nu'')$ emission region. We assume in modeling the experiment that the emission per unit length within the collision volume is equal to the excitation per unit length.

The total vibrational emission cross sections at 25 eV and 100 eV of the present study closely follow Franck–Condon factors, with the exception of $\nu' = 2$ and 4. We find $\nu' = 2$ to be the strongest vibrational level and represents about 40% of the band system at both 25 eV and 100 eV, while the $\nu' = 1$ level has a similar excitation function and represents about 33% of the total population.

3.5. N I and N II Emissions of N_2

Nitrogen line emissions can occur due to the excitation of N_2 through both dissociation and dissociative ionization by electron impact. Like N_2 band emissions, atomic line emissions of N I and N II are very important for space weather studies (Bucsela & Sharp 1997). The present VOIR emissions, which can contribute to UV emissions by cascading, are needed for modeling the nitrogen-bearing atmospheres of outer planets and their satellites (Ajello et al. 2007, 2008; Stern et al. 2008). For example, Doppler broadening of the 500.56 ($3p\ ^3D$–$3d\ ^3F^\circ$) multiplet at 200 eV electron-impact energy was reported by Erdman & Zipf (1987) as a way to separate the relative contributions of direct excitation of atomic N and dissociative excitation of N_2 to determine the source of this emission in Earth's upper atmosphere. Therefore, absolute cross sections for these atomic emissions are important to determine if other processes than the direct dissociative ionization and excitation of N_2 by electron impact excite atomic emission lines in the aurora. However, only three sets of cross-sectional measurements for a very few N I and N II emissions have been reported in the past in the VOIR range: for 500.1–500.6 nm, 566.7 nm at 150–4000 eV by Srivastava (1969), for 568.0 nm, 500.3 nm, 568.0 nm at 50–5000 eV by Aarts & De Heer (1971), and 10 line emissions in the range of 453.0–500.5 nm by Lewis et al. (1975). The present studies are timely for future planned observations by instrumentation on the New Horizons mission to the Pluto system (Stern et al. 2008) and by the *Cassini* ISS at Saturn (Porco et al. 2004).

In the past, we have performed extensive studies of dissociative excitation of resonance multiplets of atomic nitrogen N and N^+ ion emissions at UV wavelengths by electron impact on N_2 (Ajello & Shemansky 1985; Ajello et al. 1989, 2007, 2008b). The multiplets studied in the VOIR make significant cascade contributions to the prominent multiplets of UV at 91.9 and 108.5 nm for the N^+ ion emissions and at 95.4 nm, 96.4 nm, 113.4 nm, 120.0 nm, 149.4 nm, and 174.4 nm for N emissions. For example, the lower state of the N I 868 nm emission is also the upper state of the N I 120.0 nm multiplet (Budzien et al. 1994). Figures 6–14 show various N I and N II emissions resulting from electron impact on N_2, and these emissions become prominent with increasing in electron-impact energy. We determined the cross sections of all these lines by normalization with respect to the absolute emission cross section of the (0,0) band of the 1NB system ($B\ ^2\Sigma_u^+ \rightarrow X\ ^2\Sigma_g^+$). Care was taken

in determining the cross sections of some of the line emissions, which appeared over the band emissions of 2PB, 1NB, 1PB, and MB systems, especially at 100 eV. In Table 18, we have listed 100 line emissions observed and their multiplets in the VOIR range of the present measurements at both 25 eV and 100 eV along with the data of Aarts & De Heer (1971) for comparison. The total line emission cross sections $Q_{em}(T)$ at both 25 eV and 100 eV electron-impact energies were obtained by summing all the cross-sectional values of N I and N II emissions. These values are much smaller compared to those values of each band system (2PB, 1NB, 1PB, and MB) emissions at the same energies. For identification of these line emissions, we used the electronic configuration of the radiating states available from the NIST atomic spectra database. Since we carried out measurements at low pressure and low electron-beam currents, we consider that the secondary effects such as quenching and polarization can be neglected. Our cross sections are accurate to within 30% as described in Section 2. The most prominent examples of near-IR atomic emissions are the dipole-allowed transitions 862.9 nm, 868.0 nm, 868.3 nm, 868.6 nm, 870.3 nm, 871.2 nm, 871.92 nm, 939.2 nm, 1011 nm of $2s\ ^2 2p\ ^2(^3P)3s$–$2s\ ^2 2p\ ^2(^3P)3p$. Most of the transitions come from $3s$–$3p$ (i.e., $2s\ ^2 p\ ^2 3s$–$2s\ ^2 2p\ ^2 3p$), and relatively less from $3s$–$4p$, $3s$–$5p$, $3p$–$3d$, $3p$–$4d$, $3p$–$5d$ states as shown in Table 18. Our cross-sectional value of 0.0965×10^{-18} cm^2 for N II 500.3 nm is in excellent agreement with the 0.098×10^{-18} cm^2 determination of Aarts & De Heer (1971). The 500.3 nm is a cascade to 568 nm, and 938.0 nm, 821.3 nm, 868.0 nm, 906.0 nm are the cascade contributions to the 120.0 nm, 149.4 nm, 174.4 nm, 117.7 nm multiplets, respectively.

4. SUMMARY AND CONCLUSIONS

We have performed a laboratory study of electron-excited VOIR (330–1100 nm) emissions of N_2 gas. The excitation mechanisms from the $X\ ^1\Sigma_g^+$ ground state are both dipole-allowed (producing excited singlet states) and spin-forbidden (producing triplet states) excitations. The latter are strong at low electron energies below 30 eV. Thus, the triplet transitions (1PB and 2PB systems) of N_2 are strong at low electron-impact energy while the doublet transitions, the first negative and MB systems of N_2^+, are strong at higher electron-impact energy with a peak emission cross section near 100 eV. In addition, electron-excited dissociation of N_2 produces neutral and ionic atomic emissions prevalent at energies above 25 eV. The spectrum of molecular nitrogen is strongly energy dependent over the electron energy range from 25 to 100 eV. The VOIR spectra are dominated by the band systems emissions of N_2 and N_2^+ compared to the N I and N II emissions. The four most important nitrogen-bearing atmospheres in the solar system belonging to Earth, Titan, Triton, and Pluto are at a high degree of current interest and their nitrogen airglow and auroral emission are actively being studied (or planned for study) by such missions as the TIMED Earth-orbiting satellite, the *Cassini Mission*, and the *Pluto New Horizons Mission*, which carry UV and visible spectral and photometric instrumentation on board.

As an example of how the results presented here may be used, we consider *Cassini* ISS observations of Titan. Images of Titan in eclipse have been obtained and are planned by the *Cassini* spacecraft during the current extended mission, dubbed *Cassini Equinox Mission*, which began in 2008 July. ISS instrument consists of a wide-angle camera and a narrow-angle camera spanning the spectral range of 235–1100 nm (Porco et al. 2004). The narrow-angle camera provides high-resolution images of targets of interest, while the wide-angle camera allows more extended spatial coverage at lower resolution. To increase the images' scientific value, each camera has two filter wheels. The narrow-angle camera has 12 filters in each wheel for a total of 24 filters; the wide-angle has 9 in each wheel for a total of 18. Previous VOIR laboratory work on electron-excited SO_2 has enabled the successful identification of SO_2 as the predominant atmospheric gas on Io from ISS observations (Geissler et al. 2004). Similarly VOIR studies of electron-excited H_2 have identified H_2 as the primary gas in the Saturn auroral zones from ISS observations (Aguilar et al. 2008; Dyudina et al. 2007).

Table 19
Relative Signal Expected from *Cassini* ISS Filters Imaging N_2 Fluorescence (Normalized to Unity in BLUE 1 Filter)

Filter Name	Center Wavelength (nm)	Band Pass (nm)	25 eV	100 eV
Clear	611	235–1100	14.77	3.52
UV1	258	235–280	∼0	∼0
UV2	298	265–330	0.41	∼0.004
UV3	338	300–380	1.31	0.084
BL1	451	390–500	1.	1.
GRN	568	495–635	0.59	0.12
R+G	601	570–635	0.69	0.071
CB1	619	595–615+625–645	0.23	0.025
RED	650	570–635	2.32	0.22
HAL	656	650–660	0.25	0.012
R+IR1	702	670–730	1.04	0.12
IR1	752	670–850	4.43	0.74
IR2	862	800–940	2.4	0.98
IR3	930	880–1025	2.07	0.86
IR4	1002	980–1100	1.23	0.53

Most of Titan's atmospheric nitrogen chemistry is driven primarily from external energy sources such as solar UV and Saturn's magnetosphere (Sittler et al. 2009). The Solar UV tends to dominate the energy input on the day side. Recent observations and analysis of the *Cassini* extreme ultraviolet (EUV: 80–120 nm) and far ultraviolet (FUV: 120–190 nm) disk-wide day and night glows by the *Cassini* UVIS have shown that the deposition of energy to Titan's upper atmosphere is closely coupled to the details of Titan's interaction with Saturn's magnetosphere or magnetosheath or solar wind, since the magnetic field can both insulate the atmosphere against charged particle access to it and/or can channel how this energy penetrates into its upper atmosphere. The most recent analysis of the UVIS observations have shown that the dayside observations that have been analyzed to date are controlled by solar UV (Ajello et al. 2007, 2008; Stevens et al. 2011). We have presented the first UV airglow observations of Titan's atmosphere by the Ultraviolet Imaging Spectrometer on *Cassini*. Using one spectral channel in the EUV from 56.0 nm to 118.0 nm and one in the FUV from 112.0 nm to 191.0 nm, UVIS observed the disk on 2004 December 13 at low solar activity. The EUV spectrum consists of three band systems of N_2 ($b\ ^1\Pi_u$, $b'\ ^1\Sigma_u^+$, $c_4'\ ^1\Sigma_u^+ \rightarrow X\ ^1\Sigma_g^+$), while the FUV spectrum consists of one ($a\ ^1\Pi_g \rightarrow X\ ^1\Sigma_g^+$). Both the EUV and FUV spectra contain many N I and N II multiplets that are produced primarily by photodissociative ionization. However, recent UVIS observations of the night side have shown evidence of strong particle excitation (Ajello et al. 2011).

We show in Table 19 the color ratios expected from the ISS filters, which have been normalized to unity for the BL1 filter, for observations of Titan N_2 emissions excited by 25 eV and

100 eV electrons, the typical energies of secondary electrons in a particle excited atmosphere (Ajello et al. 2005). The table reflects the areas under the VOIR spectra at 25 eV and 100 eV in Figures 3(a) and (b), respectively, within each filter bandpass given in Table 19 of electron-excited N_2. At both electron-impact energies of this laboratory study, the $N_2^+(0,0)$ band at 391.4 nm of the 1NB System $B\,^2\Sigma_u^+(0) \rightarrow X\,^2\Sigma_g^+(0)$ is the strongest emission feature expected. This feature lies within the BL1 filter bandpass of 390–500 nm. The UV3 filter contains the strongest feature within the 2PB system $C\,^3\Pi_u(0) \rightarrow B\,^3\Pi_g(0)$ at 337.1 nm and the two IR1 filters centered at 702 and 752 nm contain the strongest features of the 1PB system $\Delta v = 2$ sequence (such as $B\,^3\Pi_g(3) \rightarrow A\,^3\Sigma_u^+(1)$ at 760.5 nm). The ratio of the single-scattered intensities found in the thermosphere of Titan of these two triplet series electronic transitions, excited from the single ground state, along with the BL1 filter determines the three most interesting filter combinations with which to observe Titan. The change in the ratios of the intensities found within the UV3 to BL1 to IR 1 filters with electron energy is dramatic due to strength of strong vibrational bands of the 2PB system (0,0) band at 337.1 nm or the 1PB system (3,1) band at 760.5 nm at low electron energies, e.g., 25 eV. On the other hand, the 1NB B–X(0,0) band at 391.4 nm found within BL1 and other optically allowed dissociation excitations and ionization excitation transitions are preferentially strong at higher electron energies, e.g., 100 eV electron energy. These optically allowed transitions in BL1 include the N I and N II atomic multiplets and MBs ($A\,^2\Pi_u \rightarrow X\,^2\Sigma_g^+$).

The present cross sections of vibrational bands and high-resolution rotational line emissions aid in determining the ratio of N_2/N_2^+ and electron energy and fluxes in the aurora. High-resolution rotational structure of the 1NBs of N_2^+ can be used to determine neutral temperatures and emission height variations in auroral heights from solar system objects bearing N_2 atmospheres.

The laboratory measurements described in this text were carried out at the Jet Propulsion Laboratory, California Institute of Technology. The work was supported by the NASA Planetary Atmospheres Program Office, NASA *Cassini* Data Analysis Program Office, NASA Space Astrophysics Research Program Office, NASA Outer Planets Research Analysis Program Office, the Geospace Program Office, and the Aeronomy Program of the National Science Foundation. We thank Ronald Cummings for his technical assistance.

REFERENCES

Aarts, J. F. M., & De Heer, F. J. 1969, Chem. Phys. Lett., 4, 116
Aarts, J. F. M., & De Heer, F. J. 1971, Physica, 52, 45
Aarts, J. F. M., De Heer, F. J., & Vroom, D. A. 1968, Physica, 40, 197
Aguilar, J. M., Ajello, R. S., Mangina, G. K., et al. 2008, ApJS, 177, 388
Ajello, J. M., Aguilar, A., Mangina, R. S., et al. 2008a, J. Geophys. Res.-Planets, 113, E03002
Ajello, J. M., Gustin, J., Stewart, I., et al. 2008b, Geophys. Res. Lett., 35, L06102
Ajello, J. M., Hansen, D., Beegle, L. W., et al. 2002, J. Geophys. Res., 107, SIA2.1
Ajello, J. M., James, G. K., Franklin, B. O., & Shemansky, D. E. 1989, Phys. Rev. A, 40, 3524
Ajello, J. M., Pryor, W., Esposito, L., et al. 2005, Icarus, 178, 327
Ajello, J. M., Rao, S. M., & Meier, R. R. 2011, in Recent Advances, Applications, and Interfaces, UV Molecular Spectroscopy from Electron-impact for Applications to Planetary Atmospheres and Astrophysics in Charged Particle and PhotoInteractions with Matter, ed. Y. Hatano, Y. Katsumura, & A. Mozumder (Boca Raton, FL: Taylor & Francis), 761
Ajello, J. M., & Shemansky, D. E. 1985, J. Geophys. Res., 90, 9845
Ajello, J. M., Stevens, M. H., Stewart, I., et al. 2007, Geophys. Res. Lett., 34, L24204
Ajello, J. M., et al. 1988, Appl. Opt., 27, 890
Avakyan, S. V., Ii'In, R. N., Lavrov, V. M., & Ogurstov, G. N. 1998, Collision Processes and Excitation of UV Emission from Planetary Atmospheric Gases: A Handbook of Cross Sections (Amsterdam: Gordon and Breach)
Biloiu, C., Sun, X., Harvey, Z., & Scime, E. 2007, J. App. Phys., 101, 073303
Borst, W. L., & Zipf, E. C. 1970, Phys. Rev. A, 1, 834
Bucsela, E., Morrill, J., Heavner, M., et al. 2003, J. Atmos. Sol.–Terr. Phys., 65, 583
Bucsela, E. J., & Sharp, W. E. 1997, J. Geophys. Res., 102, 2457
Budzien, S. A., Feldman, P. D., & Conway, R. R. 1994, J. Geophys. Res., 99, 23275
Burns, D. J., Simpson, F. R., & McConkey, J. W. 1969, J. Phys. B: At. Mol. Phys., 2, 52
Campbell, L., Brunger, M. J., Nolan, A. M., et al. 2001, J. Phys. B: At. Mol. Opt. Phys., 34, 1185
Cartwright, D. C., Trajmar, S., Chutjian, A., & Williams, W. 1977, Phys. Rev. A, 16, 1041
Chakrabarti, S. 2001, J. Atmos. Solar-Terr. Phys., 60, 1403
Culp, G., & Stair, A. T., Jr. 1967, J. de Chimie Physique et de Physsicochimie Bilogique, 64, 57
De Heer, F. J., & Aarts, J. F. M. 1970, Physica, 48, 620
Doering, J. P., & Yang, J. 1996, J. Geophys. Res., 101, 19,723
Dyudina, U. A., Ingersoll, A. P., & Ewald, S. P. 2007, in AGU Fall Meeting Suppl., 52, P31A
Erdman, P. W., & Zipf, E. C. 1987, Planet. Space Sci., 35, 1471
Espy, P. J., Pendleton, W. R., Jr., Sivjee, G. G., & Fetrow, M. P. 1987, J. Geophys. Res., 92, 11,257
Filippelli, A. R., Chung, S., & Lin, C. C. 1984, Phys. Rev. A, 29, 1709
Finn, T. G., Aarts, J. G. M., & Doering, J. P. 1972, Chem. Phys., 56, 5632
Fons, J. T., Schappe, R. S., & Lin, C. C. 1996, Phys. Rev., 53, 2239
Galand, M., & Chakrabarti, S. 2006, J. Atmos. Sol.–Terr. Phys., 68, 1488
Geissler, P., McEwen, A., Porco, C., et al. 2004, Icarus, 172, 127
Gilmore, F. R., Laher, R. R., & Espy, P. J. 1992, J. Phys. Chem. Ref. Data, 21, 1005
Heavner, M. J., Morrill, J. S., Siefring, C., et al. 2010, J. Geophys. Res., 115, A00E44
Herzberg, G. 1989, Molecular Spectra and Molecular Structure. I. Spectra of Diatomic Molecules (Malabar, FL: Krieger)
Holland, R. F., & Maier, W. B., II 1972a, J. Chem. Phys., 56, 5229
Holland, R. F., & Maier, W. B., II 1972b, J. Chem. Phys., 58, 2672
Hollstein, M., Lorents, D. C., Peterson, J. R., & Sheridan, J. R. 1969, Can. J. Chem., 47, 1858
Hoppe, J. C. 1970, J. Quant. Spectrosc. Radiat. Transfer, 10, 823
Huang, X.-J., Xin, Y., Yang, L., Yuan, Q., & Ning, Z. Y. 2008, Phys. Plasmas, 15, 113504
Itikawa, Y. 2006, J. Chem. Phys. Ref. Data, 35, 31
Itikawa, Y., Hayashi, M., Ichimura, A., et al. 1986, J. Chem. Phys. Ref. Data, 15, 985
Jenniskens, P., Christophe, O. L., & Schaller, E. L. 2004, Astrobiology, 4, 109
Jobe, D., Sharpton, F. A., & St. John, R. M. 1967, J. Opt. Soc. Am., 57, 106
Johnson, P. V., Malone, C. P., Kanik, I., Tran, K., & Khakoo, M. A. 2005, J. Geophys. Res., 110, A11311
Jokiaho, O., Lanchester, B. S., Ivchenko, N., et al. 2008, Ann. Geophys., 26, 853
Kanmae, T., Stenbaek-Nielsen, H. C., & McHarg, M. G. 2007, Geophy. Res. Lett., 34, L07810
Karolis, C., & Harting, E. 1978, J. Phys. B: At. Mol. Phys., 11, 357
Khakoo, M., Johnson, P. V., Ozkay, I., et al. 2005, Phys. Rev. A, 71, 062703
Koehler, R. A., Shepherd, M. M., Shepherd, G. G., & Paulson, K. V. 1981, Can. J. Phys., 59, 1143
Koval, A. G., Koppe, V. T., Proshchak, L. I., & Fogel, Ya. M. 1969, Opt. Spectrosc., 27, 198
Kryuchkov, S. I., Kudryavstev, N. N., & Novikov, S. S. 1984, Z. Prikladnoi Spektroskopii, 40, 618
Laher, R. R., & Gilmore, F. R. 1999, http://spider.ipac.caltech.edu/~laher/fluordir/fluorindex.html
Lavrov, B. P., & Pipa, A. V. 2002, Opt. Spectrosc., 92, 709
Lewis, J. W. L., Price, L. L., & Powell, H. M. 1975, Phys. Rev. A, 11, 1214
Linss, V. 2005, Spectrochim. Acta B, 60, 253
Lofthus, A., & Krupenie, P. H. 1977, J. Phys. Chem. Ref. Data, 6, 113
Majeed, T., & Strickland, D. 1997, J. Chem. Phys. Chem. Ref. Data, 26, 335
Malone, C. P., Johnson, P. V., Kanik, I., et al. 2009, Phys. Rev. A, 79, 032705
Mandelbaum, D., & Feldman, P. D. 1976, J. Chem. Phys., 65, 672
Maseberg, J. W., & Gay, T. J. 2010, J. Phys: Conf. Ser., 212, 012021
McConkey, J. W., & Latimer, I. D. 1965, Proc. Phys. Soc., 86, 463

McConkey, J. W., & Simpson, F. R. 1969, J. Phys. B, 2, 923
McConkey, J. W., Woolsey, J. M., & Burns, D. J. 1971, Planet. Space Sci., 19, 1192
Meier, R. R. 1991, Space Sci. Rev., 58, 1
Meinel, A. B. 1950, ApJ, 112, 562
Nassar, H., Pellerin, S., Musiol, K., et al. 2004, J. Phys. D: Appl. Phys., 37, 1904
Nishimura, H. 1968, J. Phys. Soc. Japan, 24, 130
Parigger, C., Plemmons, D. H., Hornkohl, J. O., & Lewis, J. W. L. 1995, Appl. Opt., 34, 3331
Peterson, J. R., & Moseley, J. T. 1973, J. Chem. Phys., 58, 172
Piper, L. G., Green, B. D., Blumbergt, W. A. M., & Wolnik, S. J. 1986, J. Phys. B: At. Mol. Phys., 19, 3327
Poparic, G. B. 2008, Phys. Chem. Technol., 6, 41
Popkie, H. E., & Henneker, W. H. 1971, J. Chem. Phys., 55, 617
Porco, C. C., West, R. R., Squyres, S., et al. 2004, Space Sci. Rev., 115, 363
Romick, G. J., Yee, J. H., Morgan, M. F., et al. 1999, Geophys. Res. Lett., 26, 1003
Romick, K. J., Smith, R. W., & Lummerzheim, D. 2001, J. Atmos. Sol.–Terr. Phys., 63, 295
Sakamoto, T., Matsuura, H., & Akatsuka, H. 2006, Japan J. App. Phys., 45, 7905
Shaw, M., & Campos, J. 1983, J. Quant. Spectrosc. Radiat. Transfer, 30, 73
Shemansky, D. E., Ajello, J. M., & Kanik, I. 1995, ApJ, 451, 472
Shemansky, D. E., & Broadfoot, A. L. 1971, J. Quant. Spectrosc. Radiat. Transfer, 11, 1385
Shemansky, D. E., & Liu, X. 2005, J. Geophys. Res., 110, A07307
Simpson, F. R., & McConkey, J. W. 1969, Planet. Space Sci., 17, 1941
Sittler, E., Hartle, R. E., Bertucci, C., et al. 2009, in Titan, from Cassini-Huygens chap. 16, 393
Skubenich, V. V., & Zapesochny, I. P. 1967, in Proc. 5th Int. Conf. on the Physics of Electronic and Atomic Collisions (Leningrad: Nauka), 570
Skubenich, V. V., & Zapesochny, I. P. 1981, Geomag. Aeronomy, 21, 355
Solomon, S. C. 1989, J. Geophys. Res., 94, 17215
Srivastava, B. N. 1969, J. Quant. Spectrosc. Radiat. Transfer, 9, 1639
Srivastava, B. N., & Mirza, I. M. 1968a, Phys. Rev., 176, 137
Srivastava, B. N., & Mirza, I. M. 1968b, Phys. Rev., 168, 86
Srivastava, B. N., & Mirza, I. M. 1968c, Can. J. Phys., 47, 475
Stanton, P. N., & St. John, R. M. 1969, J. Opt. Soc. Am., 59, 252
Stern, S. A., Slater, D. C., Scherrer, J., et al. 2008, Space Sci. Rev., 140, 155
Stevens, M., Gustin, J., Ajello, J., et al. 2011, J. Geophys. Res., 116, A5
Strickland, D. J., Bishop, J., Evans, J. S., et al. 1999, J. Quant. Spectrosc. Radiat. Transfer, 62, 689
Strickland, D. J., Evans, J. S., & Paxton, L. J. 1995, J. Geophys. Res., 100, 12217
Tohyama, Y., & Nagata, T. 2005, J. Phys. Soc. Japan, 74, 326
Yelle, R. V., Borggren, N., de la Haye, V., et al. 2006, Icarus, 182, 567
Zubek, M. 1994, J. Phys. B: At. Mol. Opt. Phys., 27, 573